RADIOCHROMIC FILM DOSIMETRY SYSTEM

FOR CLINICAL CTDI MEASUREMENTS

Chrystian Quintero Mateus

Medical Physics Unit

McGill University, Montreal

December 2014

A thesis submitted to McGill University in partial fulfillment of the requirements for the degree of

MASTER OF SCIENCE

In Medical Radiation Physics

Table of Content

Acknowledgements

I want to express my deepest appreciation to my supervisor Professor Nada Tomic. I would like to thank her for constant focus, guidance and comments on my research, as well as facilitating my studies in the Radiation Oncology Department of the Jewish General Hospital. I would also like to thank Professor Slobodan Devic for serving as my co-supervisor. To them, special thanks for their excellent comments and suggestions during all the stages of this thesis. Not only did they support and fund my research project, but also their personal advice was priceless.

I would like to thank all members of the McGill Medical Physics Unit, as well as those friends who helped me with their company and encouragement.

Words cannot express how grateful I am to my family. I want to dedicate this thesis to my parents, sisters and brother. I hope they feel as proud of my accomplishments, as I am of having them supporting me.

Chrystian Quintero M.

Abstract

The scope of this project was to measure dose profiles using Gafchromic® XR-QA2 films when clinical protocols were used to scan a PMMA phantom with CT scanners and kV Cone Beam Computed Tomography (CBCT) systems integrated into linear accelerators. Estimated volume CT dose index $CTDI_{\mathrm{vol}}$ values based on measured dose profiles were compared to tabulated data in order to assess the reproducibility and accuracy of this method in clinical use. The feasibility study of the radiochromic film-based dosimetry system included an evaluation of the film response as a function of the effective photon energy over the energy range used in radiology and estimation of the precision of the CTDI measurements during helical (on CT scanner) and cone beam CT acquisitions (on linear accelerator).

Energy dependence of the Gafchromic® XR-QA2 film was tested over the imaging energy range covered by multiple commercially available CT scanners and on-board imaging (*OBI*) devices on linear accelerators. A General Electric LightSpeed® LS 16 radiotherapy simulator was used for this purpose. The effective energy of multiple beams was estimated via HVL measurements, and the device output was obtained following the AAPM TG-61 protocol. Strips of film were irradiated in air to known air kerma values ($[K_{air}]_{air}$) with the x-ray tube of the CT scanner in static mode. The reflectance change of the film prior and after irradiation was assessed using an in-house Matlab code with the *TIFF* images of the films scanned by an Epson® Expression 10000XL flatbed document scanner. Calibration curves for each beam quality were created to model the response of the film in the $[K_{air}]_{air}$ range up to100 mGy. Pixel values were read out after applying a low filter kernel to the extracted red channel from the images. Responses of the film for the same dose values were then compared.

Film strips were sandwiched between PMMA rods cut in half and placed into both the peripheral and central holes of a *CTDI* phantom. Three sets of films were irradiated under the same scanning parameters, and the procedure was repeated for several clinical scanning protocols on each imaging device. The change in the reflectance of the film was converted into $[K_{air}]_{air}$ using calibration curves and subsequently converted into dose to water (D_w) using mass energy

absorption coefficients. Finally, D_w profiles were averaged to calculate $CTDI_{\text{vol}}$ values. Averaged $CTDI_{\text{vol}}$ values from three measurements $\left(CTDI_{vol}|_{XR-QA2}\right)$ were compared to the corresponding tabulated $CTDI_{\text{vol}}$ values provided by the manufacturer $(CTDI_{vol}|_{tabulated})$. Dispersion of the data was used to assess reproducibility of the dosimetric system. Measured to tabulated CTDI values ratio was used to assess accuracy.

The relative variation of the film response was determined to be inversely proportional to the absorbed dose The maximum absolute variation of the film response was observed at 30 mGy over the studied effective energy range. The observed variation diminishes up to $50\ \%$ as dose decreases to $5\ \text{mGy}$, and up to $75\ \%$ as dose increases to $100\ \text{mGy}$. The reproducibility of $CTDI_{vol}|_{XR-QA2}$ values was similar for CT simulators and CBCT devices. A linear correlation between $CTDI_{vol}|_{XR-QA2}$ and $CTDI_{vol}|_{tabulated}$ values was found for CT simulators and CBCT devices with acceptable correlation factors. $CTDI_{vol}|_{XR-QA2}$ values were on constantly lower than $CTDI_{vol}|_{tabulated}$ values for CT simulators and higher for CBCT devices.

Film dosimetry using Gafchromic® XR-QA2 film proved to be reproducible regardless of the protocol or device used to irradiate the set of films, but its clinical use may result in relatively high systematic error in dose measurements if a single calibration curve is used. We also found relatively large discrepancy between measured and tabulated $CTDI_{\text{vol}}$ values for various protocols and imaging systems used within radiotherapy department. Our findings strongly support the trend towards replacing the CTDI value with measurement of equilibrium dose in the center of a cylindrical phantom as suggested by TG-111.

Abrégé

Le sujet de cette thèse était de mesurer les profils de dosage des films Gafchromic® XR-QA2® lorsqu'un fantôme PMMA était scanné avec des tomodensitogrammes (scanners CT) et des systèmes CBCT (*Cone Beam Computed Tomography*) reliés à des accélérateurs linéaires, et ce suivant les protocoles cliniques. Les valeurs estimées de tomodensitométrie d'index de dosage CTDIvol, lesquelles sont basées sur les profils de dosage mesurés, ont été comparées aux données indexées de façon à déterminer la reproductibilité et l'exactitude d'une telle méthode à des fins d'usage clinique. L'étude de la faisabilité du système de dosimétrie radiochromic à base de films inclus une évaluation de la réponse du film comme fonction de l'énergie effective du photon par rapport à la portée de l'énergie utilisée en radiologie, de même que l'estimation de la précision des mesures CTDI lors de l'hélicoïdale (sur le CT scan) et lors de l'acquisition CT de rayon coniques (sur l'accélérateur linéaire).

La dépendance énergétique du film Gafchromic® XR-QA2 a été testée sur la portée énergétique d'imagerie couverte par de multiples scanners CT commerciaux de même que par des appareils intégrés d'imagerie sur des accélérateurs linéaires; un simulateur de radiothérapie General Electric LightSpeed LS 16 a été utilisé à cette fin. L'énergie effective de nombreux rayons a été mesurée à travers des mesures *HVL* et l'output du dispositif a été obtenu en suivant le protocole AAPM TG-61. Des parties de films ont été irradiées à l'air afin de déterminer les valeurs de $[K_{air}]_{air}$, et ce à l'aide du tube à rayon x du scanner CT en mode statique. Le changement de réflectivité des films avant et après l'irradiation a été établi en utilisant un code MatLab interne et scannant les images TIFF des films à l'aide d'un scanner de documents à plat Epson Expression 10000XL. Les courbes de calibration pour la qualité de chaque rayon ont été créées afin de répliquer la réponse du film dans un rayon d'air-kerma allant jusqu'à 100 mGy. Les valeurs de pixel ont été lues après l'application d'un filtre bas afin d'extraire le canal rouge des images. Les réponses du film pour des valeurs identiques de dosage ont ensuite été comparées.

Des films fixes ont été placés entre des tiges PMMA coupées en deux et placées dans les torus périphériques et centraux d'un fantôme CTDI en même temps. Trois ensembles de films ont été irradiés avec les mêmes paramètres de scanning, et la procédure a été répétée pour plusieurs

protocoles cliniques de scanning sur chaque appareil d'imagerie (tête axiale, tête multiaxiale, thorax hélicoïdal, pelvis hélicoïdal). Le changement de réflectivité du film a ensuite été converti en $[K_{air}]_{air}$ en utilisant les courbes de calibration et subséquemment converti en dosage dans l'eau en utilisant des coefficients d'absorption de l'énergie de la matière. Finalement, les moyennes des profils de dosage dans l'eau ont été établies en utilisant une longueur d'intégration de 100mm, et ont ensuite servi à calculer le CTDIvol. Les valeurs moyennes de CTDIvol des trois mesures (pour un protocole donné) ont été comparées aux valeurs indexées de CTDI fournies par le fabricant; la dispersion des données a été utilisée afin de déterminer la reproductibilité du système dosimétrique. Les mesures de ratio des CTDI indexés ont été utilisées afin de déterminer l'exactitude des données.

La variation relative du film est inversement proportionnelle à la dose absorbée. La variation absolue maximum de la réponse du film a été observée à 30 mGy pour la portée d'énergie effective donnée. Une telle variation va diminuer jusqu'à 50 % lorsque le dosage est réduit à 5 mGy, et va augmenter jusqu'à 75 % lorsque le dosage est augmenté à 100 mGy. Les valeurs mesurées moyennes de CTDI ont présenté, pour les mêmes machines et protocoles utilisés, une variation moyenne similaire pour les simulateurs CT et pour les appareils CBCT. Une corrélation linéaire a été trouvée pour les simulateurs CT et les appareils CBCT, et ce avec des facteurs de corrélation acceptables. En générale, les valeurs mesurées de $CTDI_{vol}$ étaient plus basses que les valeurs indexées pour les simulateurs CT, et plus élevées pour les appareils CBCT.

La dosimétrie de film basée sur XR-QA2 a prouvée être reproductible peu importe le protocole ou l'appareil utilisé pour irradier un ensemble de films. Toutefois, sont utilisation clinique peu avoir comme résultat une haute erreur systématique dans la mesure de dosage si seulement une courbe de calibration est utilisée. Une importante divergence a été observée entre les résultats des $CTDI_{vol}$ mesurés et indexés pour les différents protocoles et systèmes d'imagerie utilisés dans le département de radiothérapie. Ces résultats viennent fortement supporter la tendance de replacer les valeurs de CTDI par des mesures de dosage équilibrées dans le centre d'un fantôme cylindrique, tel que suggéré par TG-111.

1. Introduction

1.1 On the Computed Tomography (CT) concept

Computed Tomography (CT) scanners were developed to solve common problems associated with early planar radiographic systems. Some of the principal drawbacks of 2D radiography (film/screen) include inefficient x-ray absorption and the consequent waste of information, high scatter-to-primary x-ray ratios that reduce subject contrast (Signal to Noise ratio, SNR), superimposition and conspicuity of organs due to the rendering of 3D objects onto planar images, and the receptor contrast versus latitude trade-off for films [1]. These limitations compromised the performance of the imaging system at acceptable patient dose ranges, as the visualization of low-contrast structures degenerated.

New digital technologies replaced the use of film in radiography, but low-contrast, and conspicuity-related artifacts are intrinsically linked to the use of 2-dimensional imaging technology. On the other hand, cross-sectional imaging systems used for tomography reduce organ image overlaps by sectioning the imaged object into slices to be individually visualized. In general, the intersecting of structures decreases with the thickness of the scanned slice. The blurring due to scattered radiation depends on the way these cross-sections are irradiated, the enhancements in attenuated radiation detection, and reconstruction algorithms [2].

The origin of modern CT technology stems from the basic principles of conventional tomography described by Bocage in 1921 [3]. Bocage provided the first attempt to acquire slice images (1 cm thickness) of an object using the mobile x-ray source-detector assembly. Further enhancements to Bocage's prototype and the development of the theory of image reconstruction from projections allowed the development of the first clinical CT scanner (*Mark I*) in 1971 by Godfrey Hounsfield in England [4].

The theory of the projections image reconstruction postulates that the x-ray transmission through an axial cross section of the imaged body has to be recorded at multiple points (rays) and from diverse angles (views) in order to create an accurate attenuation coefficient map of the object.

The slice consists of 3-dimensional voxels containing tissue descriptors, *i.e.* effective attenuation-coefficient. Measured data in form of a sinogram is used to obtain the elements of the reconstruction matrix through either a filtered back projection or a Fourier-based reconstruction algorithm. The elements of the reconstruction matrix describe how much attenuation of the narrow x-ray beam occurs in each subject voxel [1], and their normalized values are presented as a grey-scale planar image of the object's cross section.

Mark I was the first clinical scanner designed by Hounsfield, and it is an example of the first generation scanners, also referred to as the translate-rotate type scanner. An assembly of an x-ray tube and a single x-ray element NaI scintillation detector is translated in a straight line while a narrow x-ray beam (3 mm thick × 13 mm wide) is used to acquire consecutively 160 individual rays along the 3 mm thick axial cross-section of the imaged subject. Once the attenuation of the rays is measured, the x-ray source-single detector couple rotates at 1° increments around the object to acquire additional views, for a total of 180 different views [5]. Most modern forth generation scanners consist of a rotating fan-beam x-ray source and stationary ring-detectors. They collect normally 360 views, 750 rays each, to create 512×512 reconstruction matrices. Most clinically used CT-scanners are of the third generation, whose key feature is the simultaneous rotation of a CT detector array and the X-ray tube. The success of the 3rd generation CT-scanners was mainly due to development of the slip-ring technology that allows fast signal readout from rotating detectors.

1.2 Clinical use of CT scanners

The presence of CT scanners in clinical facilities has grown since its debut in 1971 along with technical developments and enhancements in the performance of CT technology. Furthermore, large improvements have been made in the optimization of CT image qualities and minimizing dose to the patient. The imaging system sensitivity, dose efficiency, spatial resolution and acquisition times, among other characteristics, have made CT scanners an essential tool in radiology and radiotherapy departments.

The introduction of helical technology in 1990 and multi-slice CT technology in 1999 played a determinant role in the development of new clinical applications for CT scanners [6], such as multiphase exams, vascular and cardiac exams, perfusion imaging and "whole body" screening exams. Due to the widespread use of CT scanners in medical diagnosis and treatment procedures within the last three decades, progressive increase has been observed in the number of CT examinations. The number of procedures increases by about 10% per year, resulting in up to 62 million CT examinations in USA in 2006 [7]. This translates into 32.2 CT scans per million population in USA (2004) and 12.3 CT examinations per million population in Canada (2006) [8].

1.3 Quality Assurance for CT scanners

As for any complex technology, there is a need to define quality criteria that objectively assess the performance of a CT device. The complexity of CT technology and its imaging settings may compromise the image quality or dose to the patient parameters if verification tests are not carried out regularly. Thus, quality criteria have been widely proposed in order to optimize the use of ionizing radiation in radiology and radio-oncology services.

The American Association of Physicists in Medicine (AAPM Report No. 4) defined in 1978 a quality assurance protocol for diagnostic x-ray technology, including a short section on quality assurance tests for "Geometric Tomographic Systems" [9]. An update titled "Quality Control in Diagnostic Radiology" was released in 2002 under the authorship of the Diagnostic X-Ray Imaging Committee (AAPM Report No. 74). This report dedicated a whole section to "Quality Control of Computed Tomography Systems" [10]. Additionally, the AAPM released in 2003 a separate report on quality assurance protocols for CT simulators and the CT simulation process in radiotherapy (AAPM Report No. 66) [11]. The report of the AAPM Group Task No. 75 published in 2007 detailed recommendations for the management of imaging doses during image-guided radiotherapy [12].

The European Commission's Radiation Protections Actions report described an operational framework for radiation protection during CT examinations in the EU in 1999 based on principles previously recommended by the International Committee in Radiation Protection (***ICRP***). This regulation suggests the definition and evaluation of quality criteria for diagnostic images, imaging devices and imaging patient dose. It also provides specific requirements on anatomical imaging criteria and dose to the patient criteria [13].

A considerable group of independent professional associations in medical physics outside of Europe and North America have adopted recommendations on quality control for diagnosis radiology issued by the World Health Organization in 1982 [14] as a guideline to carry out quality tests to x-ray equipment, including CT devices. The International Atomic Energy Agency (IAEA) published an updated report in 2012 that includes principles of image quality assessment, film reject analysis, and patient dose evaluation as part of a general quality control program that will ensure the proper functioning of modern imaging devices [15].

A quality control program, in general, aims to detect any change in the imaging system that may have negative clinical consequences. This may be related to either the quality of the images or a significant increase in patient's exposure to radiation. The dose to the patient is significant, even under normal technical conditions. At the end of the past century, 40% of collective dose to population in Europe was due to exposure to diagnostic radiology (1999) [8], and the corresponding contribution for the USA population reached 24% in 2006 [7]. Deterministic and scholastic injuries-related risks associated with diagnostic doses have been since then widely studied [16-18].

1.4 CT dosimetry

The sensitivity, or ability of CT scanners to visualize low-contrast tissues, is closely related to the dose efficiency, and both relate to the fraction of radiation that can be detected after being transmitted through the patient. Thus, for a given dose, the dose efficiency depends on two detection features: the fraction of transmitted x-rays reaching the sensitive area of the scanner detectors (geometric efficiency), and the fraction of x-rays that are actually interacting (being detected) with the system (absorption efficiency) [1]. There is an implicit limitation on the dose efficiency of CT scanners induced by the inherent presence of quantum mottle (noise) during the measurement process due to the limited number of rays and views acquired by the machine.

Therefore, a compromise between image quality and patient dose has to be achieved during image acquisitions on CT scanners, CT simulators and kV CBCT devices. Studies have shown that, in order to obtain acceptable image quality, CT examinations result in organ dose in the range of $10 - 100$ mGy [7], while planar radiography doses range between $1 - 20$ mGy [8]. The objective of CT dosimetry is to establish diagnostic reference levels under the definition of dosimetric quantities for comparative risk evaluations, and assessment of the performance of CT scanners as a part of the quality assurance protocol [19].

Before the appearance of CT scanners, dosimetry in radiology was limited to the measurement of radiation exposure/dose to the entry surface (Entrance Skin Exposure/Dose, ESE/ESD), as maximal dose is given to the skin of the patient facing the radiation source during planar imaging. In contrast, in CT imaging the radiation source moves constantly around the patient, making it difficult to locate the point on or in the patient where the maximum dose is delivered [20]. Therefore, the concept of ESE is clinically meaningless when applied to CT dosimetry.

Shortly after Hounsfield introduced the first version of a clinical CT scanner in 1971, the International Commission on Radiation Units and Measurements published recommendations on CT dosimetry [21]. In 1977, the AAPM published its own recommendations that defined the methods of CT quality assurance through the utilization of particular phantoms and radiation detectors [22]. The proposed dosimetric practice was to measure exposure with a thermoluminescence dosimeter (LiF TLD) at the center and the surface of a cylindrical anthropomorphic Plexigas phantom (203 mm diameter mimicking head, and 330 mm for body). ***Figure 1.1*** illustrates the technical specifications of dosimetry inserts used to hold the TLD capsules in the phantom, as proposed by the AAPM Report No. 1 [22].

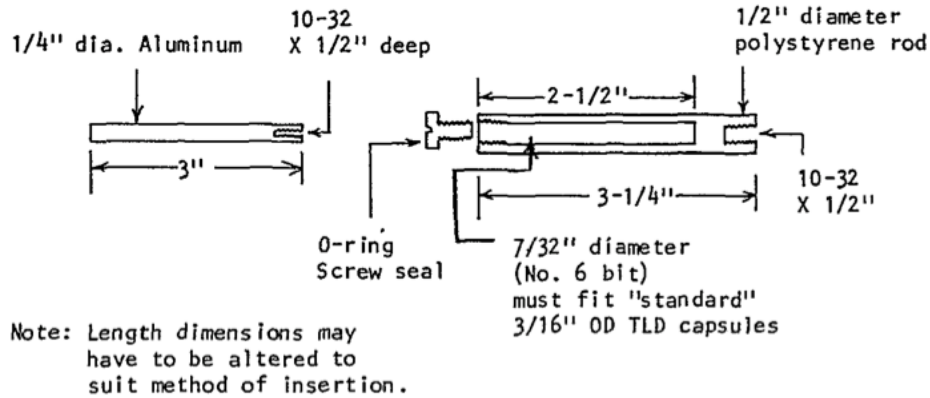

Figure 1.1. Watertight inserts for TLD capsules used in early dose measurements for CT scanners. Image taken from AAPM Report No. 1 [22].

The AAPM report on CT dosimetry (TG-23) published in 2008 provides a review and reinterpretation of fundamental definitions of CT dose parameters. It also includes recommendations on CT dose measurements and interpretation of CT dose risk parameters [6]. The first quantity for dose assessment in CT to be defined was the Computed Tomography Dose Index (*CTDI*)[1]:

$$CTDI = \frac{1}{N \cdot T} \int_{-\infty}^{\infty} D(z)\, dz. \qquad [1.1]$$

The product $N \cdot T$ corresponds to the length covered by the number of channels *N* used to produce tomographic sections of thickness *T* for a particular scanning protocol, and it is also referred to as the beam collimation. $D(z)$ is the dose profile along the *z*-axis. CTDI is measured in axial scan mode for a single rotation of the x-ray tube, and its value approximates the average absorbed dose, along the *z*-axis, of a scan volume consisting of multiple, contiguous CT scans [6]. In this report, it was recommended to use the polymethylmethacryte (PMMA) phantoms with standard dimensions of 160 mm for head dose measurements and 320 mm for body dose measurements.

A commercially available 10 cm pencil-type ionization chamber (3 cm^3 active volume) is

[1] The concept of computed tomography dose index CTDI as a dose metric for CT scanners was introduced earlier in 1981 by Shope et al. [23]

used to carry out clinical measurements of CTDI. The value obtained is the accumulated dose at the center of a PMMA phantom for CTDI measurements of a 100 mm scan, but it underestimates doses for longer scan lengths, as it does not take into consideration the contribution to the total dose of the profile's tails beyond the $\pm$ 50 mm integration range.

$$CTDI_{100} = \frac{1}{NT} \int_{-50\ mm}^{50\ mm} D(z)\, dz. \qquad [1.2]$$

$CTDI_{100}$ values vary as a function of the measurement point across the $xy -$ plane, so a useful concept to characterize the CT scanner output for a particular imaging setting (kVp and mAs) is the so called weighted $CTDI_w$, and it is defined as:

$$CTDI_w = \frac{1}{3} CTDI_{100}^{center} + \frac{2}{3} CTDI_{100}^{edge}. \qquad [1.3]$$

Nevertheless, $CTDI_w$ is not considered a dose descriptor, *per se*, because it does not take into account the x-ray beam gaps or overlaps due to consecutive rotations of the radiation source around the patient. For the case of helical acquisitions, the $pitch$ is defined as the ratio of the imaging couch translation in the *z*-direction per rotation (Δz) to the nominal beam collimation ($N \cdot T$):

$$pitch = \frac{\Delta z}{NT}. \qquad [1.4]$$

Gaps between x-ray beams occur when the couch translation is larger than the beam collimation ($pitch\ > 1$). In this case, $CTDI_W$ overestimates the real dose. On the other hand, when the beam collimation is larger than the couch translation ($pitch\ < 1$) x-ray beams overlap, so $CTDI_W$ underestimates the actual dose. Hence, *pitch* can be seen as a proportional factor used to describe CT dose to a CTDI phantom for consecutive x-ray tube rotations to correct $CTDI_W$ measurements. This corrected value is known as the volumetric weighted CTDI ($CTDI_{vol}$), and it is defined as:

$$CTDI_{vol} = \frac{CTDI_w}{pitch}. \qquad [1.5]$$

$CTDI_{vol}$ estimates the average dose to a PMMA phantom along a 100 mm scanning length, but it cannot be considered as actual dose to the patient, as patient shape, attenuation coefficients, and scanning length affect the total energy deposited in the imaged volume [24]. A recent AAPM report on the future of CT dosimetry addressed this and other issues related to the limitations of current dose descriptor [25]. The task group No. 111 on CT dosimetry proposed a unified theory for CT dose measurements for all the available CT acquisition modes (axial, helical, fan-beam and cone-beam) based on the concept of equilibrium dose (*ED*) rather than the commonly used CTDI parameter [25].

1.5 Radiochromic film-based dosimetry

The purpose of the present work is to provide the clinical feasibility study of a protocol for the measurement of $CTDI_{vol}$ values on CT scanners and kV CBCT devices as a part of QA tests based on Gafchromic® XR-QA2 films. The current paradigm in CT dosimetry is based on the use of ionizing chambers to measure dose imparted to a CTDI phantom, but during earlier stages other dosimetric methods were also explored (TLDs in particular). Dixon and Ekstrand [26] proposed the use of radiochromic films for dose assessment in CT scanners for the first time in 1978. Kodak XV-2[2] films were used to record dose distributions around a cylindrical water-filled phantom. The accuracy of $\pm$ 15 % was reported for several CT simulators in the study of Dixon and Ekstrand.

In 2010, Tomic *et al*. proposed a two-dimensional reference dosimetry technique for measuring dose maps from kilovoltage photon beams in CBCT examinations based on radiochromic films [27]. They defined an air-kerma in air-based reference dosimetry protocol using the Gafchromic® XR-QA film model to convert net reflectance change due to exposure to ionizing radiation to dose to water. Despite the non-water equivalence of the film's sensitive layer, this dosimetry protocol ignores the composition of the film's sensitive layer and only requires the use of air-to-water mass-energy absorption coefficients, as recommended by the AAPM report on kilovoltage dosimetry [28]. The film-based method provided 1σ dose measurements uncertainties of up to 3% for kV CBCT acquisitions. Additionally, the acquired surface dose to phantom data

[2] The XV-2 is a radiochromic film developed by Kodak (Rochester, United States) for photon-beams dosimetry. It possesses a low saturation dose ($\sim 100\ cGy$) which can be used in CT dosimetry [26].

were consistent with the tabulated and Monte Carlo (MC) simulated data, demonstrating the applicability of the radiochromic film dosimetry system for dose measurement in the imaging energy range [26].

Boivin *et al*. in 2011 adopted the same dosimetry protocol [29]. They used the film protocol to assess dose-phantom profiles and *in vivo* entrance dose values for patients undergoing regular CT-scans. Their work aimed to measure surface dose in phantoms and patients, as well as the experimental dose length product[3] (DLP) in patients. They obtained results congruent with a 1σ uncertainty below 3% for doses between 1 and 200 mGy. The *in vivo* dose measurements were reported, including maximum surface dose (up to 97 mGy for head scans and up to 86 mGy for abdomen protocols), impossible to obtain with regular ionization chambers or TLD-based methods, due to their low spatial resolution. Boivin *et al*. recommend replacing the homogeneous CTDI model by an improved and validated anthropomorphic dosimetry system [29].

Rampado *et al*. suggested in 2010 the use of radiochromic films to carry out CTDI measurements in conjunction with PMMA phantoms [31]. In their approach, film strips were used to replace the pencil-type chamber in the phantom, and posterior film analysis was conducted for average dose assessment and $CTDI_{vol}$ values estimations. Rampado *et al.* compared film-measured CTDI values with ionization chamber-collected data and reported differences of up to 9% for beam collimations above 10 mm in head and body multi-axial scans. In this case, 1σ uncertainties of 5% were reported in dose to the phantom measurements.

[3] DLP is defined as the product of $CTDI_{vol}$ and the scan length. (Slice thickness $\times$ number of slices). Its value is independent to the imaged object, so it is not an actual dose descriptor. Nevertheless, some proportional factors can be used to convert DLP into related effective dose. [30].

2. Materials

2.1 Gafchromic® XR-QA2 film

The Gafchromic® XR-QA2 film by Ashland *Inc*. (Covington, USA) is manufactured specifically for QA tests in radiology, for kilo-voltage imaging beam qualities at low energies (~ 20 kVp $-$ 200 kVp). The opaque-laminated film consists of an active layer (25 microns thick) sandwiched between two layers of polyester laminate (97 microns thick), as shown in ***Figure 2.1***. Heavy elements composing the active layer ($Z_{eff} = 7.14$) interact with low energy photons, principally via photoelectric effect. The active layer of the film is sensitive to doses between 1 mGy to 200 mGy.

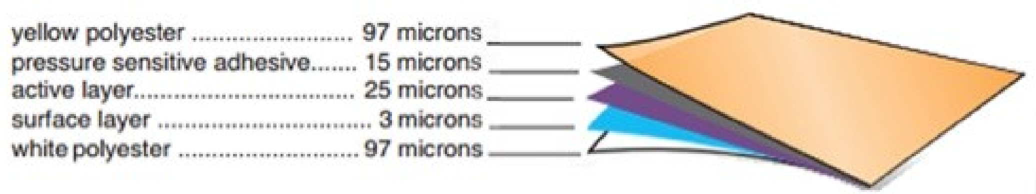

Figure 2.1. Design of the Gafchromic® XR-QA2 film. [32].

The principal features of the film, according to the manufacturer, include high resolution (5000 dpi) and improved contrast. Another feature is the film's non-sensitivity to visible light and high data integrity. In total, 30 sheets of size $10'' \times 12''$ were used in this study (lot #: A07091204). The composition of the film and relative amounts of component elements (by weight) are shown in T***able 2.1.***

Layer	Z_{eff}	Composition (%)					
		C	H	O	N	Li	Cl
Active Layer	7.14	25.0	54.2	9.6	10.4	0.7	0.1
Surface layer	6.84	22.5	53.3	11.1	12.7	0.2	0.2
Polyester	6.64	45.5	36.4	18.2	0.0	0.0	0.0

Table 2.1. Gafchromic® XR-QA film composition [32].

2.2 PMMA phantom for CTDI measurements

The polymethyl methacrylate (PMMA) phantom for *CTDI* measurements, produced by Radcal Corporation (Monrovia, USA) was used to mimic patients' head and body. It is a phantom designed to hold a pencil-type ionization chamber inside of it in order to measure CTDI values. The phantom consists of two cylinders (Head: 160 mm diameter and Body: 320 mm diameter) containing 13 mm diameter holes in their periphery and center that serve to place cylindrical radiation detectors. The head phantom incorporates a central hole and additional four holes at 10 mm depth from the edge separated by 90°, as shown in ***Figure 2.2***. The body phantom includes four peripheral holes and a 160 mm diameter cavity in the center to be coupled to the head phantom. The tool set includes holders to stabilize the phantom and nine PMMA cylindrical rods to be placed in the holes in the absence of radiation detectors.

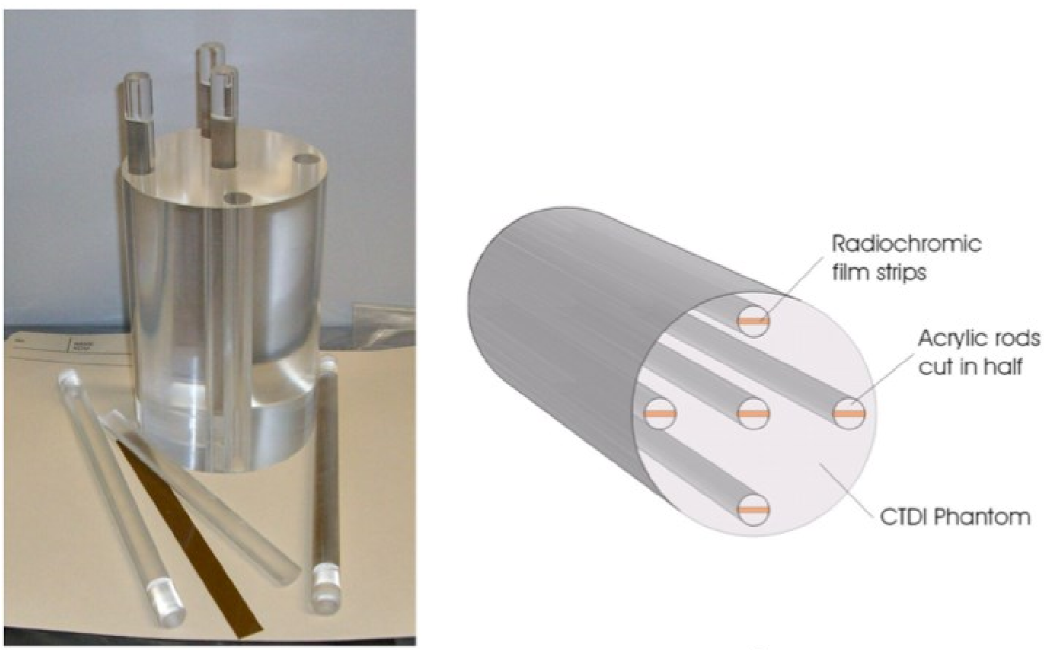

a b

Figure 2.2. The head CTDI phantom and a set of PMMA rods (a). Scheme of a set of PMMA rods modified to hold radiochromic films into the head CTDI phantom (b).

2.3 Reference ionization chamber

The reference ionization chamber that was used in this study was the NE 2557C model manufactured by NE Technology (Reading, United Kingdom). This is a farm-type ion chamber with $0.2\ \mathrm{cm}^3$ active volume. It consists of a thin-walled thimble made of high-purity graphite protected by a detachable build-up cap and an aluminum electrode. This model may be used to measure radiation in the energy range $0.05 - 35.0\ \mathrm{MV}$. It has a sensitivity of $11.7\ \mathrm{rad/nC}$ and measures a maximum dose rate of $3.5\ \mathrm{krad/min}$ [33].

The ionization chamber used for CTDI measurements was the L-30009 CT model by Ludlum Measurements *Inc.* (Sweetwater, USA). It is a pencil-type chamber designed specifically for dose length product and dose length rate measurements. It has a $3.14\ \mathrm{cm}^3$ sensitive volume defined by a graphite-coated thin-wall ($100\ \mathrm{mm}$ length, $3.5\ \mathrm{mm}$ radius) and an aluminum electrode. This chamber has a nominal response of $14\ n\mathrm{C/Gy \cdot cm}$ and works at a maximum dose rate of $12.4\ \mathrm{Gy/s}$ [33].

The electrometer used in this study was the 6517a by Keithley Instruments (Solon, USA). It operates at 125 readings/s and can be used to measure current (1 fA – 20 mA), voltage (10 μV - 200 V), resistance (5 Ω - 10^6 Ω) and charge (10 fC - 2 μC). The manufacturer reports the accuracy of 0.4 % when the device is used to measure charge at the nC scale [34].

2.4 Flatbed document scanner

The Epson Expression 10000XL flatbed scanner by Epson America (Long Beach, USA) is a high performance scanner for large-volume documents. The 48-bit flatbed color image scanner has an optical resolution of 2400 dpi, $12.2'' \times 17.2''$ scanning area, and a maximum color scanning speed of $16.0\ \mathrm{ms/line}$. This document scanner has been previously used in film dosimetry protocols [27, 29 and 31]. Rampado *et al.* reported average 1σ uncertainties about 5 % in dose measurements when this particular model was used to read irradiated film samples in comparison to the 8 % uncertainty reported for other scanner brands [31].

2.5 Radiation sources

2.5.1 Orthovoltage X-ray Therapy Unit: Xstrahl 300 is an x-ray therapy system by Xstrahl Limited (Surrey, United Kingdom). It provides x-ray beams in the range between 40 and 300 kVp, works at tube currents from 0 up to 30 mA, and delivers a maximum dose rate of ~300 cGy/min. The field size ranges from 1.5 cm diameter up to $20 \times 20\ \text{cm}^2$ square [35].

2.5.2 Computed Tomography Simulators: The General Electric LightSpeed® CT Simulator is a third generation CT simulator developed by General Electric (Fairfield, USA). Its gantry is 80.0 cm in diameter, and wider than generic CT scanners which facilitates patient positioning. The generator achieves a maximum of 440 mA at 120 kVp. The x-ray tube rotations of 1 up to 4 seconds define sweeps an imaging area (Field Of View, FOV) in the range between 50 and 70 cm in diameter. The system minimum beam collimation is 2×0.625 mm and the maximum is 16×1.25 mm [36].

The Brilliance® CT Big Bore by Philips (Amsterdam, Netherlands) possesses an 85.0 cm diameter gantry aperture, and the minimum and maximum beam collimation available for the system are $2 \times 0.75\ mm$ and $16 \times 0.75\ mm$ respectively. It includes internal filtration for head and body imaging protocols. A 0.44 s 360°-rotation of the x-ray CT assembly defines a reconstruction Field Of View (FOV) that ranges between 50 and 700 mm. As for the x-ray tube, it delivers photon beams of peak energy 90, 120 and 140 kVp with tube currents from 20 up to 500 mA in 1mA increments [37].

2.5.3 Cone-Beam CT device: The On-Board Imager® (OBI) by Varian (Palo Alto, USA) was used in this study. It is a kV imaging system coupled to linear accelerators. It is clinically used for patient verification and repositioning. For CBCT data acquisition, the x-ray tube delivers beams in the peak energy range of 40 and 140 kVp. The mAs varies between 0.1 and 1000, and the device offers slice thicknesses from 1 mm up to 10 mm in 0.5 mm increments. For large object imaging protocols, the CBCT scan is acquired after a full gantry rotation that defines a 45 cm diameter FOV. For small imaged bodies, the gantry moves through 200° and defines a 25 cm diameter FOV [38]

Three clinical accelerators with OBI systems were used: the Clinical iX Linear Accelerator, the TrueBeam System and the Trilogy Linear Accelerator, all of them by Varian.

2.6 Film Analysis user code

The film analysis was performed with an in-house code written by the author of this thesis in Matlab. Matlab is a high-level, forth generation programming language for numerical computation, modeling and programming developed by MathWorks (Natick, USA). The version 7.13 of Matlab was used to create a film analysis application suitable to read information out of film TIFF images and report relevant dosimetric information. The code was split into two modules. The first part was dedicated to the elaboration of calibration curves, while the second module served exclusively to create dose maps and dose profiles out of an irradiated set of films. This last step includes the determination of CTDI values according to the imaging protocol followed to expose the films. This code is described in detail in ***Section 5.4.1***.

3. Protocol for Clinical CTDI Measurements

The Gafchromic® XR-QA2 film-based dosimetry system for $CTDI$ measurements includes sources of uncertainty in all the protocol steps. Some of them are directly related to the inherent characteristics of the film, such as its orientation and effective energy (E_{eff}) dependence. Other sources of uncertainty are related to the calibration system and the measurement procedure itself. This chapter contains a general description of the protocol proposed to carry out CTDI measurements with radiochromic films. Furthermore, a concatenated report of the tests performed in order to estimate the individual uncertainty associated with each protocol steps is presented in the subsequent section. An outline of the $CTDI$ measurement protocol is schematized in ***Figure 3.1***. The procedure consists of six consecutive steps, starting from the film irradiation in phantom and ending with the calculation of volumetric CTDI values.

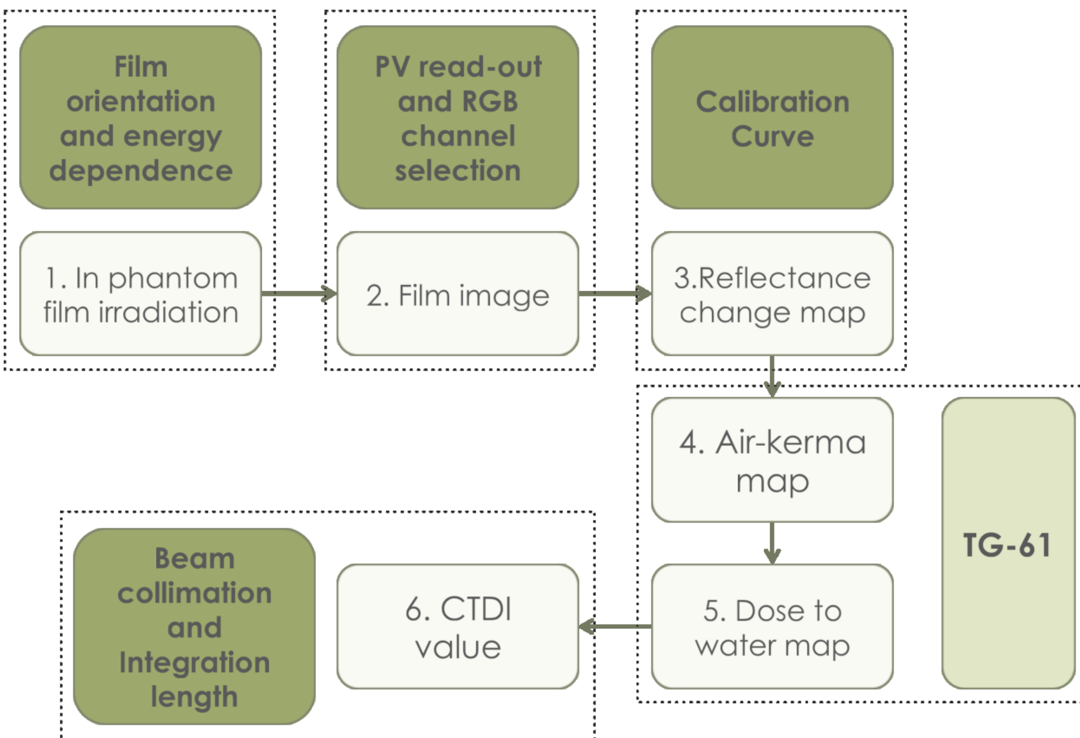

Figure 3.1 Protocol for clinical $CTDI$ measurements; steps in white boxes, and their associated sources of uncertainty in green boxes. The TG-61 protocol provides an estimated combined uncertainty (1σ) in dose to water measurements using an ion chamber calibrated in air in terms of air-kerma [28].

3.1 In-phantom film irradiation

The film-based protocol for clinical *CTDI* measurements starts with the irradiation of a sandwiched set of films correctly set in place inside of a PMMA phantom for CTDI measurements. Each piece of film is labeled with a code that indicates the imaging protocol employed to scan the phantom, the beam quality, and a code describing its position inside of the phantom. ***Table 3.1*** describes the codes used to keep track of the films, and ***Figure 3.2a*** presents an example of a labeled film.

Category	Symbol	Description
Protocol name	H, B, P, T	Head (16 cm diameter phantom), Body, Pelvis, Thorax (32 cm diameter)
	1, 2, 3	Three sets of films were used during each measurement
Beam Quality	80, 100, 120, 140	Peak energy (kVp)
	A, H, B	Filter: Air, Head, Body
In phantom localization	U, R, B, L, C	Up, Right, Bottom, Left, Center

Table 3.1 Films for CTDI measurements labeling.

a. b. c.

Figure 3.2. a) Example of the first film placed into the "UP" hole of the body phantom to be scanned by a 'Thorax" imaging protocol; a 120 kVp beam hardened by the "Body" filter was used. b) Piece of film sandwiched by a PMMA rod cut in a half and placed into the body phantom. c) A CTDI phantom holding a set of five films ready to be scanned.

The PPMA phantom for CTDI measurements includes five holes ($16\ \mathrm{cm}$ depth, $1\ \mathrm{cm}$ diameter) originally designed to place in a pencil-type ionization chamber. In order to replace the pencil-type detector with a film strip, five PMMA rods with the same phantom holes dimensions were cut in a half and used to sandwich a $10 \times 150\ \mathrm{mm}^2$ strip of film without air gaps in the middle, as shown in ***Figure 3.2b*** and ***Figure 2.2***.

The PMMA rods holding the films are placed into their corresponding holes, and the phantom is placed on the couch of the imaging device (CT Simulator or Linac). The laser system in the treatment room is used to align the phantom in such a way that its central hole is parallel to the $z-$axis of the machine and crosses its isocenter. Finally, each rod in the periphery of the phantom is rotated in order to have the active layer of the film facing the surface of the phantom. ***Figure 3.2c*** depicts the setup. Each measurement is repeated three times in order to increase the precision of the procedure. Additionally, a non-irradiated control strip of film accompanies the set of irradiated films, so a total of 16 films are used to measure the CTDI value of a particular imaging protocol.

3.2 Generation of film images

With the purpose of comparing any change in the reflectance of the films due to the absorption of energy during an imaging protocol, the set of films is scanned with the document scanner before and after the irradiation. Each imaging protocol is repeated three times in order to estimate the corresponding CTDI value. In total, sixteen film strips are scanned twice by the *Epson 10000XL* flatbed document scanner; five pieces per repetition plus a unique control piece.

The software image acquisition settings remained constant for each set of films. The images were acquired in reflection mode, at 127 dpi ($0.2\ \mathrm{mm/pixel}$), and saved in *Tagged Image File Format* (***TIFF***). On the scanner screen, the films of each set were placed in a particular order. Namely, they were positioned horizontally with the control film in first position, followed by the peripheral films and the central film at the bottom of the column.

Desroches *et al.* in 2010 studied the effect of scan orientation and positioning of EBT and EBT2 radiochromic films[4], manufactured by Ashland Inc. (Covington, USA), over the scanning area of a document scanner on the proprieties of the acquired images [39]. Desroches *et al.* reported systematic errors up to 17.8% in dose measurements due to misalignments or rotations of the films. The recommendations included in that study have been used in this protocol to take advantage of the sensitivity, uniformity, and behavior of the scanner elements to enhance the quality of the images:

- The so-called lateral effect compromises the quality of the images, so defects in the homogeneity of the image are more evident when the document is close to the edges of the scanning screen. To avoid this undesirable effect, the films were placed at the center of the scanning screen.
- The quality of the film images also varies with the film's orientation with respect to the direction swept by the scanner light source. The image is more uniform when the film's coating direction is parallel to the scanning direction. Consequently, the film strips were placed on the scanner screen parallel to each other and in the same direction of the light source movement, *i.e.* with the longer side parallel to the light source movement direction.

The photopolymerization process of the active layer due to the absorption of ionizing energy continues over time even after the irradiation of the film [32]. The reflectance (R) of the film varies slightly during the first hours following its irradiation, and up to 4% within the seven hours following exposure. The time required for the film to reach a final appearance is known as the processing time, and for radiochromic films it is about 24 hours [32]. This means that the images of the film should be scanned at least one day after the irradiation.

3.3 Film response map, ΔR_{net}

The response of the film to the ionizing radiation was assessed in terms of the *net change in the*

[4] The Gafchromic® EBT and EBT 2 models are radiochromic films manufactured by Ashland (Kentucky, United States) for kilo and mega-voltage photon and electron beam dosimetry in the 0 – 50 Gy dose range.

reflectance (ΔR_{net}) of the acquired image. The *reflectance* R of a pixel is defined as:

$$R = \frac{PV}{2^{16}}, \quad [3.1]$$

which is the normalization of the *Pixel Value* (PV) to its maximum possible value ($2^{16} \rightarrow 4$ channels, 4 bits per channel). The in house-written Matlab code described in ***Section 5.4.1*** was used to produce a reflectance map ΔR_{net} of the $m \times n$ pixel^2 images. The code also compares the reflectance map for the same film before and after irradiation in order to obtain the *change in reflectance* (ΔR) map:

$$\Delta R = R_{After} - R_{before}. \quad [3.2]$$

Finally, in order to eliminate any additional effect of the environment on the film response (temperature, humidity, other radiation exposure, *etc*.), the average change in reflectance of the control film ($\overline{\Delta R}$) is subtracted from the reflectance change map of the film to obtain the net reflectance change map ΔR_{net}, as shown in ***Figure 3.3***.

$$\Delta R_{net} = \Delta R^{film} - \overline{\Delta R}^{control}. \quad [3.3]$$

In such a way, a matrix ΔR_{net} named response map contains the net reflectance change values for each pixel of the irradiated image of dimensions $n \times m$ pixel^2.

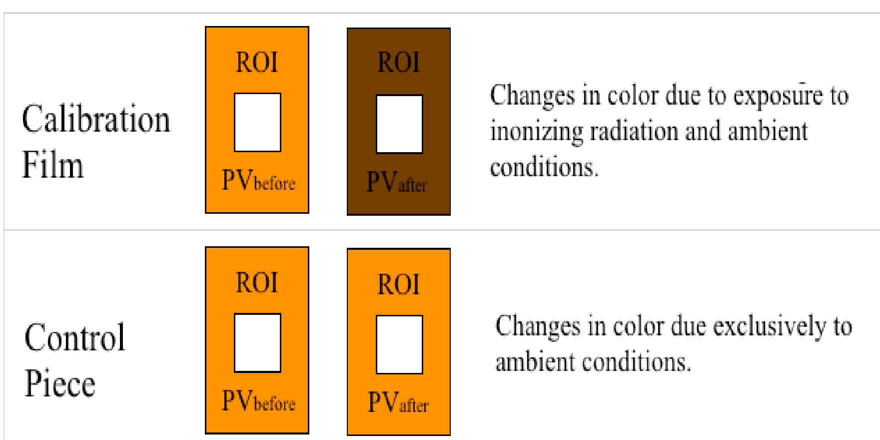

Figure 3.3 Scheme of the control film's role.

Several assumptions underline this step. The first one is related to the impossibility of comparing one-to-one exactly the same point of a film before and after irradiation to assess the change in reflectance at that point. This is due to the fact that, in general, the reflectance maps before and after irradiation for the same film don't have the same size. Although the software for film analysis identifies the shape of the scanned film by comparing its interior values to the background and corrects its orientation to produce a non-tilted map of the film, the film's original orientation on the scanner screen during the scanning process, or any other modification of the film's shape due to its manipulation, may alter the size of the reflectance map. To avoid this problem, the reflectance maps are reduced to their minimum common value in each direction, i.e. a $n \times m$ pixel^2 matrix, where n is the smallest high (in pixel) of all reflectance maps, and m is the smallest reflectance maps base (in pixel). An air-kerma in air map and a dose to water map are subsequently created from the reflectance map, and the size of these matrices remain constant. A scheme of the dose to water map and a dose profile calculation is shown in **Figure 3.4.**

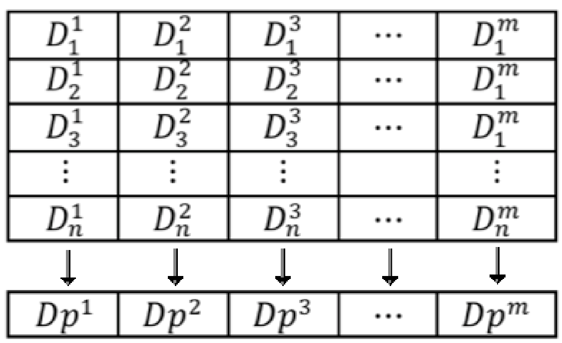

Figure 3.4. Dose to water map and profile *Dp* definition.

3.4 Film air-kerma in air map, $[K_{air}]_{air}$

A calibration curve is a function f_Q that describes the change in the reflectance of the film ΔR_{net} in terms of air-kerma in air values $[K_{air}]_{air}$, for a particular well-known beam quality Q:

$$\Delta R_{net} = f_Q([K_{air}]_{air}). \quad [3.4]$$

The Gafchromic® XR-QA2 CTDI dosimetry system was calibrated in terms of $[K_{air}]_{air}$ for a particular E_{eff} (beam quality Q), so each point of the net reflectance change map of the film image can be related to an $[K_{air}]_{air}$ value through the inverse function of the calibration curve. According to this dosimetry system, no additional corrections must be taken into considerations [27]:

$$[K_{air}]_{air} = f_Q^{-1}(\Delta R_{net}) \qquad [3.5]$$

Calibration curves created to be used in this study describe the change in reflectance of the film across the $[K_{air}]_{air}$ range from 5 to 100 mGy for 19 effective energies in the range from 12.7 to 64.0 keV. If the film is exposed to a different beam quality within the 12.7 – 64.0 keV range, the response of the film can be assessed by interpolating the closest well-known response functions.

In order to obtain an $[K_{air}]_{air}$ map of the film, it was assumed that the photon fluence spectrum (*i.e.* E_{eff}) of the beam remained constant throughout the phantom and the film during the irradiation, so that the calibration curve corresponding to the beam quality delivered by the imaging protocol could be used to convert net reflectance change ΔR_{net} values into $[K_{air}]_{air}$.

3.5 Film dose to water map, D_{water}

The $[K_{air}]_{air}$ map is converted directly into a dose to water in air map D_{water} via the mean mass energy-absorption coefficient ratios for water to air, as described by the AAPM Report TG-61 [27]:

$$[D^w]_{air} = [K_{air}]_{air}\left[\left(\frac{\bar{\mu}_{en}}{\rho}\right)_{air}^{water}\right]_{air}. \qquad [3.6]$$

This procedure requires two conditions to be met at low energies:

- Assuming charged particle equilibrium (CPE) in the point of measurement ($\beta = 1$), dose to water ($D^w = \beta K^{water}$) equals K^{water}

$$D^w = K^{water}. \qquad [3.7]$$

- Kerma (K), collisional kerma (k_{col}), and radiative kerma (k_{col}) are defined as $K = k_{rad} + k_{col}$, $K = \Psi\left(\frac{\bar{\mu}_{tr}}{\rho}\right)$, and $k_{col} = \Psi\left(\frac{\bar{\mu}_{en}}{\rho}\right)$. Ψ is the energy fluence of the beam, $\frac{\bar{\mu}_{en}}{\rho}$ is the mass energy absorption coefficient of the material averaged over the energy range present in Ψ, and $\frac{\bar{\mu}_{tr}}{\rho}$ is the mass energy transfer coefficient of the material. Due to the low photon energy range of the beams used in kV imaging protocols, the charged particles' energy loss via radiation can be neglected ($k_{rad} = 0$), so

$$K = k_{col},$$

$$\mathrm{K} = \Psi\left(\frac{\bar{\mu}_{en}}{\rho}\right), \text{ or}$$

$$\Psi = \mathrm{K}/\left(\frac{\bar{\mu}_{en}}{\rho}\right). \qquad [3.8]$$

This applies for water and air equally, so:

$$\mathrm{K}^{air}/\left(\frac{\bar{\mu}_{en}}{\rho}\right)_{air} = \Psi = \mathrm{K}^{water}/\left(\frac{\bar{\mu}_{en}}{\rho}\right)_{water},$$

and so, the water-kerma in air $[K^{water}]_{air}$ can be defined as:

$$[K^{water}]_{air} = [K_{air}]_{air}\left[\left(\frac{\bar{\mu}_{en}}{\rho}\right)^{w}_{air}\right]_{air}. \qquad [3.9]$$

The value for a particular position of the response map, and therefore the dose map, is related to the macroscopic change in the appearance of the film due to the polymerization process that followed its irradiation. This value is related to the dose absorbed by the active layer of the film during the irradiation, but it also depends on the processing time that followed the irradiation, the ambient conditions of the place where the film was stored before being scanned, and the scanning process itself. The processing time was kept constant for all the films ($t_{processing} = 24$ h), and the ambient effect on the film was corrected for the use of a control film, but some other sources of uncertainty cannot be corrected for. Those uncertainty sources are summarized in the ***Section 5.4.***

3.6 CTDI value determination

The CTDI as defined in ***Equation 1.1***, integrates the dose function $D(z)$ along the $z-$ axis of the phantom. This definition was modified by replacing the integration of a continuous function by the sum of discrete dose data acquired with the film protocol. The line integration has been replaced by a sum over the elements of a dose profile Dp, whose m elements are the average values of the D_{water} map columns (D_{water} is a $n \times m$ matrix).

$$Dp_i = \frac{\sum_{x=1}^{n} D_i^x}{n}. \quad [3.10]$$

The CTDI value for a film piece is defined then as:

$$CTDI_{XR-QA2} = \frac{1}{nT}\left(\sum_{i=1}^{m} Dp_i\right)\Delta x. \quad [3.11]$$

Where nT is the length of the channels used by the CT scanner to collect data (sometimes referred to as beam collimation), and Δx is the length of a pixel. In the case of a $CTDI_{100}$ calculation, $m = 500$, so the integration length equals to 10 cm. Five $CTDI_{film}$ values calculated from ***Equation 1.2*** for a particular set of films are then used to obtain the weighted CTDI:

$$CTDI_w|_{XR-QA2} = \frac{1}{3}CTDI_{center} + \frac{2}{3}average(CTDI_{periphery}). \quad [3.12]$$

Finally, for the case of helical scans, the volumetric CTDI value is calculated using ***Equation 1.5***

$$CTDI_{vol}|_{XR-QA2} = \frac{CTDI_w|_{XR-QA2}}{pitch}. \quad [3.13]$$

4. Film Response

4.1 Film-image pixel value read-out

The response of the film to different $[K_{air}]_{air}$ values was defined in terms of its net reflectance change (***Section 3.3)***. Following this definition, an average response value $\Delta\bar{R}_{net}$ was calculated inside a ROI defined at the geometrical center of each calibration film's irradiated zone. In addition to the process of film irradiation and its intrinsic characteristics, the use of a calibration curve that converts measured change in reflectance into $[K_{air}]_{air}$ (and subsequently into dose to water) also contributes to the total uncertainty in the CTDI measurements. The precision of any CTDI value determination is limited by the uncertainty associated with each step in the dosimetry protocol. One of these sources of uncertainty arises from the way the flatbed document scanner produces the image, as well as the way the pixel values of such an image is read out.

The $[K_{air}]_{air}$ map determination requires the use of a calibration curve for the corresponding beam quality delivered during the imaging protocol. The total uncertainty associated with the calibration curve includes an experimental and a fitting component. Both uncertainties depend on the *Standard Deviation* (SD) of the *Pixel Value* (PV) inside the chosen *Region of Interest* (ROI) on the image of the calibration films. It is recommended to reduce as much as possible the *SD* by selecting the appropriate *ROI* size and geometry. The *Red, Green, or Blue* (RGB) channel selected to read out the PV from the scanned images also plays a role in the optimization of the dosimetry protocol accuracy, as described in ***Section 4.2.1*** to ***Section 4.2.3***

4.2 Region of Interest size effect

A set of 9 calibration films was exposed to well-known $[K_{air}]_{air}$ values (from 5 to 100 mGy) by a 46.9 keV beam delivered by the General Electric LightSpeed® CT simulator described in ***Section 2.5.2***. Images obtained from the irradiated films were then used to create multiple calibration curves for a 120 kVp without filtration beam, and to assess their average experimental, fitting, and total uncertainty as a function of the *ROI* size used to read out the *PV* on the images, as shown in ***Figure 4.1.***

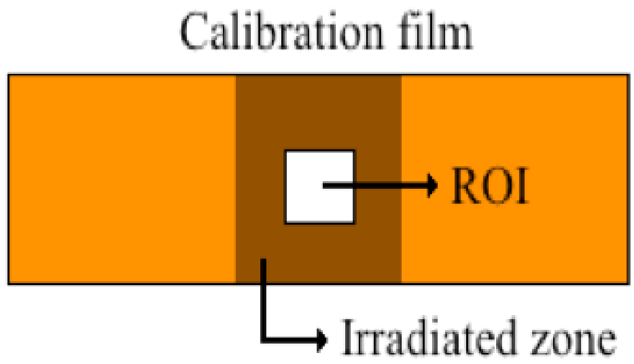

Image 4.1. Scheme of the *ROI* defined inside of the irradiated zone of a calibration film.

In order to cover the *ROI* size range from 4 to 400 pixel^2, seven calibration curves were created for the same beam quality by choosing squared *ROI* of dimension ranging from 2×2 to 20×20 pixel^2. The average fitting, experimental, and total uncertainty associated to each calibration curve was plotted as a function of the *ROI* area, $\bar{\delta}_T(ROI)$.

Each calibration curve was elaborated by reading out the PV and its SD inside a ROI centered in the irradiated film. The size of the ROI varied from 4 to 400 $pixel^2$. Subsequently, for each calibration curve, the experimental, fitting, and total uncertainties were calculated as a function of $[K_{air}]_{air}$, this is: $\delta_{exp}([K_{air}]_{air})$, $\delta_{fit}([K_{air}]_{air})$, and $\delta_T([K_{air}]_{air})$ in ***Equations 5.11 – 5.13*** of ***Section 5.3***. Finally, uncertainties for the same calibration curve, i.e. *ROI* size, were averaged over the $[K_{air}]_{air}$ range 5 – 100 mGy and plotted in ***Figure 4.2*** as a function of the *ROI* size used to create the corresponding calibration curve.

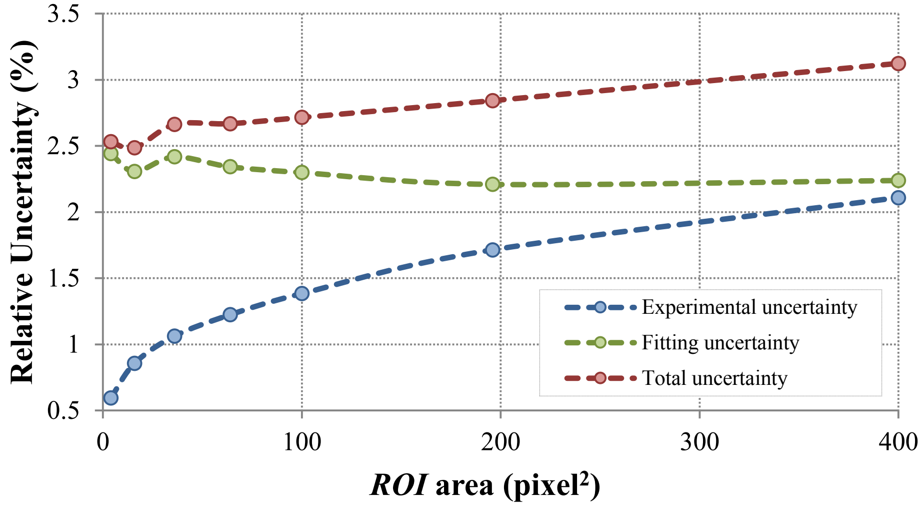

Figure 4.2. Relative uncertainty in the change of reflectance of the film as a function of the *ROI* area for 120 kVp without filter on GE LightSpeed® CT Simulator.

Averaged experimental uncertainty $\delta_{exp}(ROI)$ increases with the size of the *ROI*, while fitting uncertainty $\delta_{fit}(ROI)$ is almost constant and always larger than the experimental uncertainty. $\delta_{exp}(ROI)$ increases with the *ROI* area as a consequence of the film inhomogeneity, but $\delta_{fit}(ROI)$ is relatively stable because it depends on the standard error (SE) of the fitting function coefficients obtained through a minimum square minimization algorithm for the same number of iterations ($\sim$15), as described in ***Section 5.4.1***.

As shown in ***Figure 4.2***, if the reference *ROI* size is set at 100 pixel^2, the average total uncertainty of any $[K_{air}]_{air}$ measurement between 0 and 10 cGy is about 2.7 %, but by quadrupling the *ROI* size, such an uncertainty increases up to 3.1%. As an example, ***Figure 4.3*** compares the total uncertainty in ΔR_{net} (***Equation 3.3***) of two calibration curves created to describe the film response to low energy photon beams (38.8 keV) in the $[K_{air}]_{air}$ range between 0 and 10 cGy. It is seen that for very low $[K_{air}]_{air}$ values (< 5 mGy), the total uncertainty $\delta_T([K_{air}]_{air})$ is the same regardless of the *ROI* size. The difference between the 100 pixel^2 and 400 pixel^2 associated uncertainties becomes more noticeable when $[K_{air}]_{air}$ increases above 10 mGy. In accordance with these results, the *ROI* size selected to read-out the calibration films during the CTDI protocol was 100 pixel^2.

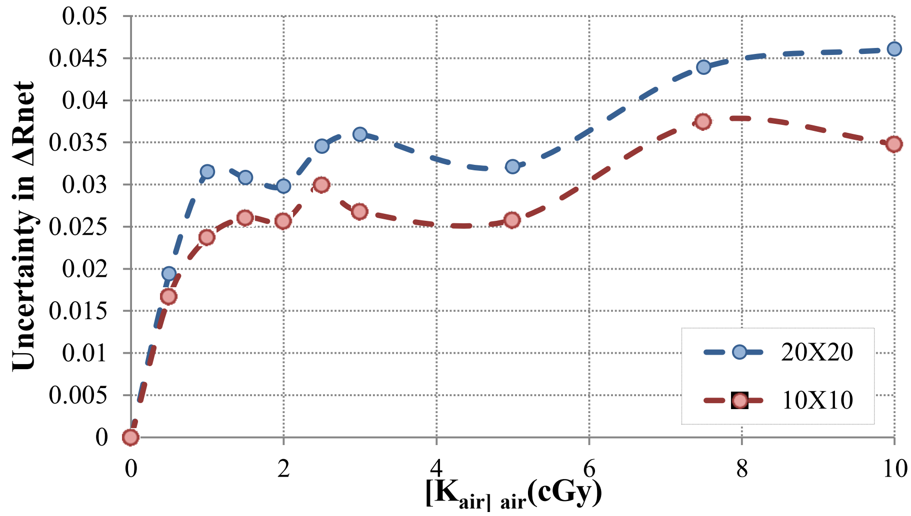

Figure 4.3. Effect of the *ROI* size on the total uncertainty for an 80 kVp (without filtration) calibration curve.

4.3 Region of Interest geometry effect

The shape of the *ROI* inside of the irradiated zone of the calibration films also may have an effect on the total uncertainty $\delta_T([K_{air}]_{air})$ in the ΔR_{net} of the calibration curve. The influence of the *ROI* geometry on the *SD* of the *PV* inside of the ROI was assessed.

Two *ROI* shapes were compared in terms of the total uncertainty (ΔR_{net}, ***Equation 3.3***) linked to the calibration curves produced by each geometrical arrangement. A set of 11 calibration films was irradiated to $[K_{air}]_{air}$ values in the range from 0 to 100 mGy by an 80 kVp beam without filtration. The set of films were used to create the corresponding calibration curve. Geometry A, named "1 *ROI*", was a 100 $pixel^2$ squared region with its center matching the middle point m of the irradiated zone on the film. Geometry B ("5 *ROI*") consisted of five rectangular regions, 20 pixel^2 each. The center of one of them matched point m, and the four additional regions were placed around it (***Figure 4.4)***

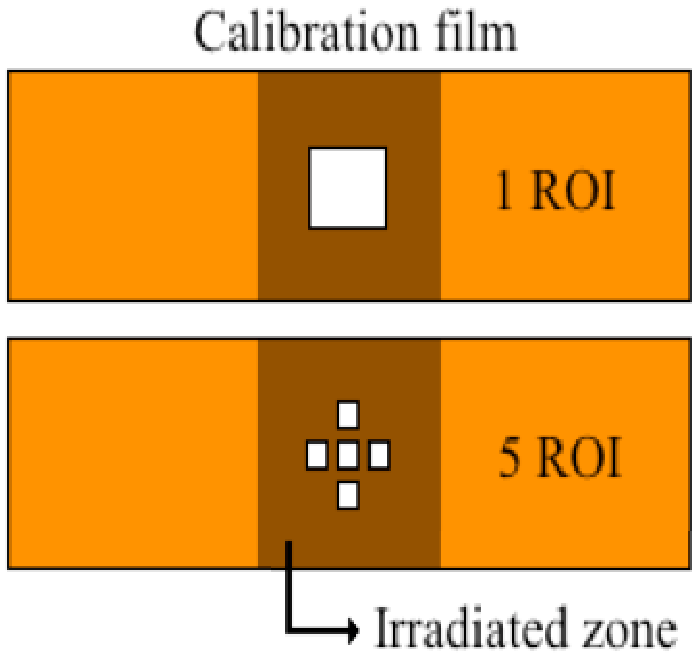

Figure 4.4. Scheme of the *ROIs* studied to assess the effect of its geometry on the total uncertainty in the change of reflectance of the film.

The average *PV* and its standard deviation were calculated to create a calibration curve for a low energy photon beam (38.8 keV), and the total uncertainty for both geometries was plotted as a function of $[K_{air}]_{air}$, as shown in ***Figure 4.5***.

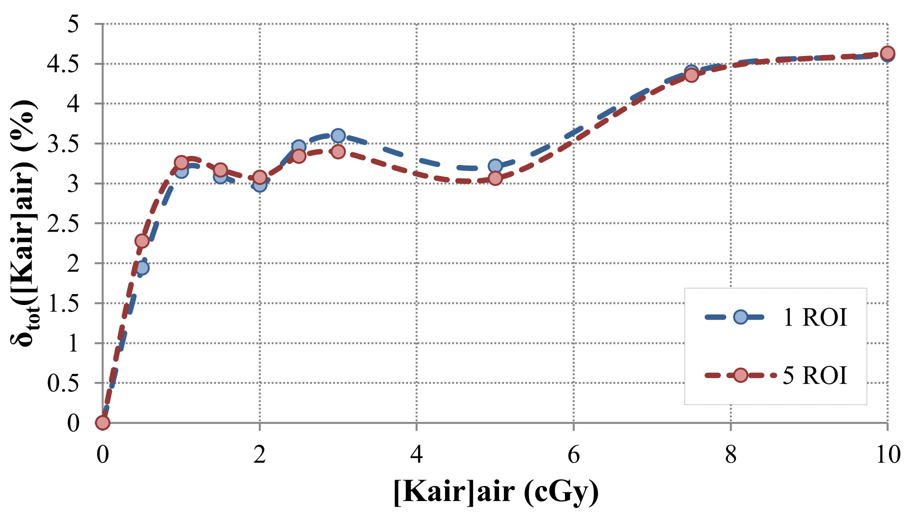

Figure 4.5. Effect of the *ROI* geometry on the film response uncertainty.

The total uncertainties of both calibration curves as a function of $[K_{air}]_{air}$ values were compared:

$$\delta_T([K_{air}]_{air})|^{difference} = \delta_T([K_{air}]_{air})|^{1\,ROI} - \delta_T([K_{air}]_{air})|^{5\,ROI}. \qquad [4.1]$$

The results of the test indicate that there are no considerable differences in the total uncertainty of the calibration curves. Thus, for simplicity the *ROI* geometry selected to read-out the calibration films of the CTDI protocol was geometry A. ***Figure 4.6*** shows ${\delta_T}^{difference}$ as a function of $[K_{air}]_{air}$ in the $0 - 100$ mGy range. Maximum absolute differences were seen at low $[K_{air}]_{air}$ values ($5 - 30$ mGy), but total uncertainties became nearly identical as $[K_{air}]_{air}$ increased. The average absolute uncertainty difference over the whole range was calculated to be:

$$\frac{1}{100\text{ mGy} - 5\text{ mGy}} \int_{5\text{ mGy}}^{100\text{ mGy}} \left|{\delta_T}^{difference}\right| d[K_{air}]_{air} = 0.13\ \%. \qquad [4.2]$$

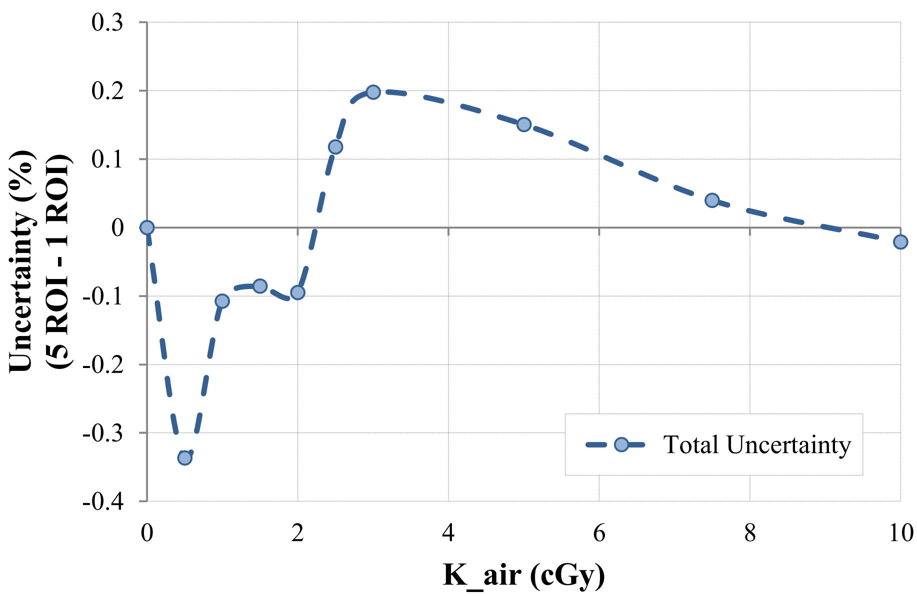

Figure 4.6. Relative uncertainty difference 1 *ROI vs*. 5 *ROI* (10×10 pixel^2) (***Equation 4.1***).

4.4 Red Green Blue channel selection effect

A set of 8 films was irradiated to known $[K_{air}]_{air}$ values in the range from 0 to 100 cGy by exposing them to a $E_{eff} = 38.8$ keV beam delivered by the orthovoltage therapy unit described in ***Section 2.5.1***. The images of the films were acquired only after irradiation. The red channel of the images was used to read out the average *PV* and its *SD* inside of a ROI in the center of the irradiated zone of each film. The *SD* values were normalized to the average *PV* and plotted as a function of the $[K_{air}]_{air}$values used to expose the films. In such a way, the Signal to Noise Ratio (SNR) of the images as a function of $[K_{air}]_{air}$ was obtained for a particular beam quality Q and red channel of *RGB* scanned *TIFF* images:

$$SNR_{Red}^{Q}([K_{air}]_{air}) = \left.\frac{SD\left(PV_{Red}([K_{air}]_{air})\right)}{\overline{PV}_{Red}([K_{air}]_{air})}\right]_{Q}, \qquad [4.3]$$

where $\overline{PV}$ indicates the average pixel value over the *ROI*. The average value of the SNR function over the $[K_{air}]_{air}$ range used to expose the films was then calculated as

$$\overline{SNR}_{Red}^{Q} = \frac{1}{(100-5)\mathrm{mGy}} \int_{5\ \mathrm{mGy}}^{100\ \mathrm{mGy}} SNR_{Red}^{Q}\, d[K_{air}]_{air}, \qquad [4.4]$$

$\overline{SNR}_{Red}^{12.7\ keV}$ describes the average *SNR* of the images created when film strips are exposed to an ionizing radiation beam of $E_{eff} = 12.7\ keV$ over the $[K_{air}]_{air}$ range $5\ mGy \leq [K_{air}]_{air} \leq 100\ mGy$. Various sets of films were used to calculate the values of $\overline{SNR}_{Red}^{Q}$ for $12.7\ keV \leq Q \leq 64.0\ keV$, and so, a description of the film signal to noise ratio $\overline{SNR}_{Red}(Q)$ was characterized over the E_{eff} range used in diagnosis radiology.

The same procedure was repeated by reading the green and blue channels of the images to obtain $\overline{SNR}_{blue}(Q)$ and $\overline{SNR}_{green}(Q)$. The SNR functions were plotted and compared as a function of the beam E_{eff}: Signal to Noise Ratio function $SNR_{color}^{Q}([K_{air}]_{air})$ were created for $Q = 12.7, 15.5, 23.5, 29.5\ 42.8$, and $64.0\ kVe$, using each of the three *RGB* channels of the *TIFF* images of films. Subsequently, these values were used to create average *SNR* functions $\overline{SNR}_{color}^{Q}$, with the results shown in ***Figure 4.7***.

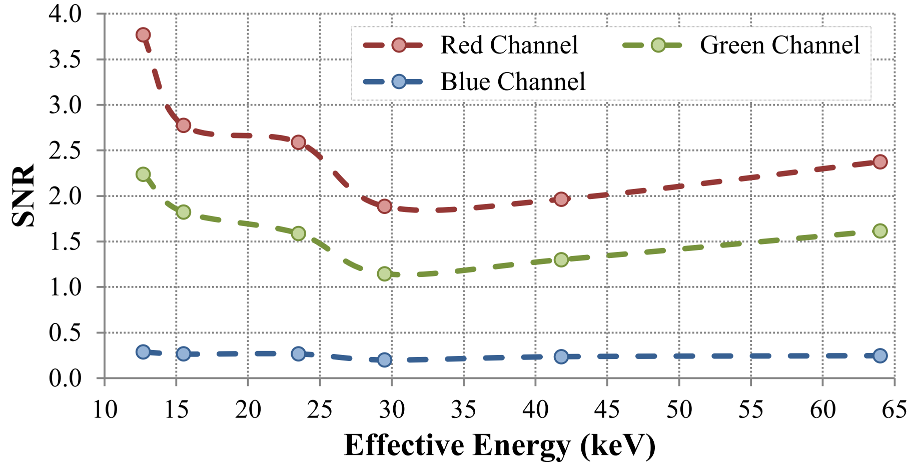

Figure 4.7 Signal to Noise Ratio (SNR) analysis for *RGB* channels.

The blue channel offered, as expected[5], the minimum average SNR values for the E_{eff} range used in the test. The *SNR* value for the blue channel averaged 0.25, being almost constant for all energies ($\sigma = 0.03$) and poorly distinguishable from non-irradiated films ($SNR_{blue}(0\text{ mGy}) = 0.50 \pm 0.22$). Green and Red channels' average SNR functions behave similarly to each other. The only difference noted is a vertical shift that provides the advantage of using the red channel over the green channel ($\overline{SNR}_{red} - \overline{SNR}_{green} = +0.94$). Both channels offer large average SNR values at the lowest studied energy ($\overline{SNR}_{red}^{12.7\ keV} = 3.77 \pm 0.83$, and $\overline{SNR}_{green}^{12.7\ keV} = 2.24 \pm 1.28$), and both decrease drastically before reaching a plateau ($\overline{SNR}_{red}^{15.5\ keV} = 2.78 \pm 1.62$, and $\overline{SNR}_{green}^{15.5\ keV} = 1.82 \pm 0.89$) that is followed by a second sharp decline to medium E_{eff} values ($\overline{SNR}_{red}^{29.5\ keV} = 1.89 \pm 1.82$, and $\overline{SNR}_{green}^{29.5\ keV} = 1.15 \pm 1.40$). At greater effective energies, average SNR functions increase linearly with nearly identical slopes ($m_{red}(29.5\text{ keV} - 64.0\text{ keV}) = 1.42 \times 10^{-2}\text{keV}^{-1}$, and $m_{green}(29.5\text{ keV} - 64.0\text{ keV}) = 1.37 \times 10^{-2}\text{keV}^{-1}$). As a result of this investigation, it was concluded that the total uncertainty of the calibration curves used to measure CTDI values would be minimized by reading-out the red channel of the *TIFF* images produced from the calibration films.

[5] Micke, Lewis and Yu published in 2010 a study on the advantages of multichannel dosimetry with radiochromic film in the dose range 10 cGy – 100 Gy. Micke *et al.* reported how the response of the film recorded in the blue channel of a *TIFF* image becomes insensitive to dose at low exposures (<160 cGy) [40].

5. Film Calibration

5.1 Film calibration process

The film response-fitting model, *i.e.* calibration curve, results from an iteration process that minimizes the squared differences between experimental data, and a bi-parametric function. The experimental data quantifies the response of the film to ionizing radiation in the range $0\ mGy < (K_{air})_{air} \leq 100\ mGy$ in terms of net reflectance change ΔR_{net}, and it depends on the beam quality Q (effective photon energy) of the beam used to expose the films:

$$\Delta R_{net} \rightarrow \Delta R_{net}([K_{air}]_{air}, Q)\ for \begin{cases} 0 \text{ mGy} < [K_{air}]_{air} \leq 100 \text{ mGy} \\ 12.7 \text{ keV } \leq Q \ \leq 64.0 \text{ keV} \end{cases}.$$

This $(K_{air})_{air}$ range was intentionally selected to cover the CTDI values delivered by CT scanners and CBCT devices during common imaging protocols. The chosen E_{eff} range also covers the operational beam qualities generally used by these systems in radiology and radiotherapy imaging procedures.

Multiple functions of $\Delta R_{net}((K_{air})_{air}, Q)$ were used to fit the experimental data (***Section 5.2***), but during the measurement procedures of the study only the one providing the lowest fitting uncertainty was used. A bi-parametric (α, β) rational function showed to fit the data well resulting in the uncertainty that was lower than any other analyzed model:

$$\Delta R_{net} = \frac{\alpha(Q) \cdot [K_{air}]_{air}}{1 + \beta(Q) \cdot [K_{air}]_{air}}, \tag{5.1}$$

where the fitting parameters are function of the beam quality $\alpha(Q), \beta(Q)$. In the proposed model, the parameter α describes the linear response of the film in the low absorbed dose region of the calibration curve, and the parameter β models the non-linear behavior for greater dose values.

The calibration film irradiation protocol differs from the CTDI measurement film irradiation protocol (***Section 3.1***). The calibration set consists of 9 films irradiated free in air $[K_{air}]_{air}$ values, in addition to a control film strip. ***Figure 5.1*** shows the calibration film irradiation setup, with films placed 12.0 cm above the CT simulator's isocenter. As the General Electric LightSpeed® CT Simulator was used to create the calibration curves, measurements were carried out to assess the machine output based on the estimates of the effective photon energy of the beams.

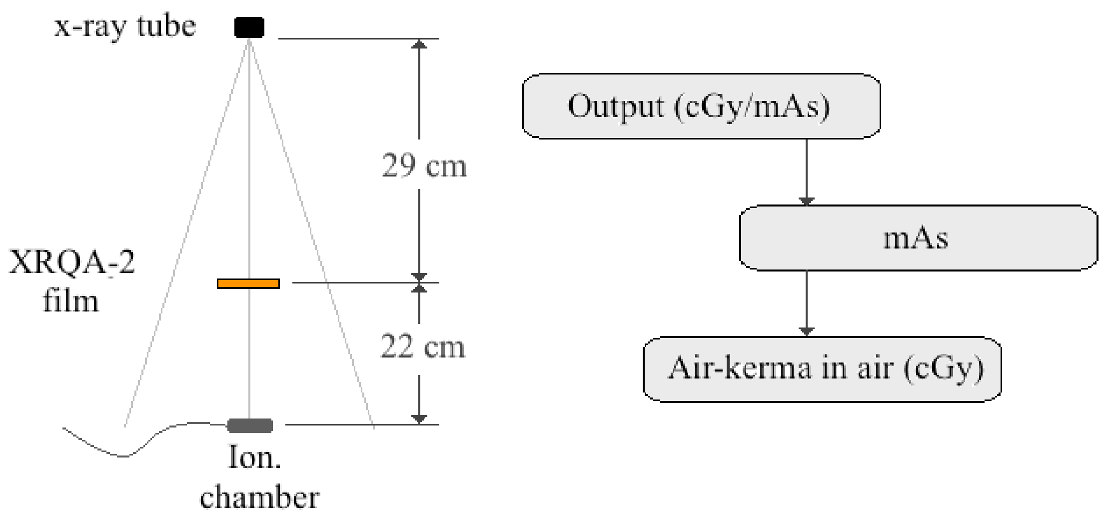

Figure 5.1. Setup for calibration films irradiation. Films were exposed to well-known $[K_{air}]_{air}$ values.

Table 5.1 shows the information required prior to the irradiation of the calibration films. The peak energy of the beam and the filter type used to harden it are used to identify a particular beam quality. This process is based on Half Value Layer (HVL) measurements. Subsequently, a direct correlation between HVL and machine output can be measured, and finally the amount of mAs needed to provide the desired $[K_{air}]_{air}$ value at the point of output measurement can be calculated. The irradiation process was monitored by an NE 2577c ionization chamber (described in ***Section 2.3***) placed under the film holder. The charge collected was normalized to its maximum value and used to scale the actual delivered $[K_{air}]_{air}$ values.

Date	2013-09-15	Scanner	LightSpeed® CT Simulator				
Peak energy (kVp)	80	Filter	Air				
Output (cGy/100 mAs)	1.1986	Output (mR/mAs)	13.6830				

Film Piece (#)	Calculated Values		Delivered Values		Measured Values	
	$[K_{air}]_{air}$ (cGy)	mAs for 3000 ms	$[K_{air}]_{air}$ (cGy)	mAs for 3000 ms	Charge (nC)	$[K_{air}]_{air}$ (cGy)
0	0.0	0.0	0.0	0.0	0.000	0.00
1	0.5	41.7	0.5	42.0	0.004	0.11
2	1.0	83.4	1.0	84	0.032	0.86
3	1.5	125.1	1.5	125	0.055	1.49
4	2.0	166.9	2.0	168	0.074	1.99
5	2.5	208.6	2.5	207	0.093	2.50
6	3.0	250.3	3.0	249	0.110	2.97
7	5.0	417.1	5.0	417	0.185	5.00
8	7.5	625.7	7.5	627	0.279	7.53
9	10.0	834.3	10.0	854	0.370	10.00

Table 5.1. Example of a form used during the calibration film irradiation.

5.2 Imparted dose calculation

The known $[K_{air}]_{air}$ values used to calibrate the film were calculated following the recommendations of the AAPM Report TG-61 on kilo-voltage dosimetry [28]. Accordingly, a three-step process was carried out to determine the quality of the beams, measure the output delivered by the machine X-ray tube for each beam quality, and finally choose the correct mAs setting ($[K_{air}]_{air}$ values to expose the calibration film strips). A scheme of the process is shown in ***Figure 5.2***.

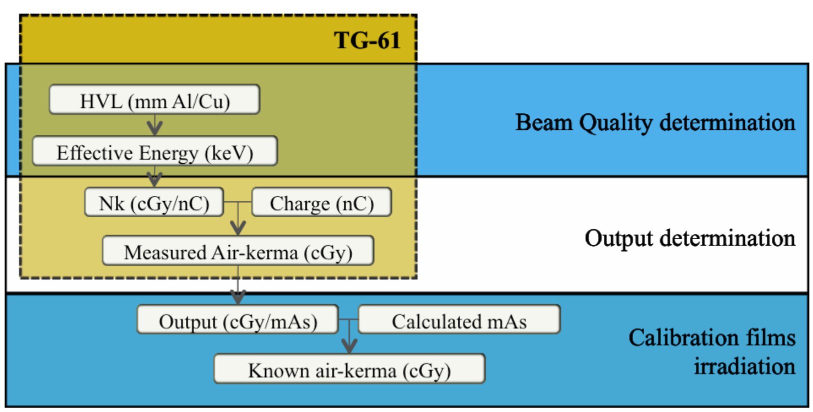

Figure 5.2. Scheme of the $[K_{air}]_{air}$ values determination process based on the recommendations by the AAPM Report No. 61 [28].

5.2.1 Beam quality determination

The Half Value Layer (*HVL)* of the beams delivered by the X-ray tube of the LightSpeed® CT Simulator was measured via linear attenuation coefficient. The *NE 2577c* ionization chamber was placed at the isocenter of the scanner and irradiated by the 80 kVp beam without filtration for 600 mAs with the x-ray tube in stationary mode (at 0^0). Three consecutive measurements of the collected charge were recorded, and a 0.5 mm thick aluminum sheet was then placed between the radiation source and the detector, as shown in ***Figure 5.3***. A lead diaphragm was used on top of the attenuator material to guarantee narrow beam geometry during *HVL* measurements, so that no scattered radiation could be detected by the ionization chamber.

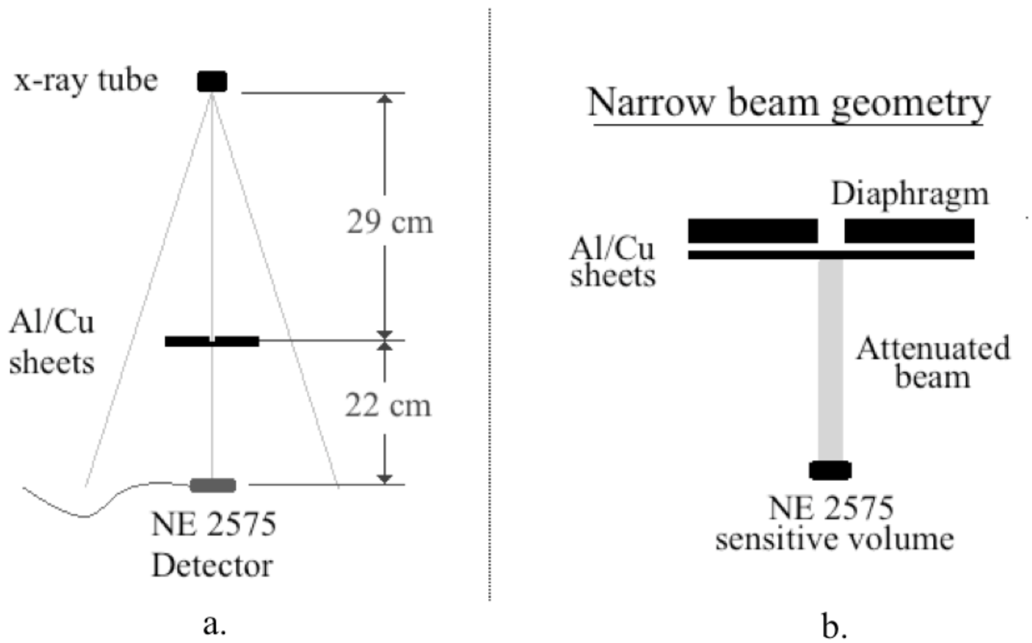

Figure 5.3. *HVL* measurements setup (a). Narrow beam geometry (b).

Collected charge was recorded without the modification of the irradiation parameters in order to quantify the attenuation of the beam though the aluminum sheet. New attenuator sheets were added until the charge collected by the detector dropped below a half of the non-attenuated beam measurement.

Acquired data $C_{mm\,Al/Cu}$ were normalized to the non-attenuated collected charge value C_0, and an exponential model $c(mm\,Al/Cu)$ was used to fit the measured data as a function of the attenuator thickness t:

$$c(t) = e^{\mu t}, \quad [5.1]$$

where μ represents the linear attenuation coefficient for the photon beam in aluminum (or copper) for a particular E_{eff}. The measurement was repeated in order to assess the linear attenuation coefficient for 12 beams (3 filters and 4 peak energies, as shown in ***Table 5.2***) delivered by the LightSpeed® CT Simulator. From ***Equation 5.1***, where $c(HVL) = 0.5$, *HVL* can be calculated as:

$$HVL(\mu) = -\frac{ln\ 0.5}{\mu}. \quad [5.2]$$

Table 5.2 provides a summary of the peak energy and filtration of the beams analyzed, as well as attenuator materials used for the *HVL* measurement.

The *National Institute of Standards and Technology* (*NIST*) database [41] on mass linear attenuation coefficients for aluminum and copper was used to interpolate the E_{eff} of the beams based on their measured coefficients.

This method was followed 2. ***Appendix 1*** outlines the raw and processed data from this measurement. Relative attenuation of the beam was plotted against attenuator material thickness, and ***Equation 5.2*** was used to fit the measurements with an exponential function shown in ***Figure 5.4***. The linear attenuation coefficient for that beam was found to be $\mu(80\ \text{kVp}, Air) = 0.172$.

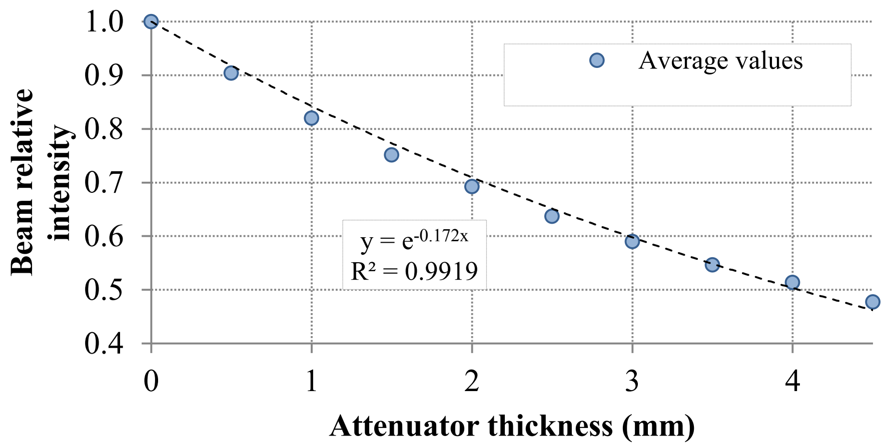

Figure 5.4. The attenuation of the 80 kVp beam aluminum attenuators. The dashed line indicates the exponential function fit to measured data.

Linear attenuation coefficients were converted to mass attenuation coefficients by normalizing to the attenuator material density (See ***Appendix 2*** to obtain raw data). This value was then used to interpolate effective energies from the *NIST* database [42]. ***Table 5.2*** summarizes the attenuation coefficients for all the beams and filters, as well as HVL values calculated using ***Equation 5.2***. ***Figure 5.5*** correlates calculated E_{eff} to delivered peak energy, discriminating additionally the filter used by the LightSpeed® CT Simulator to harden the beam.

Peak Energy (kVp)	Filter	Attenuator	Attenuation coefficient (cm^{-1})	R^2	HVL (mm)	Effective Energy (keV)
80	Air	Al	0.172	0.99	4.03	38.8
80	Head	Al	0.163	0.99	4.25	39.4
80	Body	Al	0.131	0.94	5.29	44.1
100	Air	Al	0.138	0.99	5.02	42.9
100	Head	Al	0.131	0.99	5.29	44.1
100	Body	Al	0.110	0.99	6.30	48.0
120	Air	Al	0.116	0.99	5.98	46.9
120	Head	Al	0.112	0.99	6.19	47.7
120	Body	Al	0.095	0.99	7.30	51.8
140	Air	Cu	1.817	0.97	0.38	50.1
140	Head	Cu	1.753	0.97	0.39	51.4
140	Body	Cu	1.227	0.97	0.49	56.3

Table 5.2. Results of the *HVL* measurements on the LightSpeed® CT Simulator.

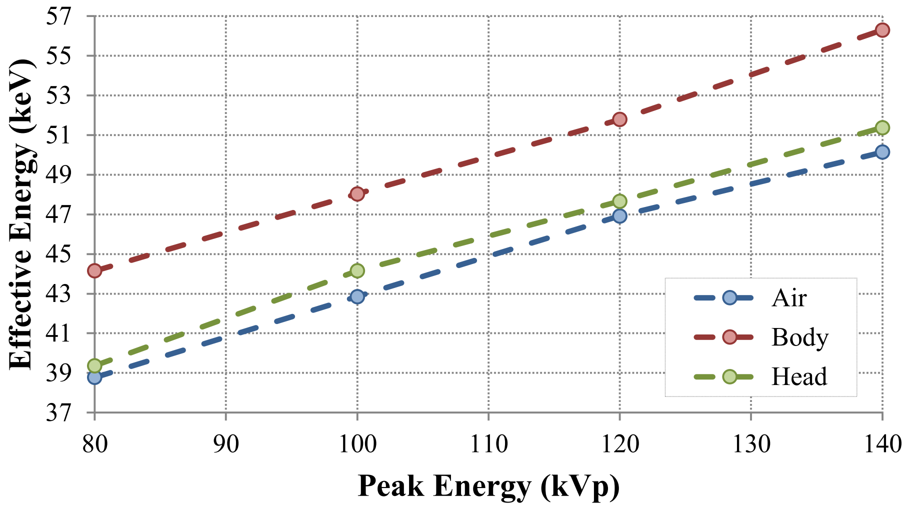

Figure 5.5. Effective photon beam energy measurements for the LightSpeed® CT Simulator.

5.2.2 Ionization chamber N_k interpolation

N_k values for the NE 2577c ionization chamber provided by the National Research Council of Canada [43] for the E_{eff} range from 14.24 keV to 114.56 keV were used, and they are shown in ***Figure 5.6***. Polynomial functions were created to fit the first three data points in ***Figure 4.4*** (14.24, 27.16, and $33.22\ keV$), and three intermediate additional points (33.22, 52.90, and $83.28\ keV$). Those models were used to interpolate the N_k values of the detector for the measured beam qualities. N_k functions for the NE 2577c ionization chamber were:

$$N_k^{fitted}(E_{eff}) = \begin{cases} 0.0081{E_{eff}}^2 - 0.5227E_{eff} + 21.015 & for\ E_{eff} < 33.22\ keV \\ 0.0003{E_{eff}}^2 - 0.0346E_{eff} + 13.426 & for\ E_{eff} \geq 33.22\ keV \end{cases}, \qquad [5.3]$$

where E_{eff} represents the effective beam energy. ***Figure 5.7a*** and ***Figure 5.7b*** demonstrate the polynomial functions for N_k interpolation. Finally, ***Equation 5.3*** was used to interpolate N_k values for the effective energies previously found, and the results are shown in ***Table 5.3***.

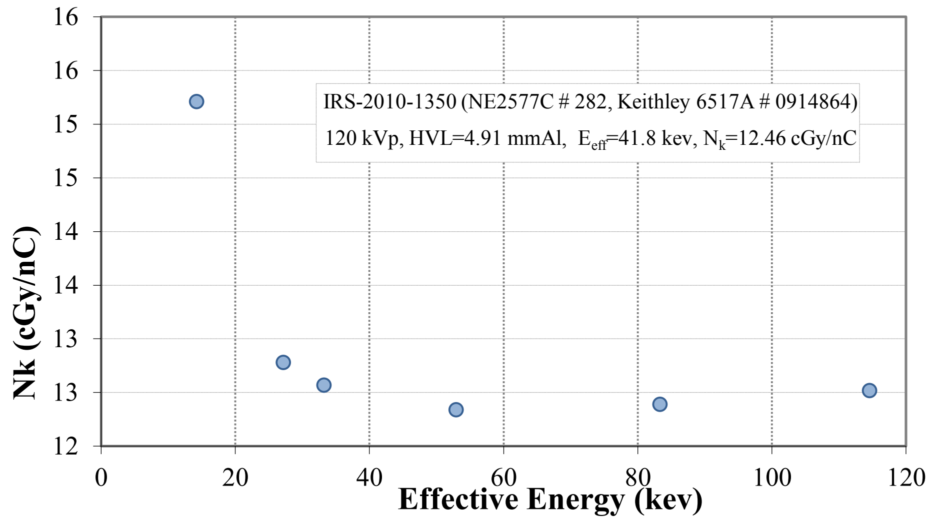

Figure 5.6. N_k values for the NE 2575 ionization chamber as a function of the effective photon energy obtained from the National Research Council [43].

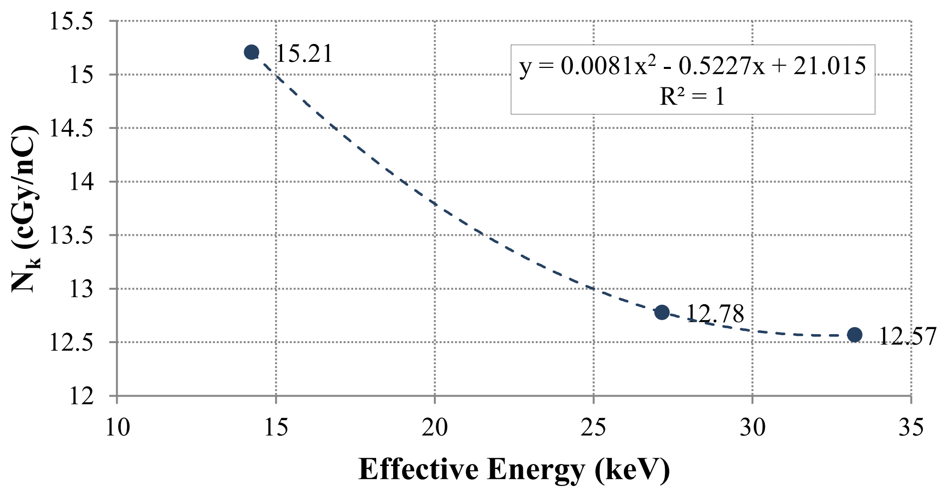

Figure 5.7a. The first three N_k values of ***Figure 5.6*** fitted with ***Equation 5.3*** – $E_{eff} <$ 33.2 keV.

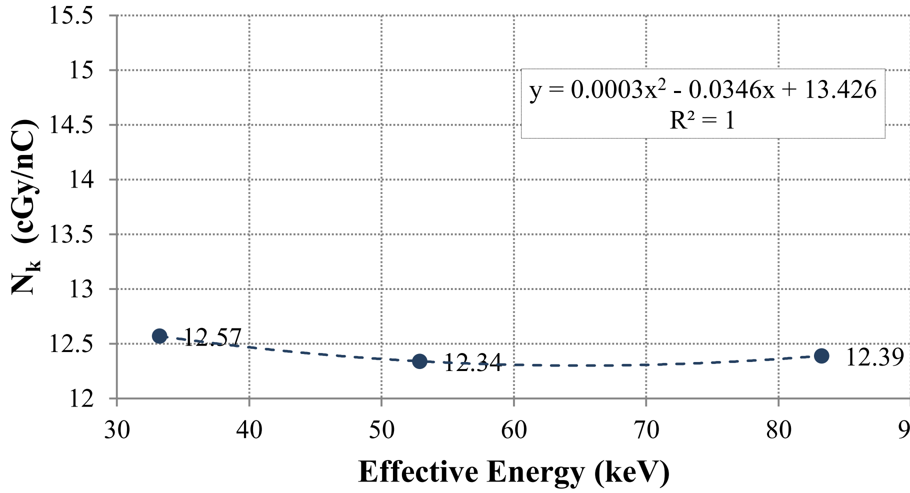

Figure 5.7b. The last three N_k values of ***Figure 5.6*** fitted with ***Equation 5.3*** – $E_{eff} > 33.2$ keV.

Date: 2013-09-07		Scanner GE CT Simulator		Energies (kVp) Filters		80-150 Air, Body, Head	
Source	Peak Energy (kVp)	Filter	*HVL*	Unit	μ/ρ cm2/g	E_{eff} keV	N_k cGy/nC
NRC Calibration IRS-2010-1350	50		0.27	mmAl	9.442	14.24	15.21
	80		1.82	mmAl	1.411	27.16	12.78
	120		3.03	mmAl	0.848	33.22	12.57
	180		0.35	mmCu	2.210	52.9	12.34
	220		1.10	mmCu	0.703	83.28	12.39
	250		2.22	mmCu	0.348	114.56	12.52
Beam qualities in this study	80	Air	4.03	mmAl	0.637	38.77	12.53
		Body	5.29	mmAl	0.485	44.15	12.48
		Head	4.25	mmAl	0.604	39.37	12.52
	100	Air	5.02	mmAl	0.511	42.85	12.49
		Body	6.30	mmAl	0.408	48.03	12.45
		Head	5.29	mmAl	0.485	44.15	12.48
	120	Air	5.98	mmAl	0.430	46.92	12.46
		Body	7.30	mmAl	0.352	51.78	12.43
		Head	6.19	mmAl	0.415	47.66	12.45
	140	Air	0.38	mmCu	2.050	55.52	12.42
		Body	0.49	mmCu	1.579	60.34	12.43
		Head	0.39	mmCu	1.961	56.39	12.42

Table 5.3. N_k values for the NE2577 ion chamber in the energies studied used to measure the output of the LightSpeed® Ct Simulator. The values shown in gray were interpolated from ***Equation 5.3.***

5.2.3 Radiation sources output determination

The AAPM Report TG-61 [28] was followed to measure $[K_{air}]_{air}$ at the reference point (12.0 cm above the isocenter) for the LightSpeed® CT Simulator. Accordingly, this value can be calculated as:

$$[K_{air}]_{air} = M^c \cdot N_k, \text{where} \quad [5.4]$$

$$M^C = M^{raw} \cdot P_{PT} \cdot P_{ion} \cdot P_{pol}\,, \quad [5.5]$$

$$P_{PT} = \frac{P_{ref}}{P} \cdot \frac{T}{T_{ref}}, \quad [5.6]$$

$$P_{ion} = \frac{1 - \left(\frac{V_H}{V_L}\right)^2}{\frac{M_{raw}^H}{M_{raw}^L} - \left(\frac{V_H}{V_L}\right)^2}, \text{and} \quad [5.7]$$

$$P_{pol} = \left|\frac{M_{raw}^+ - M_{raw}^-}{2M_{raw}}\right|, \quad [5.8]$$

with M^c being the charge collected by an ionization chamber corrected for pressure and temperature (P_{PT}), ion recombination (P_{ion}), and chamber polarity effect (P_{pol}), and N_k the detector calibration factor for a specific beam quality. ***Table 5.4*** summarizes the parameters included in ***Equations 5.4 - 5.8***. The setup of the M^{raw} measurements is shown in ***Figure 5.7.*** The measurement point corresponds to the location of calibration films during irradiation (12.0 cm above the isocenter). Measurements of $[K_{air}]_{air}$ were carried out for 600 mAs, and the imaging machine output O at the point of measurement was defined for a particular beam quality Q as:

$$O_Q(\text{cGy/mAs}) = \frac{[K_{air}]_{air}}{600\text{ mAs}}. \quad [5.9]$$

Parameter	Description
P_{ref}	Reference pressure (760 mm Hg)
T_{ref}	Reference temperature (295.2 K)
V_H, V_L	High and low electrometer voltage
M_{raw}^H, M_{raw}^L	Charge collected due to V_H and V_L
M_{raw}^+, M_{raw}^-	Charge collected when the electrometer bias is modified

Table 5.4. Parameters used for $[K_{air}]_{air}$ measurement, as suggested by the AAPM TG-61 [28].

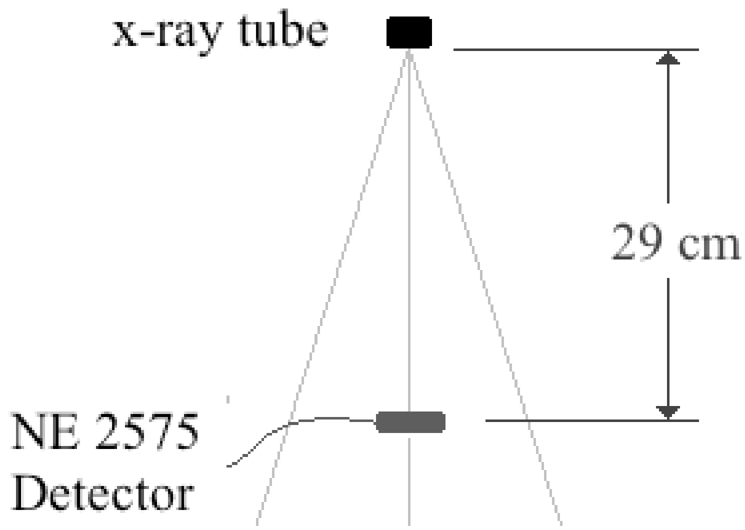

Figure 5.7. Setup for output measurements.

Figure 5.8 is a graph correlating the output (cGy/mAs) measured 12.0 cm above the isocenter of the LightSpeed® CT Simulator and the peak energy of the beam delivered by the x-ray tube of the machine. The 12 outputs measured for imaging beam qualities delivered by the CT simulator ($38.8\ keV \leq E_{eff} \leq 56.3\ keV$) and 6 additional outputs ($MU/200cGy$) measured on the Xstrahl 300 orthovoltage therapy unit were included to widen the E_{eff} range ($12.7\ keV \leq E_{eff} \leq 64.0\ keV$). ***Table 5.5*** details the peak energy delivered by the orthovoltage unit, the applicator dimensions, and the filter used to harden the beam. *HVL* values, E_{eff} and output were taken from the technical report of the machine [35]. An example of the format used to register raw and processed data from the output measurement process is provided in ***Appendix 3***.

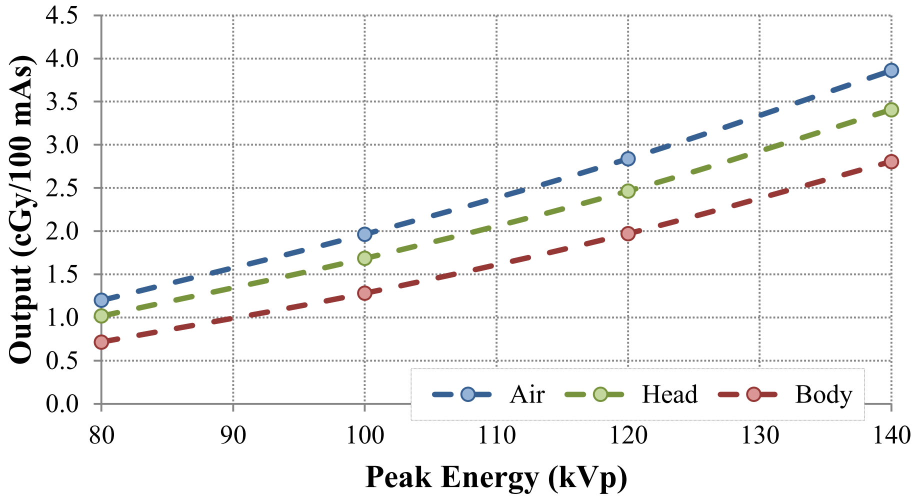

Figure 5.8. Output values for the beam qualities delivered on the LightSpeed® CT Simulator.

Peak energy (kVp)	*HVL* (mm) Al	Cu	Output (MU/200cGy)	Applicator diameter (cm)	Applicator length (cm)	Filter	Effective energy (keV)
50	0.16		1478	5	30	8	12.74
50	0.33		4514	10 cm X 10 cm*	20	1	15.5
70	1.38		1931	5	30	3	23.47
80	2.18		2038	5	30	2	29.5
120	4.19		1553	5	30	4	41.8
180		3.0	1559	6	31	6	64

Table5.5. Effective energy for the Xstrahl 300 orthovoltage therapy unit.

5.3 Fitting models assessment

The "*Levenberg-Marquardt*" iteration algorithm for non-linear fitting optimization was used to fit the experimental data presented in Section 6. Weighting factors w for each film response data point $\overline{\Delta R}_{net}$ were included in the iteration. A particular weighting factor $w(\overline{\Delta R}_{net})$ was defined as the inverse squared value of the standard deviation (*SD*) on the corresponding response of the film $\overline{\Delta R}_{net}$, normalized to the total inverse squared *SD* of the data series:

$$w(\overline{\Delta R}_{net}) = \frac{\frac{1}{SD^2(\overline{\Delta R}_{net})}}{\sum_{\overline{\Delta R}_{net}} \cdot \frac{1}{SD^2(\overline{\Delta R}_{net})}}. \quad [5.10]$$

Given a general fitting model $\Delta R_{net}([K_{air}]_{air})$ depending on a number n of scalar parameters $\alpha_1, \alpha_2, \cdots \alpha_n$ with Standard Error $SE(\alpha_i)$, the fitting uncertainty $\delta_{fit}([K_{air}]_{air})$ is defined as:

$$\delta_{fit} = \frac{\partial \Delta R_{net}}{\partial \alpha_1} \cdot SE(\alpha_1) + \frac{\partial \Delta R_{net}}{\partial \alpha_2} \cdot SE(\alpha_2) + \cdots + \frac{\partial \Delta R_{net}}{\partial \alpha_n} \cdot SE(\alpha_n). \quad [5.11]$$

While the experimental uncertainty $\delta_{exp}([K_{air}]_{air})$ due to the inhomogeneity in the exposed *ROI* is calculated as:

$$\delta_{exp} = \frac{d\Delta R_{net}}{dK} \cdot SD(\overline{\Delta R}_{net}). \quad [5.12]$$

Both uncertainty components are added in quadrature to obtain the total uncertainty $\delta_T([K_{air}]_{air})$ in the calibration curve:

$$\delta_T([K_{air}]_{air}) = \sqrt{{\delta_{fit}}^2 + {\delta_{exp}}^2}. \quad [5.13]$$

Three fitting functions $\Delta R_{net}((K_{air})_{air}, Q)$ were tested, and the fitting uncertainties associated with the corresponding calibration curves were compared in order to select the model that offered the lowest total uncertainty. The bi-parametric models $f_i(\alpha, \beta)$ used to fit measured average net reflectance change ΔR_{net} and delivered air-kerma in air $[K_{air}]_{air}$ were:

$$f_1(\alpha, \beta) \to \Delta R_{net} = \frac{\alpha [K_{air}]_{air}}{1 + \beta K_{air}}, \quad [5.14]$$

$$f_2(\alpha, \beta) \to \Delta R_{net} = \alpha([K_{air}]_{air})^{\beta},$$

$$f_3(\alpha, \beta) \to \Delta R_{net} = \alpha [K_{air}]_{air} + \beta([K_{air}]_{air})^{2.5},$$

as suggested by Tomic *et al.* in 2010 [27]. Standard error (SE) in each parameter α and β of models f_i was recorded as a function of the E_{eff} used to irradiate the calibration films, as shown in ***Figure 5.9*** for f_1. Absolute standard error in α was constant over the $12.7 - 64.0$ keV E_{eff} range ($\overline{SE}_\alpha = 0.140 \pm 0.194$ cGy^{-1}), and just one point was seen out of range at very low energy ($SE_\alpha = 0.925\ cGy^{-1}$ at $12.7\ keV$). This is beyond the energy range for the film recommended by the manufacturer (20 keV) [32]. Absolute error in β was even more stable ($\overline{SE}_\beta = 0.018 \pm 0.024$ cGy^{-1}) with a slightly higher value at the lowest energy ($SE_\beta = 0.116$ cGy^{-1} at 12.7 keV). In relative terms, average percent errors of $100\,\% \cdot SE_\alpha/\alpha = 1.6\,\%$ and $100\,\% \cdot SE_\beta/\beta = 1.0\,\%$ were obtained for the model number 1, as shown in ***Figure 5.10.***

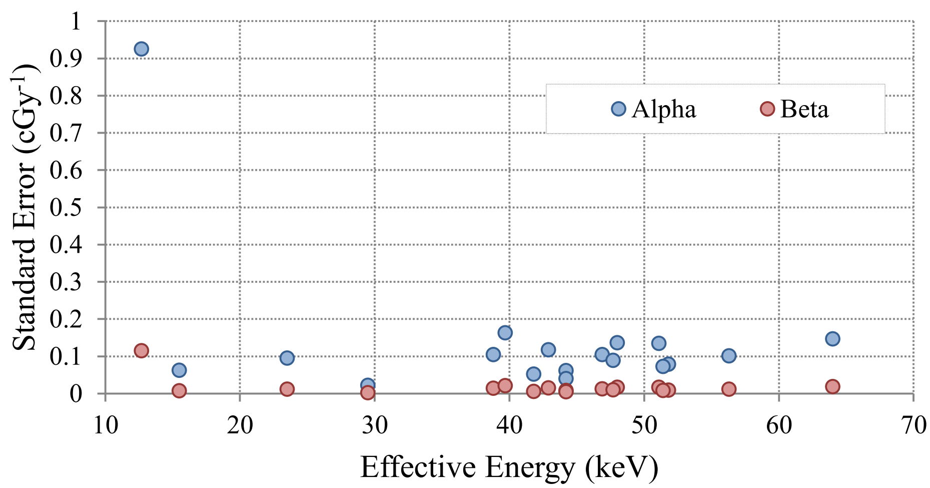

Figure 5.9. Absolute error in the fitting parameters for f_1.

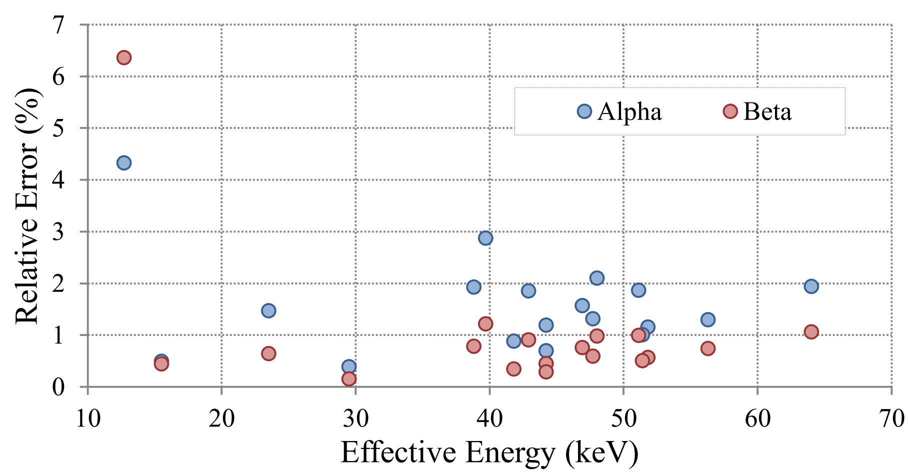

Figure 5.10. Relative error in the fitting parameters for f_1.

Average SE for each model f_i and parameter α and β are shown in ***Table 5.6***. Results indicate that model f_1 provides on average less uncertainty to the total dose measurement uncertainty over the whole E_{eff} range used during regular imaging protocols by CT scans and OBI devices ($38.8 - 56.4\ keV$). Based on this important finding, the function f_1 was chosen as a model to fit ΔR_{Net} as a function of $[K_{air}]_{air}$.

Model	Coefficient	Effective Energy Range	
		$12.7\ -\ 64.0\ keV$	$38.8 - 56.4\ keV$
f_1	Alpha	1.6	1.6
	Beta	1.0	0.7
f_2	Alpha	1.9	1.9
	Beta	1.2	0.9
f_3	Alpha	1.8	1.9
	Beta	1.0	0.9

Table 5.6. Relative Uncertainty (%) of to the fitting coefficients.

Figure 5.11 is a plot of values obtained for α and β when the fitting model f_1 was used. The response of the film to ionizing radiation can be well characterized in the E_{eff} range from 38.8 keV to 56.3 keV (beam qualities delivered by the GE CT simulator) due to the small variation of the fitting parameters in this energy range. Indeed, while beta is almost constant for any E_{eff} within that range ($\bar{\beta} = -1.74\ \pm 0.05$ cGy^{-1}), alpha increases linearly ($\bar{\alpha} = 6.46 \pm 0.77$ cGy^{-1}) with a relatively small slope ($m_\alpha = 0.14$ cGy$^{-1} \cdot$ keV^{-1}), as shown in ***Figure 5.12***. On the other hand, outside of the imaging effective range, the response of the film is strongly dependent on the beam quality. At very low effective energies alpha decreases drastically from 21.36 to 5.69 cGy^{-1}, and at 40 keV its value increases constantly.

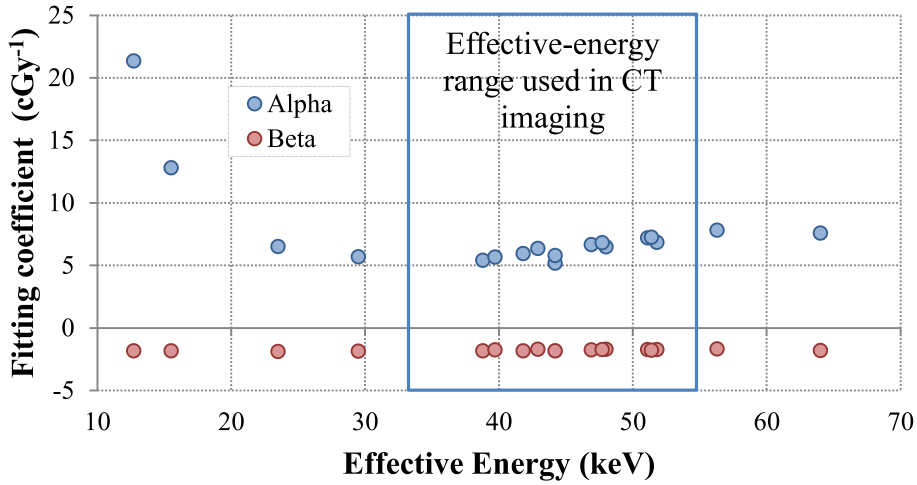

Figure 5.11 Fitting parameters as a function of effective energy.

If the small variation in the value of the parameter β across the whole E_{eff} range is considered negligible ($\beta \rightarrow \bar{\beta}$), the fitting model f_1 takes a simpler form, depending just on parameter α:

$$\Delta R_{net} = \frac{\alpha \cdot [K_{air}]_{air}}{1 - 1.74 \cdot [K_{air}]_{air}}. \qquad [5.15]$$

Figure 5.12 is a plot of the fitting parameters value as a function of the beam E_{eff} in the range $38.8\ keV$ – $56.3\ keV$. It includes also a linear approximation for parameters α and β, which can be used to express f_1 in terms of E_{eff}:

$$\Delta R_{net} = \frac{\left(0.138\ E_{eff} - 0.022\right) \cdot [K_{air}]_{air}}{1 + \left(0.005\ E_{eff} - 1.997\right) \cdot [K_{air}]_{air}}. \qquad [5.16]$$

Equation 5.6 describes the change in reflectance ΔR_{net} of the Gafchromic® XR-QA2 model film to ionizing radiation of effective energy 38.8 keV $\leq E_{eff} \leq$ 56.3 keV in the air-kerma in air range 0 mGy $\leq [K_{air}]_{air} \leq$ 100 mGy.

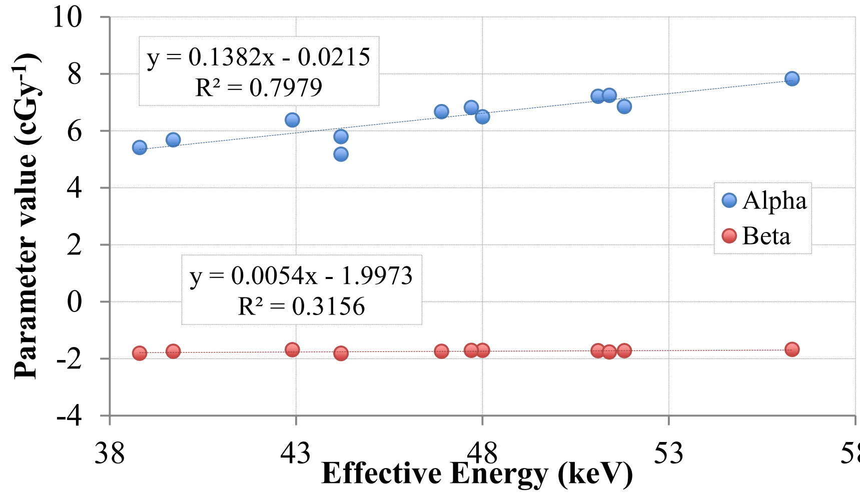

Figure 5.12. Energy dependence of the fitting parameters 38.8 keV – 56.3 keV.

5.4 Film analysis Matlab user code

As a clinical tool for CTDI measurements, the code relies on the user inputs with two sets of images and information about the image and the irradiation protocol. Parameters as image resolution (dpi), area of the *ROI* defined inside of the calibration film (pixel^2), beam collimation (mm), deemed $[K_{air}]_{air}$ values used to irradiate the calibration films (cGy), air to water mass energy absorption coefficient ratios, pitch, and integration length of the dose profiles (mm) are required. Given a set of films placed in the PMMA phantom for CTDI measurements, and a particular imaging protocol used to scan the phantom, the Matlab in house-written code for film images analysis was designed to work in sequence on two related processes. The first one is creating the calibration curve for the particular beam quality, and the second step is calculation of the CTDI from measurement films.

The input for the calibration curve code is the calibration films TIFF images and the related image information, while the output is the fitting curve for the response of the film and an appendix with uncertainty analysis. The set of images consists of one image of the calibration films prior to the irradiation and other after being exposed. The code identifies and confirms the number of films on each image, isolates and rotates them correcting for any undesirable misalignment. The average

PV and its standard deviation inside of a 100 pixel^2 region of interest (ROI) are recorded and used along with the irradiation parameters as experimental data to run an iteration process that optimizes a bi-parametric fitting model (***Equations 5.3***).

The second section of the code is fed with the TIFF images of a set of films used to measure the CTDI value for a particular imaging protocol in conjunction with the parameters of irradiation. Finally, the code provides dose profiles of the films and dosimetric parameters such as $CTDI_{100}$, $CTDI_{vol}$ and dose peaks.

Figure 5.13 is an image of a set of calibration films before and after irradiation used as input for the film analysis code. These films were exposed to a 80 kVp photon beam delivered by the LightSpeed® CT Simulator without filtration (38.8 keV). ***Figure 5.14*** shows the corresponding calibration curve. The code's output consists of a plot of the measured and fitted net reflectance change as a function of delivered $[K_{air}]_{air}$(presented in ***Table 5.1***), fitting parameters α and β, and a plot of experimental, fitting and total uncertainty associated with the calibration curve.

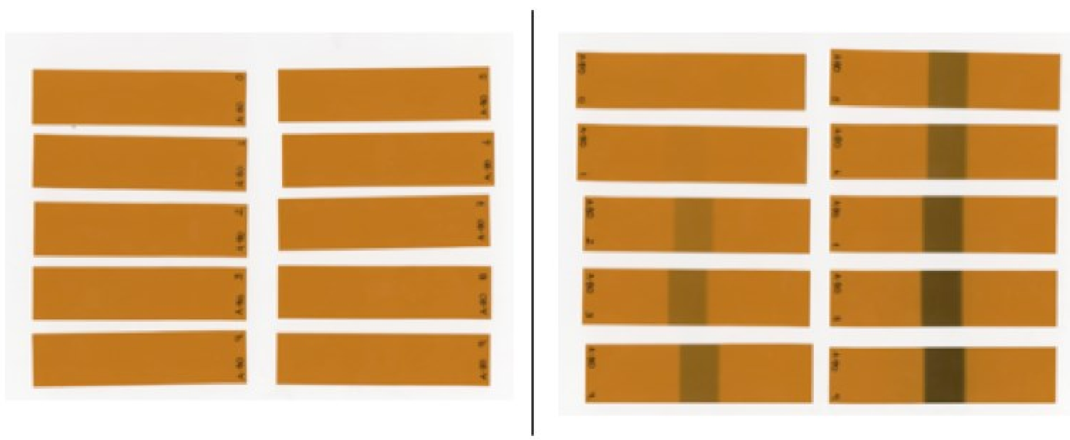

a. b.

Figure 5.13. Images of calibration films before (a) and after (b) irradiation.

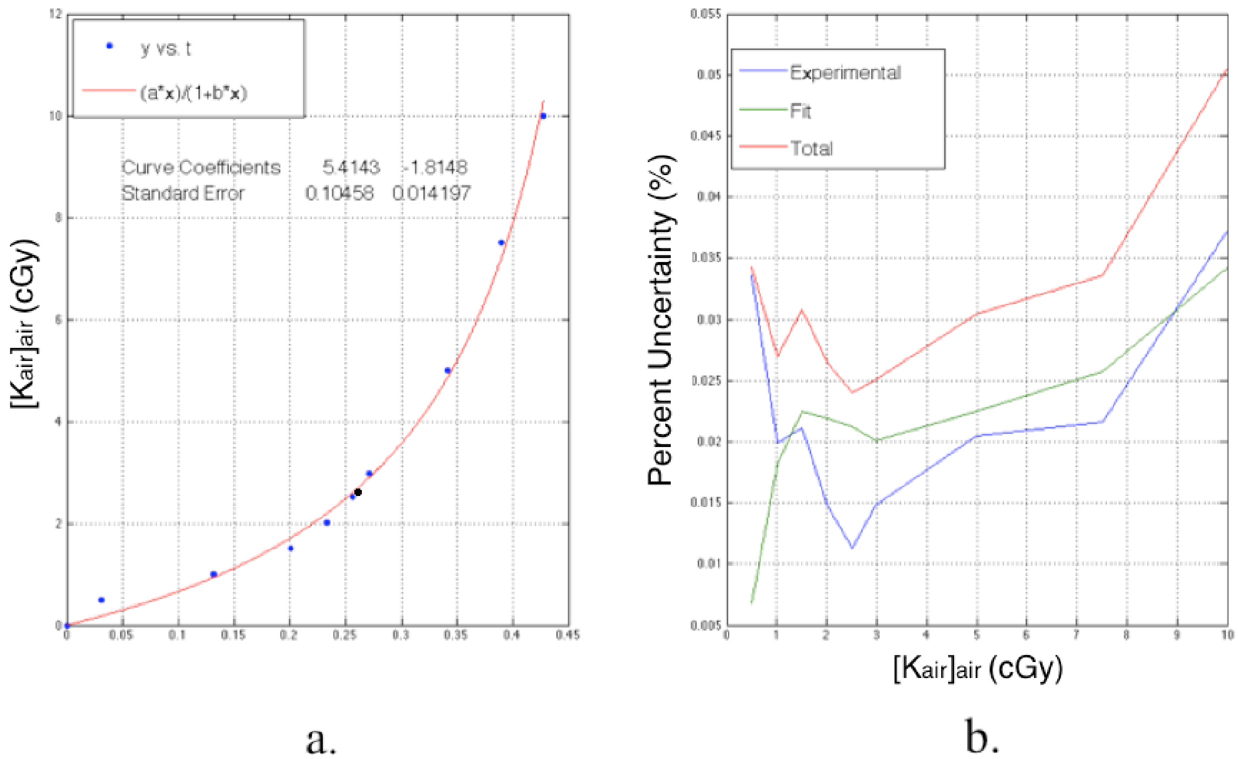

Figure 5.14. Calibration curve (a) and uncertainties associated to the calibration curve (b) for an 80 kVp beam without filtration delivered by the LightSpeed® CT Simulator. Experimental, fitting and total uncertainties were calculated from ***Equation 5.10*** to ***Equation 5.12.***

Once the calibration parameters have been established, the code proceeds to use the film images of the films to produce film response maps ΔR_{net} (***Equation 3.1 – 3.3***). ***Figure 5.15*** shows a set of films irradiated in a PMMA phantom for CTDI measurements. Subsequently, based on the fitting parameters found during the first step, $[K_{air}]_{air}$ maps (***Equation 3.5***), and dose to water maps $[D^{w}]_{air}$ (***Equation 3.6***) are obtained. Finally, dose maps are used to produce dose profiles $\boldsymbol{Dp_i}$ (***Equation 3.10***), whose analysis result into CTDI values (***Equation 3.11 – 3.13***), and dosimetric parameters such as maximum dose across the dose profile D_{max}, and point of maximum dose $z(D_{max})$. The output of the code includes a log chart with CTDI values and other dosimetric information, as well as graphs of the dose profiles along the *z*-axis, such as the profiles shown in ***Figure 5.16***.

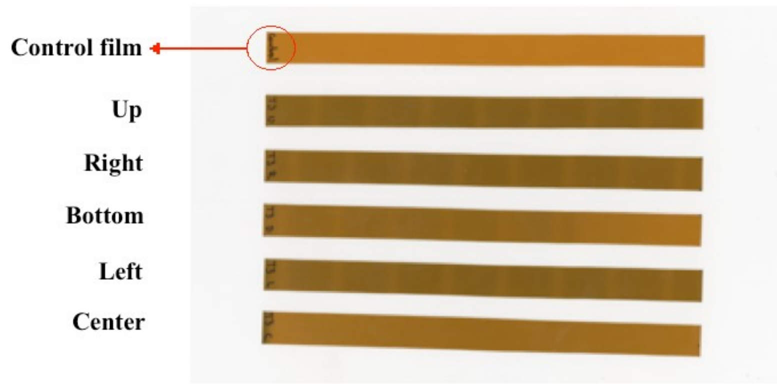

Figure 5.15. Set of films scanned by a helical imaging protocol on a CT device, and the place in the phantom where they were placed. On the top, the non-irradiated control film is shown.

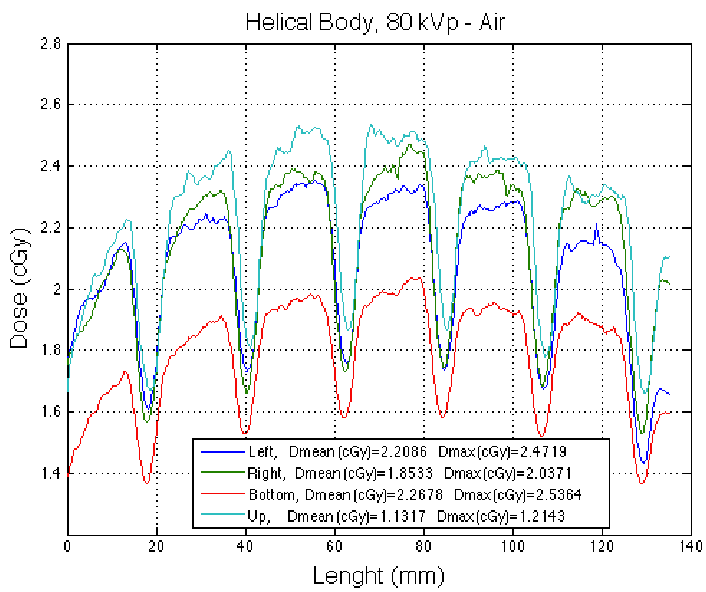

Figure 5.16. Dose profiles corresponding to the peripheral films shown in ***Figure 5.15*** (the dose profile acquired by the film placed in the center of the phantom has been removed from the plot). Contiguous dose peaks can be identified from the dose profiles (Full Width at Half Maximum of 20 mm due to the beam collimation, $N \cdot T = 20$ mm).

6. Film Orientation Dependence

6.1 Static x-ray tube film irradiation

During the film irradiation by a moving radiation source, the incidence angle $\theta_{incidence}$ between the beam central axis and the vector normal to the active layer film varies over time, ranging from 0° to $360°$ for a full rotation scan in a CT scanner (less for a Cone Beam-type scan), as shown in ***Figure 6.1***. In any case, the response of the film ΔR_{net} for the same beam quality Q and $[K_{air}]_{air}$ may vary depending on $\theta_{incidence}$. The aim of this test was to assess the average uncertainty in the response of the film when it is exposed to a full rotation of the radiation source.

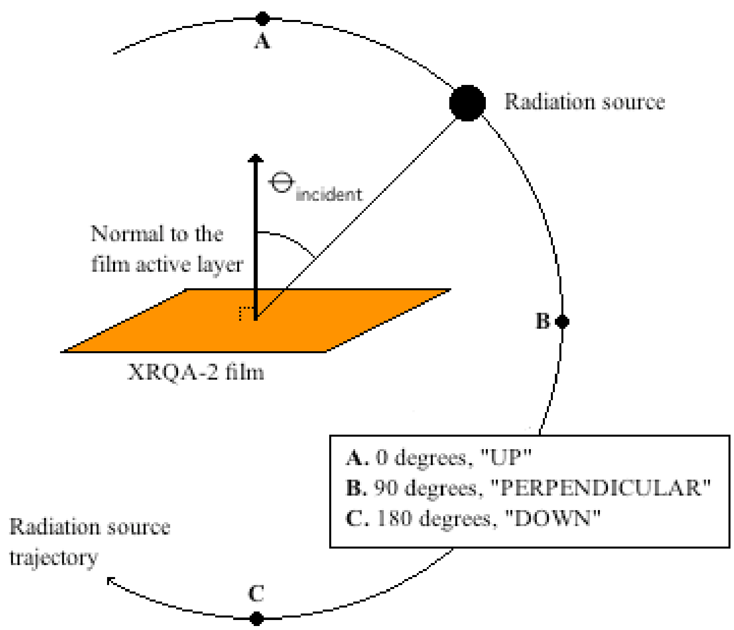

Figure 6.1. Scheme of the incidence angle $\theta_{incidence}$ defined by the normal to the active layer surface vector and the beam central axis. At point **A** of the radiation source trajectory, the film active layer and the yellow polyester layer are facing the radiation source, while at point **C** the white polyester layer is facing the radiation source. At point B the active layer is parallel to the central axis of the beam.

The difference in the film response when it is irradiated from points **A** and **B** of ***Figure 6.1*** was assessed. The LightSpeed® CT Simulator with the x-ray tube in static mode with $E_{eff} =$ 38.8 keV was used to expose films in air, on the surface of the PMMA phantom, and in the phantom at 5 cm depth. One set of films was exposed in the "*UP*" position, and another set was subsequently exposed in the "*DOWN*" position, as shown in ***Figure 6.2.*** In order to test the reproducibility of the measurement the procedure was repeated three times.

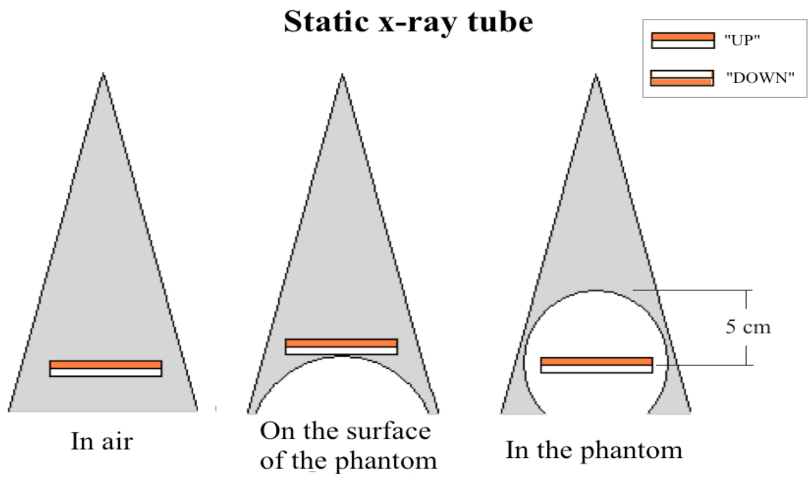

Figure 6.2. Setup of the static x-ray tube test to assess the Gafchromic® XR-QA2 film angular dependence. Sets of films were irradiated free in air, on the surface and in the PMMA phantom to assess the effect of scattering radiation in the response of the film when its active layer is facing the radiation source.

The average net reflectance change was calculated inside a 20×20 pixel^2 ROI in the center of each film strip. The average value in the response of the *"UP"* films was compared to the corresponding *"DOWN"* value under each setup condition. The process was repeated for $E_{eff} = 47.7$ and $E_{eff} = 56.3$ keV to evaluate the orientation dependence over a relatively broad energy range. The irradiation parameters are outlined in ***Table 6.1.***

Peak energy (kVp)	Filter	HVL (mm)	Effective energy (keV)	mAs	Beam collimation (mm)
80	Air	4.03 Al	38.8	500	15
120	Head	6.02 Al	47.7	500	15
140	Body	0.49 Cu	56.3	500	15

Table 6.1. Static x-ray tube irradiation parameters.

The uncertainty in the response of the film due to the measurement procedure was compared to the difference in the average response of the *"DOWN"* and *"UP"* films. Profiles of the beams across the *x*-axis were acquired to compare the effect of the active layer orientation on the response of the film. These profiles are averaged to produce the dose profiles used to calculate CTDI values, as stated in **Equation 3.11**

Figure 6.3 shows the difference in ΔR_{Net} of the film when irradiated in the "UP" or "DOWN" orientation. In the first case, the beam is partially absorbed and scattered by the transparent layer of the film before interacting with the active layer, and then it is backscattered by the opaque layer. In the second case, any change in the active layer is the result of its interaction with the partially absorbed and scattered beam coming from the opaque layer first, and then being backscattered from the transparent layer. Films were exposed to the same mAs under the same setup, so any difference in the net reflectance's change should be associated to the orientation of the active layer. This procedure was carried out for E_{eff} = 38.8 keV, E_{eff} = 44.7 keV, and E_{eff} = 56.3 keV.

Error bars in the plot show 1σ uncertainty in the film response of the film (ΔR_{net}) for the same setup after carrying out multiple irradiations. For the softest evaluated beam (38.8 keV), the absolute uncertainties in the film response were $\sigma_{UP} = 3.24 \times 10^{-3}$, and $\sigma_{DOWN} = 8.53 \times 10^{-3}$, while the absolute difference between the film responses was $[\Delta R_{net}]_{UP-DOWN} = 2.73 \times 10^{-3}$. According to these results, any uncertainty in the response of the film due to the orientation of the active layer with respect to the radiation source can be neglected, as the difference in the responses is smaller than the uncertainty in the net reflectance change of the film for each orientation separately. In the middle of our tested energy range (47.7 keV), $\sigma_{UP} = 4.04 \times 10^{-3}$, $\sigma_{DOWN} = 3.59 \times 10^{-3}$, and $[\Delta R_{net}]_{UP-DOWN} = 8.61 \times 10^{-3}$. At higher beam energy (56.3 keV), $\sigma_{UP} = 4.85 \times 10^{-3}$, $\sigma_{DOWN} = 4.62 \times 10^{-3}$, and $[\Delta R_{net}]_{UP-DOWN} = 2.44 \times 10^{-3}$. $[\Delta R_{net}]_{UP-DOWN}$ values in the studied E_{eff} range were consistently lower than $\delta_T([K_{air}]_{air})$ for $5\ \mathrm{mGy} < [K_{air}]_{air}, 100\ \mathrm{mGy}$, which suppose a weak dependence of the Gafchromic® XR-QA2 film response on the orientation of the active layer ("*UP*" or "*DOWN*") respect to a static radiation source for in-air irradiations.

Figure 6.4 shows the results for the static tube irradiation when the films were placed on the surface of the PMMA phantom. The results indicate that $[\Delta R_{net}]_{UP-DOWN}$ is smaller than $\delta_T([K_{air}]_{air})$ for 5 mGy < $[K_{air}]_{air}$, 100 mGy and for all the studied energies. No significant differences between $\Delta R_{net}|_{UP}$ and $\Delta R_{net}|_{DOWN}$ were observed due principally to the effect of radiation backscattered from the phantom surface interacting with the film active layer in both orientations. ***Figure 6.5*** shows the results of the static x-ray tube tests for film orientation dependence when the films were placed inside of the PMMA phantom. Similarly to the former case, small differences were observed between the film responses under different orientations. Scattered radiation coming from all around the film pieces interact with the active layer, reducing the influence of the film orientation on the reflectance response when scanned into the phantom.

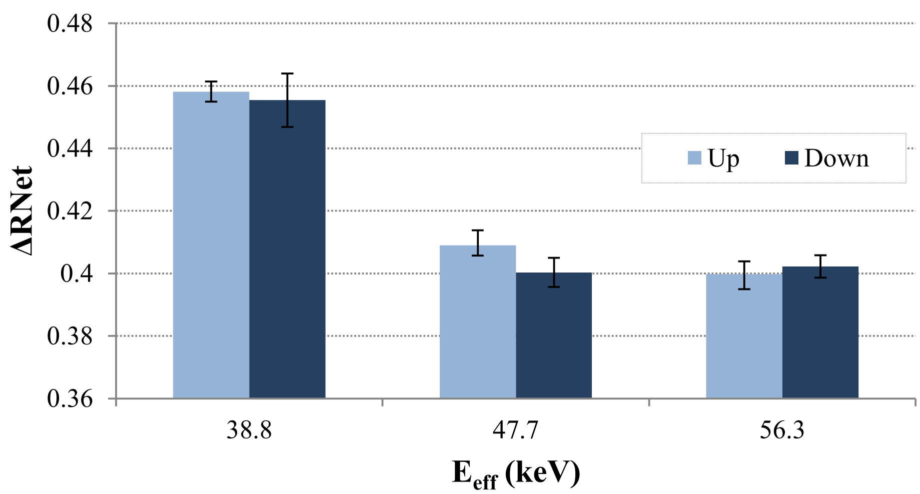

Figure 6.3. Film orientation response for a fixed X-ray tube. Three consecutive measurements were made free in air, and the error bars correspond to 1σ uncertainty in ΔR_{Net}.

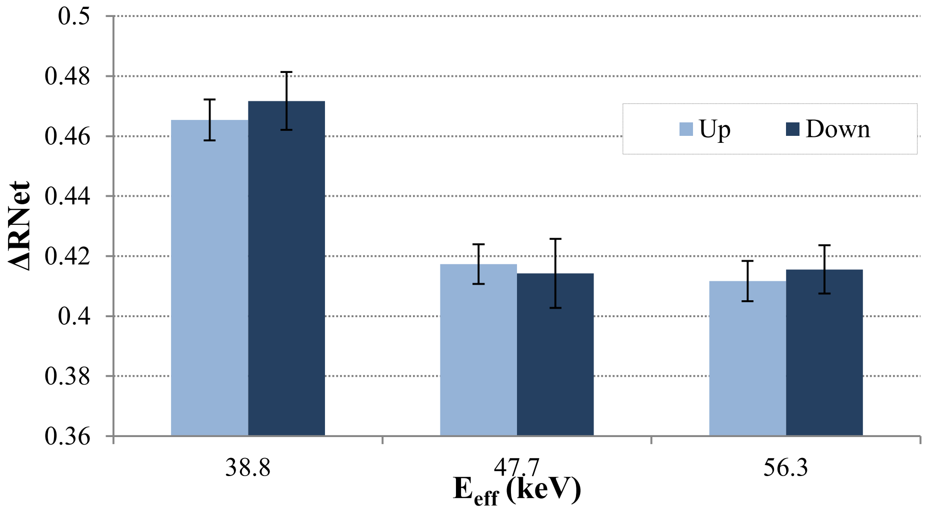

Figure 6.4. Film orientation response for a fixed X-ray tube. Three consecutive measurements were made on the surface of the phantom, and the error bars correspond to 1σ uncertainty in ΔR_{Net}.

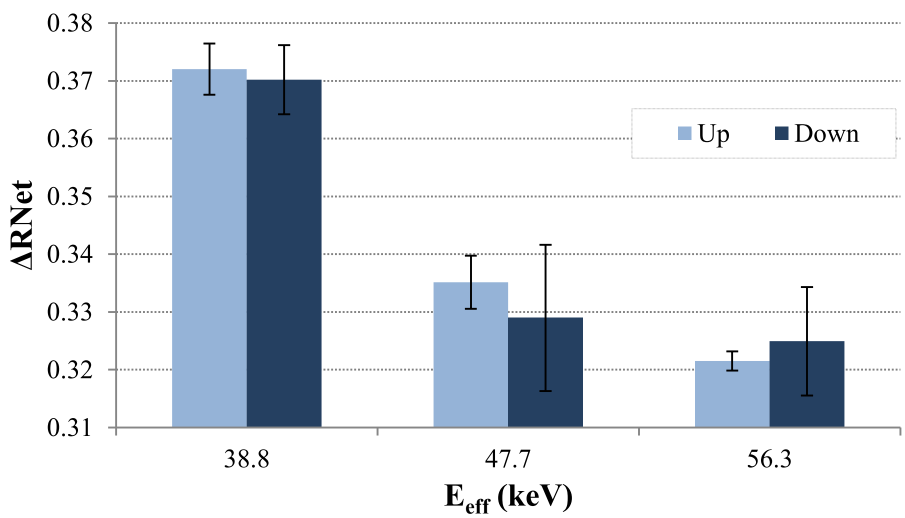

Figure 6.5. Film orientation response for a fixed X-ray tube. Three consecutive measurements were made in the phantom, and the error bars correspond to 1σ uncertainty in ΔR_{Net}.

Uncertainties in ΔR_{net} for each orientation (σ_{UP}, σ_{DOWN}), setup and E_{eff} are summarized in ***Table 6.2***. It also includes the absolute difference in the net reflectance change $[\Delta R_{net}]_{UP-DOWN}$. Finally, the setup and energy for which the orientation uncertainty can be neglected are highlighted. In these cases, the uncertainty associated to the orientation of the film is smaller than the film response uncertainties themselves, σ_{UP} and σ_{DOWN}.

	Setup								
	Air			Surface			Phantom		
Effective Energy (keV)	33.8	47.7	56.3	33.8	47.7	56.3	33.8	47.7	56.3
$\sigma_{UP}(\times 10^{-3})$	3.24	4.04	4.85	6.78	6.74	6.59	4.43	1.66	4.62
$\sigma_{DOWN}(\times 10^{-3})$	8.53	3.59	4.62	9.64	8.03	11.50	5.96	9.40	12.65
$[\Delta R_{net}]_{UP-DOWN}(\times 10^{-3})$	2.73	8.61	-2.44	-6.33	3.12	-3.42	1.83	6.17	-3.42

Table 6.2. Uncertainty in the film response due to its orientation (σ_{UP} and σ_{DOWN}). - Static X-Ray tube Setup. Highlighted fields indicate cases where $[\Delta R_{net}]_{UP-DOWN} < \sigma_{UP}$ and $[\Delta R_{net}]_{UP-DOWN} < \sigma_{DOWN}$.

"UP to DOWN" response film ratios $\frac{[\Delta R_{net}]_{UP}}{[\Delta R_{net}]_{DOWN}}$ are plotted in ***Figure 6.6***. The closer to 1 the ratio is, the smaller the orientation film dependence is. Error bars in ***Figure 6.6*** correspond to the propagated uncertainty in "UP to DOWN" rations $\sigma\left(\frac{[\Delta R_{net}]_{UP}}{[\Delta R_{net}]_{DOWN}}\right)$ and is plotted as a function of E_{eff} in ***Figure 6.7***. The maximum difference in the film response was seen, as expected, in air at medium energies (~2.2 %), while the absolute average difference for the measurements on the surface and inside the phantom where minimal and similar in value (~1.0 % on the surface, and ~1.3 % inside the phantom). At energies near the middle of the range of interest (47.7 keV), the response of the film is consistently greater when its active layer is facing the static x-ray tube ("Up"). This is $\frac{[\Delta R_{net}]_{UP}}{[\Delta R_{net}]_{DOWN}} > 1$ for every setup, but the opposite trend is observed at high energies ($56.3\ keV$), where $\frac{[\Delta R_{net}]_{UP}}{[\Delta R_{net}]_{DOWN}} < 1$. At low energy (38.8 keV) no consistent trend in $\frac{[\Delta R_{net}]_{UP}}{[\Delta R_{net}]_{DOWN}}$ values was noted.

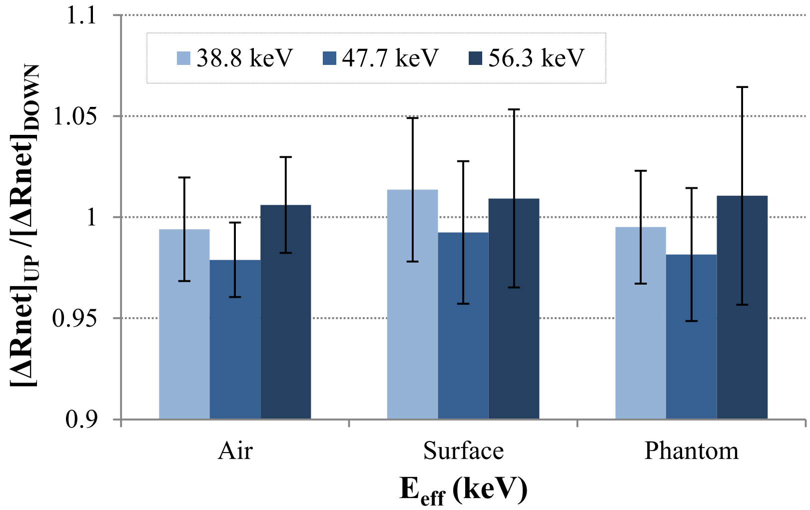

Figure 6.6. Film orientation response to a fixed X-ray tube. Measurements free in air, on the surface of a PMMA phantom, and in the phantom at 5 cm depth are shown.

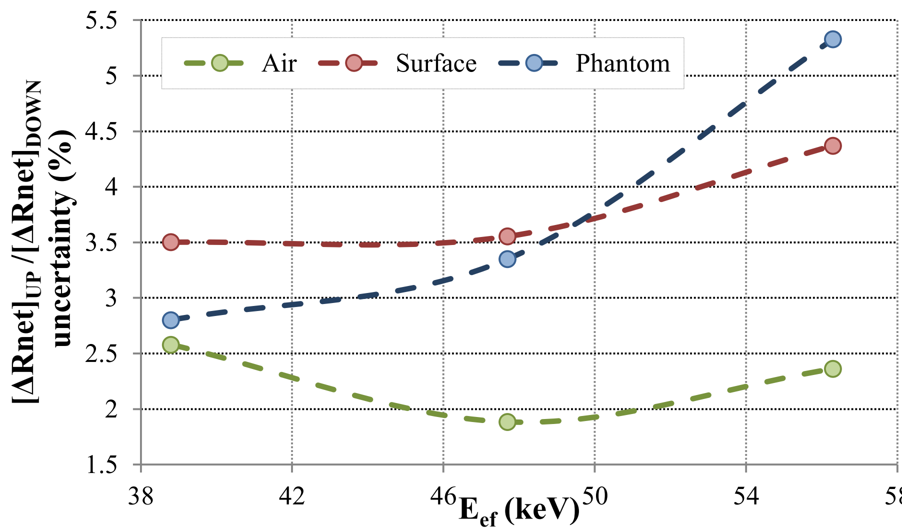

Figure 6.7. Percent uncertainty in $\frac{[\Delta R_{net}]_{UP}}{[\Delta R_{net}]_{DOWN}}$ as a function of E_{eff}.

Net reflectance change profiles along the x-axis (where the collimation of the beam is noticeable) were created from the irradiated films at low energy (33.8 keV) to assess differences in the film response. ***Figure 6.8*** shows the response of the film when scanned under diverse setups. In general, for each profile it is possible to identify two zones, a central peak due to the direct interaction of the central beam with the active layer of the film, and lateral tails due to the effect of scattered radiation. The central zone width correlates to the beam collimation, and its height is proportional to the absorbed dose.

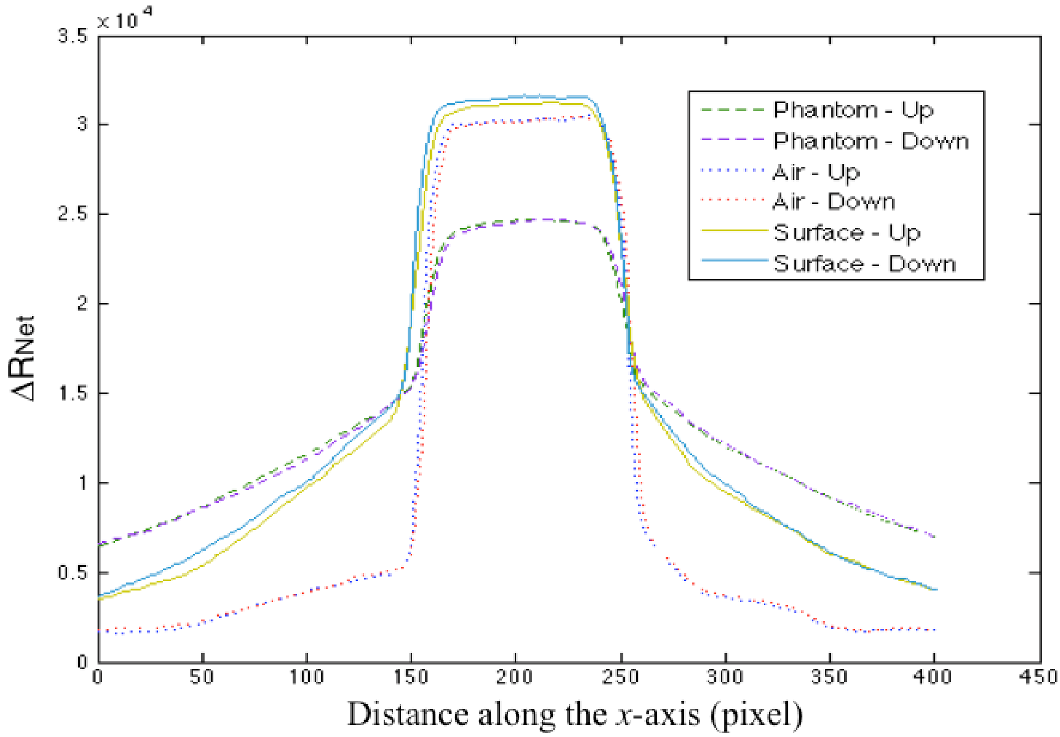

Figure 6.8. ΔR_{net} profiles along the *x*-axis for a 38.8 keV beam delivered by the LightSpeed® CT Simulator.

The central exposed zone has lowest ΔR_{net} values measured in phantom is lower, *i.e.* absorbed dose. In accordance with the behavior of low energy photons with matter, the maximum dose is deposited on the surface of the phantom, and the energy deposited by the charged particles decreases with the depth as radiation is attenuated by the phantom before interacting with the film (see **Appendix 4**, Percentage Depth Dose for kilovoltage photon beams). Additionally, in phantom profiles exhibit more pronounced tails due to the scattered radiation interacting with the film outside of the collimated central beam. This increases the dose contribution to the total profile along the tails. The opposite case is seen when the profile is acquired free in air; in such a case the central peak is as high as on the surface of the phantom, as the beam attenuation in air is negligible, and the tails are flatter and shorter due to the limited amount of scattered radiation coming from the surrounding air. Finally, the profile corresponding to the film placed on the surface of the phantom presents a high central peak, as the central beam has been scattered only by air before interacting with the active layer, but high tails are also present due to backscattered radiation coming from the surface of the phantom.

No significant differences were observed between the profile responses when the film was placed in the "UP" or "DOWN" orientation. This applied for the three analyzed setups, but it was especially interesting for measurements inside the phantom where such a difference was consistent with the results shown in ***Figure 6.6*** (average difference along the profiles lower than 1.5 %). CTDI measurements with Gafchromic® XR-QA2 films, as proposed here, are based on the integration of dose profiles as described in ***Section 3.1***, and shown in ***Figure 6.8*** as "Phantom – UP" curve.

6.2 Rotating x-ray tube film irradiation

The net effect of the film orientation on its response to ionizing radiation was assessed. The GE CT simulator was used to scan the PMMA phantom for CTDI measurements after a full rotation of a well-defined imaging protocol. Five filmstrips sandwiched in PMMA rods were placed in the holes of the phantom in such a way that the active layer in the periphery holes was always facing the radiation source when the x-ray tube passed diametrically over the corresponding phantom hole. This configuration corresponds to 0° in the scheme of ***Figure 6.9***. The procedure was repeated three times to assess the reproducibility of the method. Subsequently, the phantom was scanned by the same imaging protocol with the white layer of the films of the phantom periphery facing the x-ray tube. This is the 180° setup shown in ***Figure 6.9***. Finally, the films were placed at 90° into the periphery holes of the phantom, as indicated in the same image.

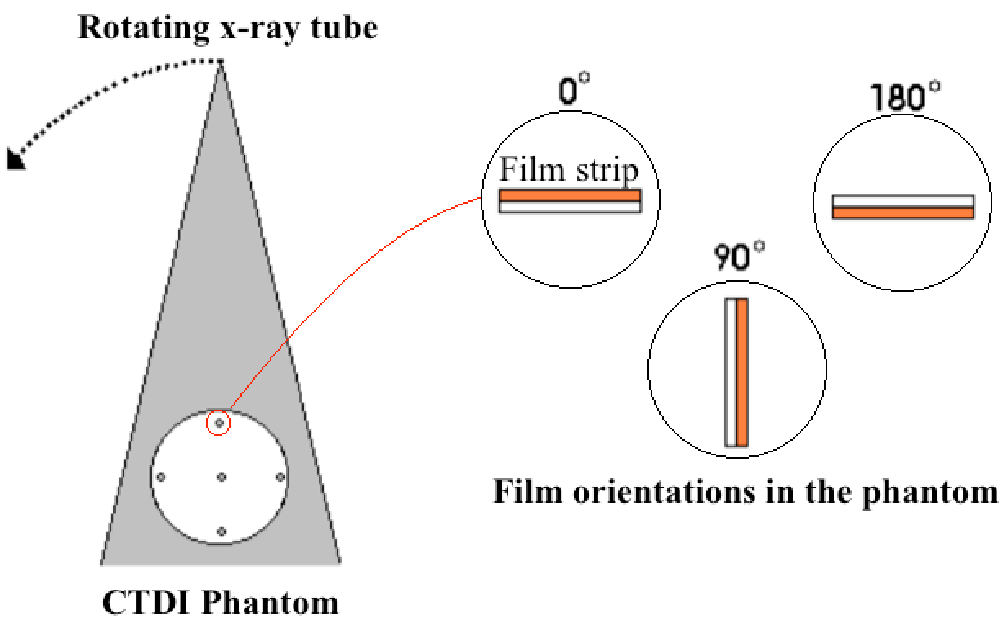

Figure 6.9. PMMA phantom for CTDI measurements holding a set of five strip of films aligned with the isocenter of the LightSpeed® CT Simulator while a full rotation scan is acquired. Films placed into the periphery holes of the PMMA phantom in different orientations.

The rotating x-ray tube test was repeated using body phantom described in ***Section 2.2*** to assess the effect of the object's size, *i.e.* the contribution of scattered radiation to the response of the film. Results are presented in ***Table 6.3***.

Peak energy (kVp)	Filter	HVL $(mmAl)$	Effective energy (keV)	mAs	Beam collimation (mm)	Phantom diameter (cm)
120	Head	7.3	47.7	600	8	16
120	Body	6.2	51.8	600	8	32

Table 6.3. Orientation dependence –Irradiation parameters of the rotating tube on the LightSpeed® CT Simulator.

Figure 6.10 shows the average response of the films placed into the holes of the head PMMA phantom after a full rotation of the x-ray tube, and the uncertainty in the response is shown in ***Figure 6.11***. Three different orientations of the films were studied in the periphery (0° corresponds to the active layer of the film facing the edge of the cylindrical phantom, 180° facing the center of the phantom, and 90° on to the radial direction of the phantom), while the orientation of the film placed in the central hole was arbitrarily selected.

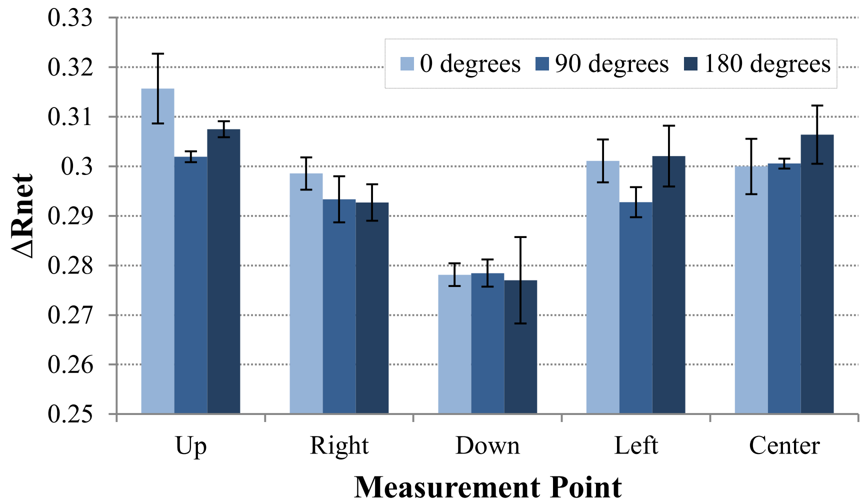

Figure 6.10. Film orientation response to the rotating X-ray tube on the LightSpeed® CT Simulator. Head phantom measurements. Error bars indicate the SD in $\Delta\bar{R}_{net}$.

The average responses $\Delta\bar{R}_{net}$ of films placed in the superior and lateral holes of the phantom (Up, Right, and Left) were consistently similar in value regardless of the film orientation ($\Delta\bar{R}_{net}]_{up} = 0.31$, $\Delta\bar{R}_{net}]_{right} = 0.29$, and $\Delta\bar{R}_{net}]_{left} = 0.30$). However $\Delta\bar{R}_{net}$ was slightly lower for the film placed in the bottom of the phantom ($\Delta\bar{R}_{net}]_{down} = 0.278$ in ***Figure 6.10***), as the radiation interacting at this point is already partially absorbed by the couch when the x-ray tube moved directly below the phantom. Finally for head phantom, the average response of the films was similar in the periphery and the center ($\Delta\bar{R}_{net}]_{center} = 0.30$). Due to a relatively small diameter of the head phantom, multiple contributions of the central beam at the center of the phantom compensate for the partial attenuation of individual beams reaching the measurement point. Film images were read-out as described in ***Section 2.6***.

Relative uncertainties $\sigma(\%)$ in the film response ΔR_{net}, were defined as:

$$\sigma(\%) = 100\ \% \cdot \frac{\sigma(\Delta R_{net})}{\Delta R_{net}}. \qquad [6.1]$$

For the head phantom this value ranged from 0.7 % to 6.3 % depending on the orientation and measurement point (***Figure 6.11***). The measurements in the center of the phantom, with orientations arbitrarily selected, presented an average uncertainty $\bar{\sigma}_{center}$ similar to the values corresponding to the periphery of the phantom ($\bar{\sigma}_{center} = 2.7$ %, $\bar{\sigma}_{up} = 2.1$ %, $\bar{\sigma}_{right} = 2.6$ %, $\bar{\sigma}_{left} = 3.0$ %, and $\bar{\sigma}_{dowm} = 3.3$ %). Nevertheless, when the uncertainty is averaged for the same orientation instead of measurement point, the response of the film appears to be less reproducible when its active layer is perpendicular to the axis of the central beam and faces the center of the phantom, this is at 180° ($\bar{\sigma}_{0°} = 2.8$ %, $\bar{\sigma}_{90°} = 2.0$ %, and $\bar{\sigma}_{180°} = 3.5$ %).

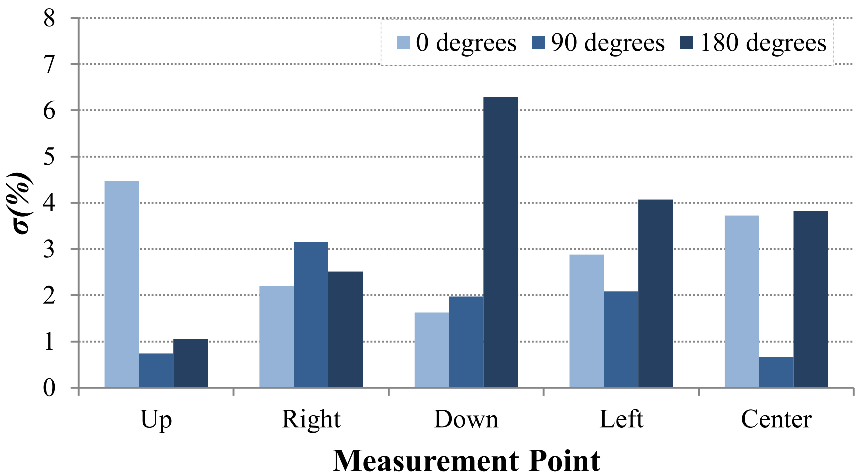

Figure 6.11. Film orientation response to the rotating x-ray tube of the LightSpeed® CT Simulator. Uncertainties in the head phantom measurements calculated using Equation 6.1 from data depicted in Figure 6.10.

Figure 6.12 and ***Figure 6.13*** show the responses of the films and their uncertainties when the body phantom was used to acquire a 1-slice axial scan (10 mm thick) in the LightSpeed® CT Simulator. The protocol used to scan the phantoms is summarized in ***Table 6.3***. The body phantom measurements carried out in the periphery were similar in value to each other, and again the measurement at the bottom plug of the phantom was 12 % lower in value, as observed with the head measurements described above. However, at the center of the phantom the signal measured was considerably lower than in the periphery ($\Delta\bar{R}_{net}]_{up} = 0.255$, $\Delta\bar{R}_{net}]_{right} = 0.25$, $\Delta\bar{R}_{net}]_{left} = 0.25$, $\Delta\bar{R}_{net}]_{down} = 0.22$, and $\Delta\bar{R}_{net}]_{center} = 0.17$), due to the increased attenuation of the beam through the larger phantom. The relative uncertainty $\sigma(\%)$ (as described in ***Equation 6.1***) for the body phantom measurements ranged from 0.1 % to 2.0 %, depending slightly on the measurement point and the film orientation, as shown in ***Figure 6.13***. While the uncertainties averaged for the same measurement points and film orientation were slightly different for the head phantom (***Figure 6.10***), the corresponding values for body were similar to each other ($\bar{\sigma}_{up} = 0.6\ \%$, $\bar{\sigma}_{right} = 0.3\ \%$, $\bar{\sigma}_{down} = 0.7\%$, and $\bar{\sigma}_{left} = 0.3\%$, $\bar{\sigma}_{0°} = 0.3\ \%$, $\bar{\sigma}_{90°} = 0.5\ \%$, and $\bar{\sigma}_{180°} = 0.6\ \%$).

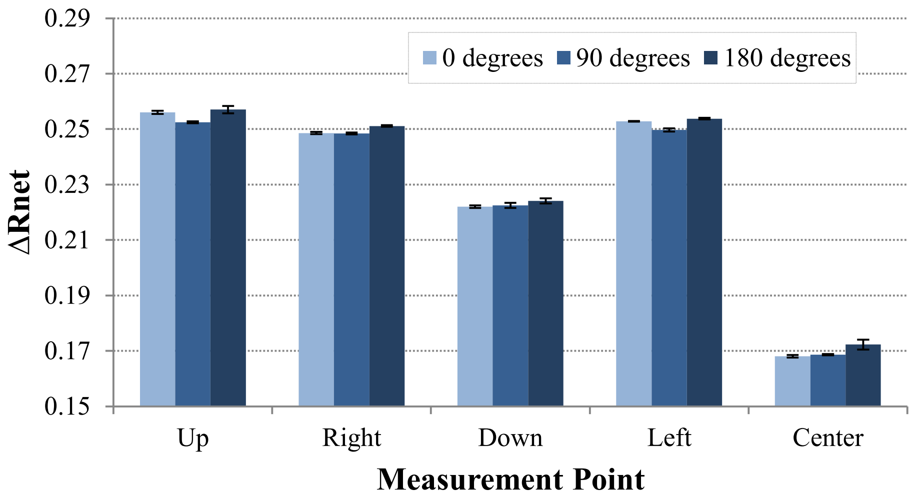

Figure 6.12. Film orientation response to the rotating x-ray tube of the LightSpeed® CT Simulator. In body phantom measurements. Error bars indicate the SD in $\Delta\bar{R}_{net}$.

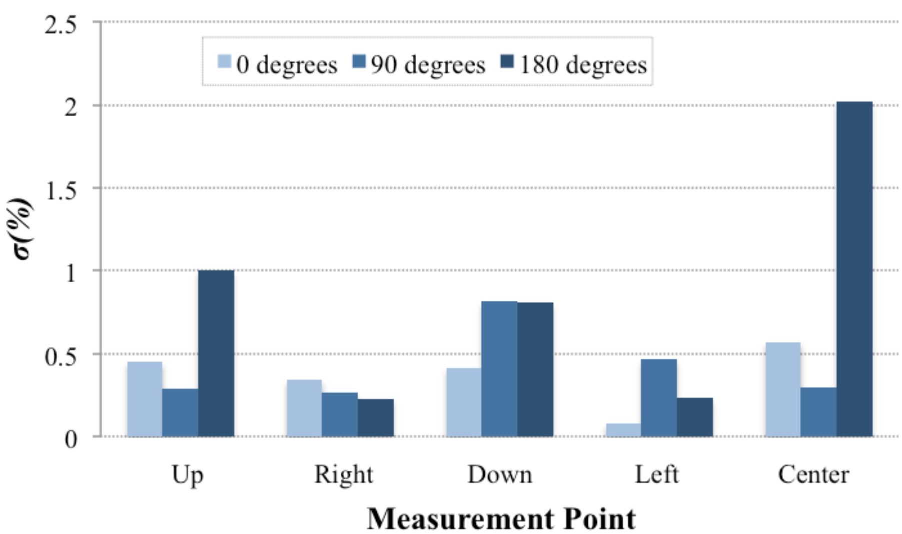

Figure 6.13. Film orientation response to the rotating x-ray tube of the LightSpeed® CT Simulator. Uncertainties in the in body phantom measurements calculated using Equation 6.1 from data depicted in Figure 6.12.

In order to compare the difference in the reflectance change as a function of film orientation, measurements with film's active layer facing the x-ray tube $\Delta\bar{R}_{net}]_{0°}$ were taken as a reference to create orientation response ratios ($\Delta\bar{R}_{net}]_{90°}/\Delta\bar{R}_{net}]_{0°}$ and $\Delta\bar{R}_{net}]_{180°}/\Delta\bar{R}_{net}]_{0°}$) for both head and body phantoms, as shown in ***Figure 6.14*** and ***Figure 6.15***. In this sense, the calculated percent difference between any film orientation and the reference orientation $\Delta\bar{R}_{net}]_{0°}$ can be used to assess the uncertainty associated with the orientation of the film. In general, a slightly larger change in the reflectance of the film (~2 %) was obtained when the active layer faced the x-ray tube with the head phantom, with $\Delta\bar{R}_{net}]_{90}/\Delta\bar{R}_{net}]_{0°} < 1$, and $\Delta\bar{R}_{net}]_{180}/\Delta\bar{R}_{net}]_{0°} \approx 1$. On the other hand, when the body phantom is used, a higher change in the reflectance of the film (~1 %) was observed if its opaque layer is facing the x-ray tube: $\Delta\bar{R}_{net}]_{90}/\Delta\bar{R}_{net}]_{0°} < 1$ and $\Delta\bar{R}_{net}]_{180}/\Delta\bar{R}_{net}]_{0°} > 1$. For all the cases, in both the head and body phantom, the uncertainty associated with the orientation of the film was smaller than the uncertainty in the measurement of the reflectance change individually for each orientation, as previously confirmed with the static x-ray tube test, presented in ***Section 6.2*** (***Table 6.2***).

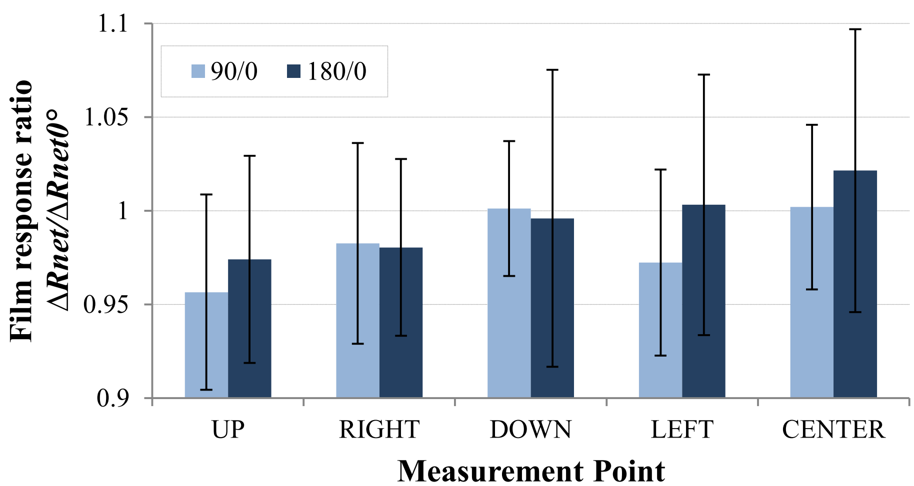

Figure 6.14. Film orientation response to the rotating X-ray tube of the LightSpeed® CT Simulator. Film response ratios in the head phantom, the error bars indicate the SD in $\Delta\bar{R}_{net}]\ \ /\Delta\bar{R}_{net}]_{0°}$.

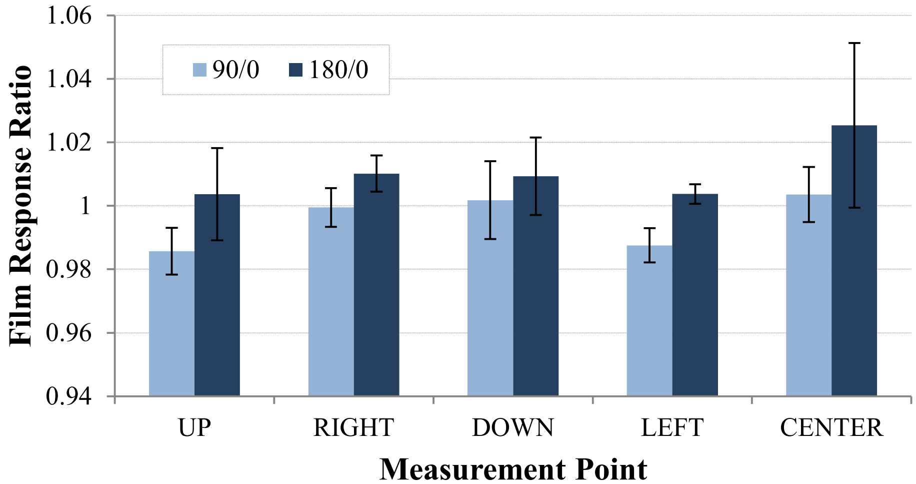

Figure 6.15. Film orientation response to the rotating X-ray tube of the LightSpeed® CT Simulator. Film response ratios in the body phantom, the error bars indicate the SD in $\Delta\bar{R}_{net}]\ \ /\Delta\bar{R}_{net}]_{0°}$.

7. Film Absorbed-Dose – Energy Dependence

7.1 Effective photon energy range

A set of calibration curves $\Delta R_{Net}([K_{air}]_{air}, Q)$ for 19 beam qualities (Q) were compared in order to assess the Gafchromic® XR-QA2 film model response dependence with E_{eff}. The average film response function for a given $[K_{air}]_{air}$ value was calculated over the $5\ mGy \leq [K_{air}]_{air} \leq 100\ mGy$ range.

Seven additional beam qualities delivered by the Xstrahl 300 orthovoltage therapy unit were added to Q values obtained for the LightSpeed® CT Simulator presented in **Section 5.2.1** (***Table 5.3***). This was done to broaden the effective photon energy range to be studied. A standard calibration protocol used clinically for the orthovoltage machine was used. It includes *HVL* and output measurements used to calculate the $[K_{air}]_{air}$ values to expose the calibration film (as described in ***Section 5.1***), as shown in ***Table 7.1***. Six calibration curves were then created for the same number of Orthovoltage beam qualities to broaden the effective photon energy range to be studied. ***Figure 7.1*** shows the beam qualities used to create calibration curves according to the imaging device used to produce the photon beam.

Peak energy (kVp)	HVL	Filter	Effective energy (keV)	Output (MU/cGy)	Applicator	
					Shape	Length
50	0.16 mmAl	8	12.74	7.39	5cm diameter	30cm
50	0.33 mmAl	1	15.5	22.57	10cm x 10cm	20cm
70	1.38 mmAl	3	23.47	9.655	5cm diameter	30cm
80	2.18 mmAl	2	29.5	10.19	5cm diameter	30cm
120	4.19 mmAl	4	41.8	7.765	5cm diameter	30cm
180	3.00 mmCu	6	64	7.795	6cm diameter	31cm

Table 7.1. Xstrahl 300 Orthovoltage Therapy Unit beam qualities for peak energy and filter/applicator used.

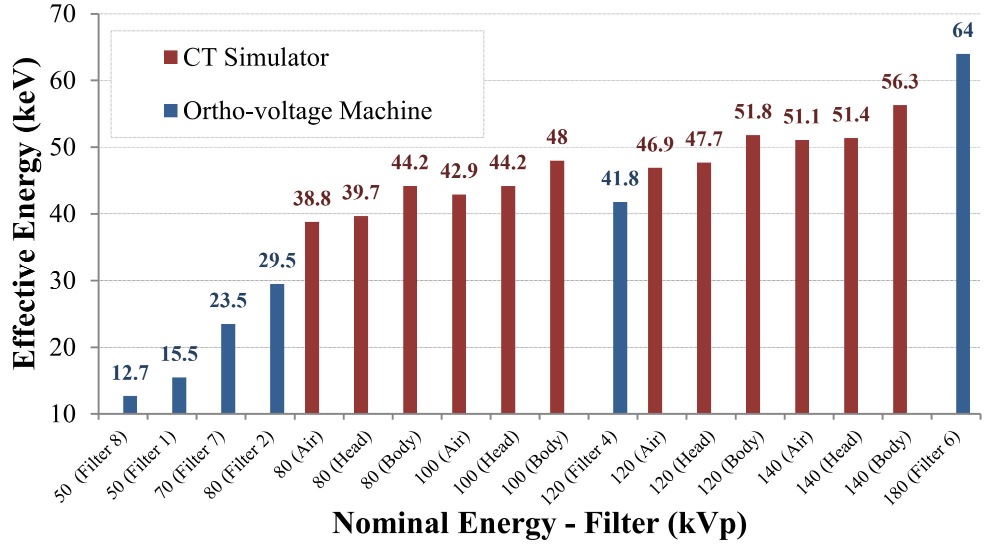

Figure 7.1. Beam qualities used for this study. The Xstrahl 300 orthovoltage energies are shown in blue, with filters provided in parentheses. The LightSpeed® CT Simulator energies are shown in red with internal filtration specification provided in parentheses. Filter/applicator characteristics of the Xstrahl 300 unit are provided in ***Table 7.1.***

7.2 Calibration curves

Calibration curves were created for the 18 beam qualities shown in ***Figure 7.1***. All curves were compared to see differences in the net reflectance change of the film ΔR_{Net} for the same $[K_{air}]_{air}$ values as a function of E_{eff}. ***Figure 7.2*** shows 18 calibration curves as function of $[K_{air}]_{air}$ values. A cluster of 16 curves defines a clear zone where the response of the film is quasi-stable. This region corresponds to calibration curves of beam qualities whose E_{eff} are within the recommended energy specifications for the radiochromic film ($20 - 200$ keV) [32]. Therefore, it was expected that the film response to 12.7 keV and 15.5 keV diverged considerably from the rest of energies. These low energies were discarded from the pool used to assess the film energy dependence, leaving 16 energies for the analysis in the $E_{eff} = 23.5 - 64.0$ keV range.

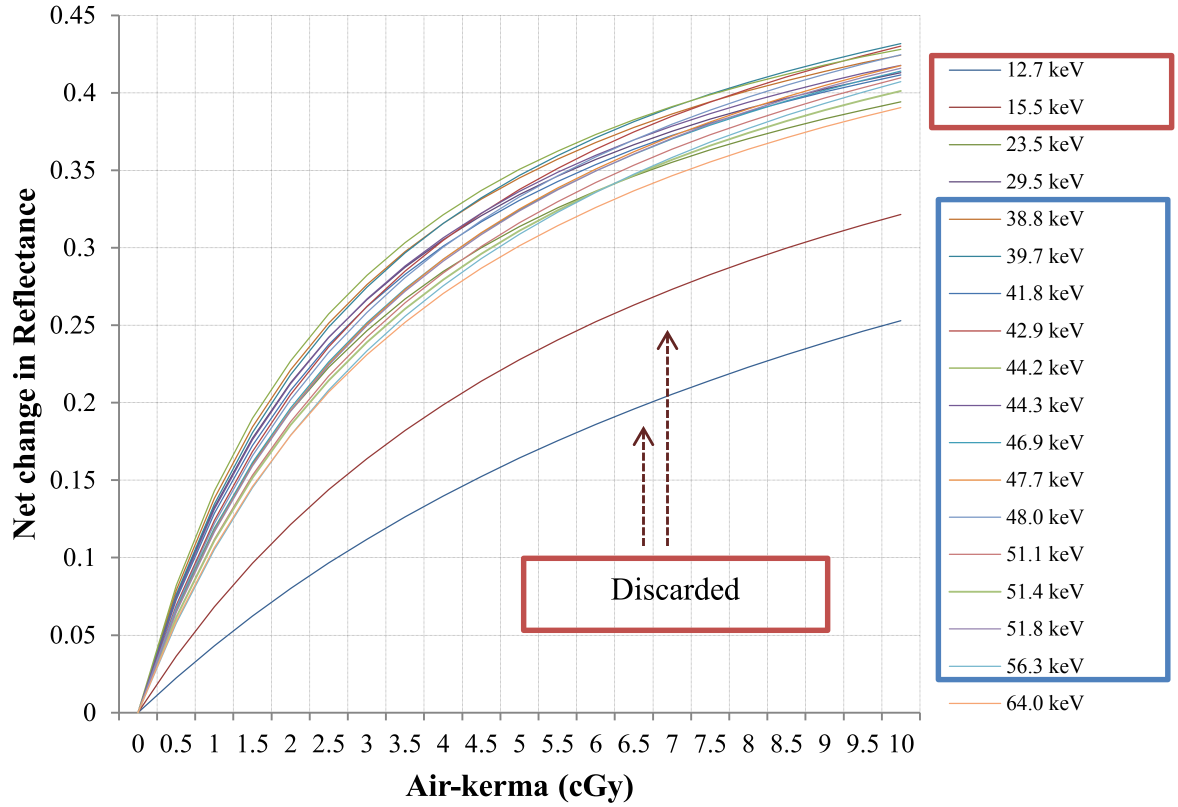

Figure 7.2. Gafchromic® XR-QA2 film response curves for 18 beam qualities of the LightSpeed® CT Simulator and the Xstrahl 300 orthovoltage unit. The arrows indicate the beam quality curves (12.7 and 15.5 keV) discarded from further analysis.

Figure 7.3 describes qualitatively the film response by suggesting three areas in the film response graph according to the E_{eff} of the beam used to irradiate it. The first zone (in blue) corresponds to the film response to photon beams of E_{eff} below of the film specifications (<20 keV) [32]. The second zone (in gray) contains the response of the film to medium-energy beams (38.8 – 48.0 keV). The third zone (in red) shows the film response to high-energy radiation (48.0 – 64.0 keV). According to these results, as the E_{eff} of the beam used to irradiate the film increases, a lower variation in the net reflectance of the film ΔR_{Net} is observed, as expected due to the composition of the active layer (high Z materials) and the recommendations of the manufacturer [32].

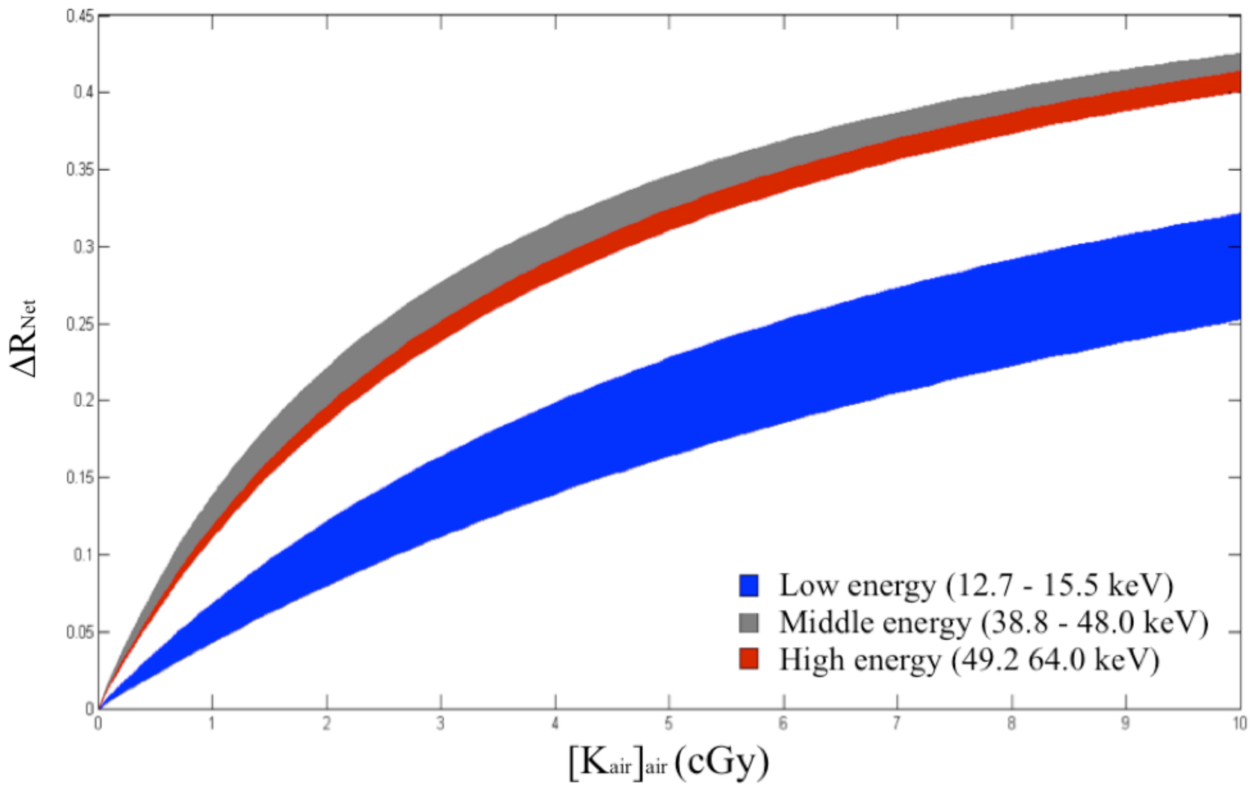

Figure 7.3. Film response to ionizing radiation of beam energies in the E_{eff} range of 12.7 – 64.0 keV.

7.3 Change in the film response as a function of Effective Energy

The Gafchromic® XR-QA2 film calibration curves $\Delta R_{Net}([K_{air}]_{air}, Q)$ were evaluated for a fixed $[K_{air}]_{air}$ value, so that the average response $\Delta\bar{R}_{net}([K_{air}]_{air})$ and its standard deviation $\delta_{\Delta R_{Net}}$ could be calculated as

$$\Delta\bar{R}_{net}([K_{air}]_{air}) = average\big(\Delta R_{Net}([K_{air}]_{air}, Q_i)\big), \quad [7.1]$$

$$\delta_{\Delta R_{Net}}([K_{air}]_{air}) = SD\big(\Delta R_{Net}([K_{air}]_{air}, Q_i)\big). \quad [7.2]$$

The relative variance in the film response $\Gamma(k)$ for a particular air-kerma value k was then defined as:

$$\Gamma(k) = \frac{\delta_{\Delta R_{Net}}([K_{air}]_{air})}{\Delta \bar{R}_{net}([K_{air}]_{air})}. \quad [7.3]$$

The relative variance $\Gamma([K_{air}]_{air})$ for the film was plotted as a function of $[K_{air}]_{air}$ to evaluate the uniformity on the response of the film over the 5 mGy $\leq [K_{air}]_{air} \leq 100$ mGy range. If the polymerization process carried out in the active layer of the film was not energy dependent, the calibration curves $\Delta R_{Net}([K_{air}]_{air}, Q_i)$ would be the same for all Q_i. In that case, as the response of the film would depend only on the dose absorbed during the irradiation, $\delta_{\Delta R_{Net}}(k)$ would be zero for all k values, and so would be the $\Gamma(k)$ function.

Equation 5.14 describes the net change in the film reflectance ΔR_{net} as a function of parameters α and β, which were proved to be energy dependent film parameters, as seen in ***Figure 5.11.*** Consequently, for the same $[K_{air}]_{air}$ value, the film response to radiation depends on the E_{eff} of the photon beam interacting with the active layer. In order to quantify this change, calibration curves were evaluated at the same $[K_{air}]_{air}$, and the variation in the film response $\delta_{\Delta R_{Net}}([K_{air}]_{air})$ was then calculated according to ***Equation 7.2***. ***Figure 7.4*** shows the dependence of absolute and percent variation of the film response $\delta_{\Delta R_{Net}}$ on $[K_{air}]_{air}$. ***Table 7.2*** condenses the average absolute and relative variation of the film response $\Delta \bar{R}_{net}$ for each one of these ranges.

$[K_{air}]_{air}$ range (mGy)	Absolute $\Delta \bar{R}_{net}$ variation	Percent $\Delta \bar{R}_{net}$ variation (%)
5 -35	0.013 ± 0.003	7.7 ± 1.5
35 – 80	0.0139 ± 0.0007	4.4 ± 0.8
80 – 100	0.0122 ± 0.0003	3.1 ± 0.2
5 – 100	0.013 ± 0.002	4.9 ± 2.1

Table 7.2. Film response variation in the 23.5 – 64.0 keV effective energy range.

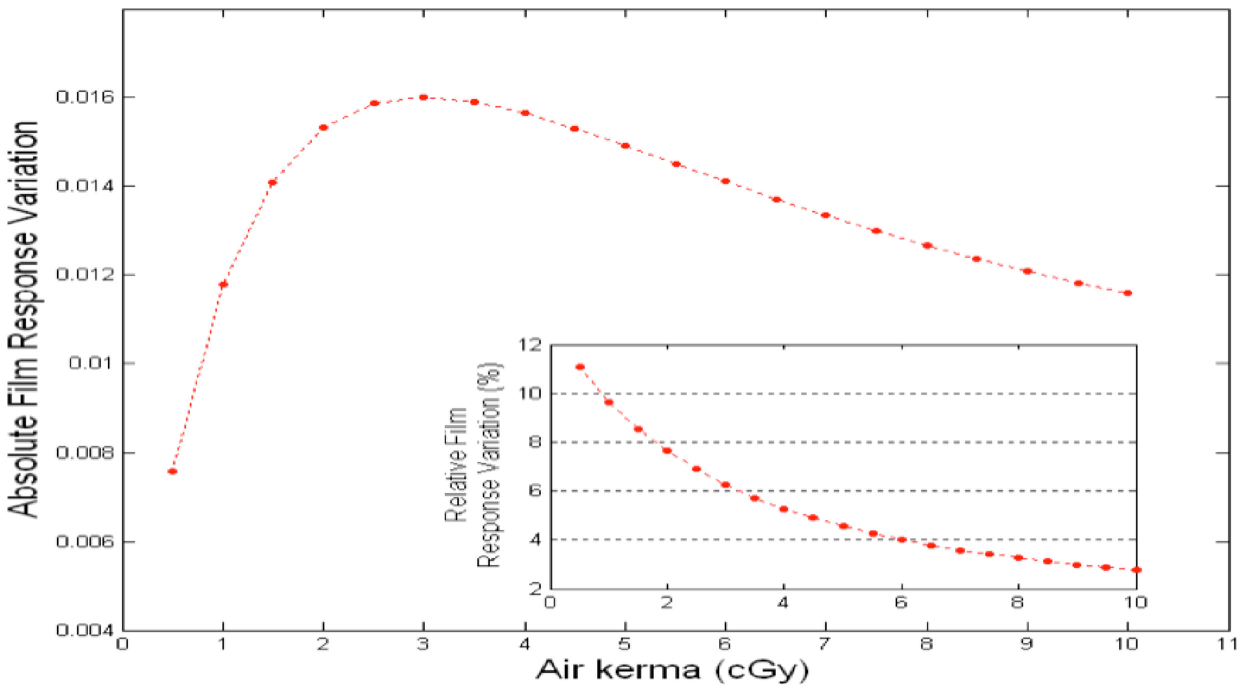

Figure 7.4. Absolute and percent variation in the film response over the 38.8 to 64.0 keV effective energy range.

8. CTDI Measurements

8.1 $CTDI_{vol}$ tabulated data

The CTDI measurement protocol is described in Section 3.1. This protocol was followed to scan the PMMA phantom on five imaging machines: the General Electric LightSpeed® CT Simulator, the Brilliance® Big Bore CT Simulator, and the On Board Imager® (OBI) devices attached to the Clinical iX Linear Accelerator, the TrueBeam® System and the Trilogy Linear Accelerator. Multiple imaging protocols were selected on each device and tested multiple times to assess the reproducibility of the method.

Each scanning protocol was repeated three times, so that the average and standard deviation on the measured $CTDI_{vol}|_{XR-QA2}$ value could be assessed and compared to the corresponding value displayed by the imaging device during the irradiation $CTDI_{vol}|_{tabulated}$. ***Table 8.1*** presents the imaging protocol used for CTDI measurements.

Imaging system	Device	Protocol
CT simulator	LightSpeed®	Axial head
		Multi-axial head
		Helical thorax
		Helical pelvis.
	Brilliance®	Axial head
		Multi-axial head
		Helical pelvis.
OBI	iX	Cone beam geometry for head, thorax and pelvis
	TrueBeam®	
	Trilogy	

Table 8.1. Imaging protocols followed to carry out CTDI measurements.

A total of 26 scanning protocols were used to image the CTDI PMMA phantom containing Gafchromic® XR-QA2 films. The $CTDI_{vol}$ values displayed by the device ($CTDI_{vol}|_{tabulated}$) during the procedure are shown in ***Figure 8.1***. The majority (68 %) of $CTDI_{vol}|_{tabulated}$ values for the imaging protocols contained in ***Table 8.1*** falls within the low $5 - 30$ mGy dose range. On the other hand, fewer of the $CTDI_{vol}|_{tabulated}$ values ($21\,\%$) are expected to be in the $30 - 70$ mGy bracket, while the $70 - 100$ mGy band covers minority of the tabulated values (11 %). These values are sorted in ascending order: 68 % of $CTDI_{vol}|_{tabulated}$ are lower than 30 mGy, 89 % lower than 70 mGy, and all the $CTDI_{vol}|_{tabulated}$ values lower than 85 mGy. ***Table 8.2*** correlates the $CTDI_{vol}|_{tabulated}$ values shown in ***Figure 8.1*** to the imaging parameters of the protocol used to scan the PMMA phantom.

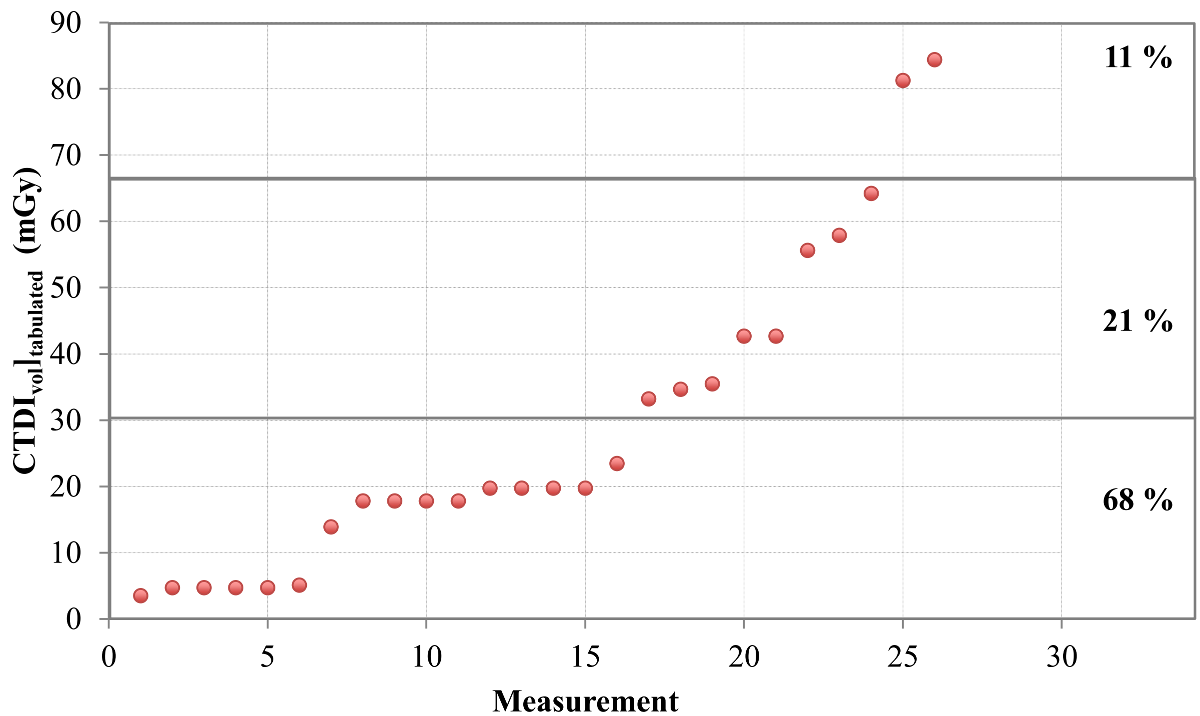

Figure 8.1. Tabulated CTDI$_{vol}$ values registered during the film-based protocol for CTDI measurements. Data is sorted in ascending order for 26 imaging protocols delivered by the imaging devices cited in ***Table 8.1***.

$CTDI_{vol}\|_{tabulated}$ (mGy)	Phantom/filter	Peak energy (kVp)	Effective energy (keV)	mAs
3.5	Body	125	50.0	26
4.73	Body	110	42.9	40
5.1	Head	100	37.7	26
13.9	Body	125	50.0	105
17.79	Body	125	49.1	104
19.76	Head	100	41.3	200
23.44	Body	120	49.8	300
33.2	Body	120	41.4	500
34.67	Body	120	49.7	860
35.48	Body	120	49.7	440
42.7	Head	120	41.4	300
55.62	Head	120	49.5	860
57.9	Head	120	49.5	300
64.21	Head	120	49.5	300
81.26	Head	120	49.5	860
84.39	Head	120	49.5	600

Table 8.2. Imaging protocol parameters.

The performance of this dosimetry system was tested for 26 scanning protocols: 1-slice-axial (3 protocols), multi-axial (4 protocols), and helical (4 protocols) on CT simulators, and cone-beam geometry (15 protocols) on OBI devices. The body PMMA phantom was scanned by 15 protocols and the head phantom by 11 protocols. ***Appendix 5*** is an example of the format used to record raw and processed data during the CTDI measurements.

8.2 $CTDI_{vol}$ measurements on CT Simulators

For each protocol used to scan the CTDI phantom, the radiochromic film protocol for CTDI measurements was repeated three times in order to test the reproducibility of the method. ***Figure 8.2*** and ***Figure 8.3*** compare $CTDI_{vol}|_{tabulated}$ values to film-measured $CTDI_{vol}$ values ($CTDI_{vol}|_{XR-QA2}$) acquired on CT simulators. Thus, $CTDI_{vol}|_{Tabulated}$ values appear in red followed by three $CTDI_{vol}|_{XR-QA2}$ measurements in blue, all of them acquired using the same imaging protocol. Seven protocols were used to measure $CTDI_{vol}$values on the LightSpeed® CT Simulator (***Figure 8.2***): two 1-slice head scans, two head multi-axial, two helical thorax, and one pelvis-helical protocol, as detailed in ***Table 8.3***. The negative value corresponding to the $CTDI_{vol}$ measurement of the "Head multi-axial II" imaging protocol showed in ***Table 8.3*** is consequence of the improper handling of the film control strip. It was accidentally exposed to scattered radiation in the CT room during one of the phantom irradiations. Nevertheless, the response of the film to such a small dose is imperceptible to the naked eye, and it was included in the analysis. This clearly shows that the accuracy of the $CTDI_{vol}|_{XR-QA2}$ measurement is highly dependent on the proper handling of the control film.

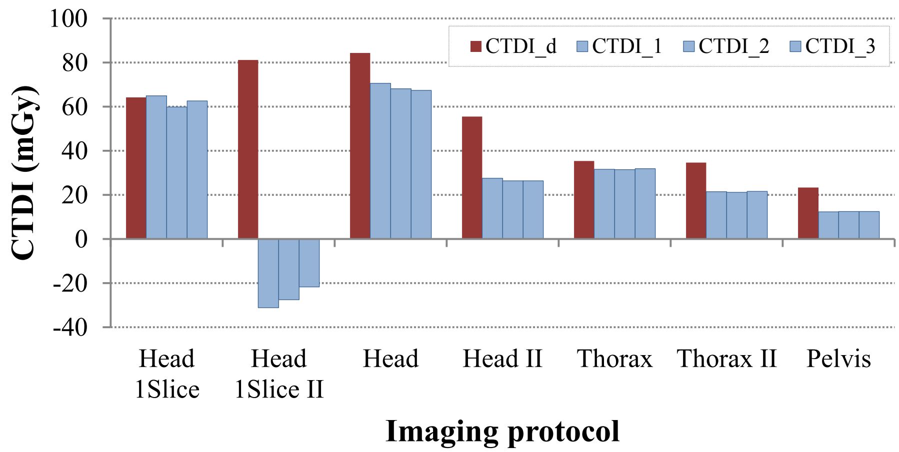

Figure 8.2. Comparison between $CTDI_{vol}|_{tabulated}$ and $CTDI_{vol}|_{XR-QA2}$ values acquired on the General Electric LightSpeed® CT Simulator. Measured data in blue ($CTDI_{1,2,3}$) and tabulated data in red ($CTDI_d$).

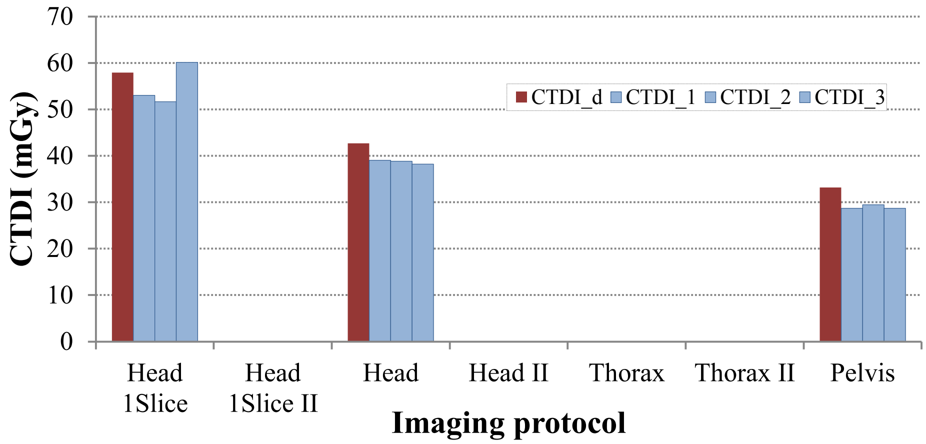

Figure 8.3. Comparison between $CTDI_{vol}|_{tabulated}$ and $CTDI_{vol}|_{XR-QA2}$ values acquired on the Philips Brilliance® Big Bore CT Simulator. Measured data in blue ($CTDI_{1,2,3}$) and tabulated data in red ($CTDI_d$).

Imaging protocol	Head 1-slice I	Head 1-slice II	Head multi-axial I	Head multi-axial II	Thorax helical	Thorax helical II	Pelvis helical
Peak energy (kVp)	120	120	120	120	120	120	120
Phantom/filter	Head	Head	Head	Head	Body	Body	Body
mAs	300	600	440	860	860	860	300
Pitch	-	-	-	-	0.989	0.989	0.986
$CTDI_{vol}\|_{Tabulated}$ (mGy)	64.21	84.39	35.48	81.26	55.62	34.67	23.44
$CTDI_{vol}\|_{XRQA-2}$ (mGy)	62.49	68.76	31.71	-26.67	26.8	21.44	12.5
Uncertainty in $CTDI_{vol}\|_{XRQA-2}$ (%)	3.28	2.02	0.41	0.18	1.99	0.84	0.95

Table 8.3. General Electric LightSpeed® CT Simulator CTDI measurements.

In general, measured $CTDI_{vol}|_{XR-QA2}$ was consistently lower than $CTDI_{vol}|_{Tabulated}$. The difference was 2.8 % on average for the 1-slice I scan, 10.6 % on average for multi-axial scans, and 45.5 % on average for helical scans. However, regardless of the imaging protocol, the uncertainty in the measurements was constrained within a narrow margin (1.58 % on average).

To complete the study on CT Simulators, three additional protocols were included on the Philips Brilliance® Big Bore CT Simulator (***Figure 8.3***). These were one 1-slice axial head scan, one multi-axial head, and one helical pelvis scans. ***Table 8.4*** summarizes general results for this device.

The Brilliance® CT Simulator exhibits the same trend as observed with the LightSpeed® CT Simulator. Namely, $CTDI_{vol}|_{XR-QA2}$ values were consistently lower than $CTDI_{vol}|_{Tabulated}$. Film measurements were 5.10 % lower than $CTDI_{vol}|_{Tabulated}$ values for the 1-slice scan, 9.4 % lower for the head multi-axial scan, and 12.7 % lower for the helical scan. Additionally, the relative uncertainty in the measurement was low, constant and irrespective of the imaging protocol used to irradiate the phantom (0.80 %).

Imaging protocol	Head 1-slice	Head multi-axial	Helical Brachy pelvis
Peak energy (kVp)	120	120	120
Phantom/filter	Head	Head	Body
mAs	300	300	500
Pitch	-	-	0.967
$CTDI_{vol}|_{Tabulated}$ (mGy)	57.9	42.7	33.2
$CTDI_{vol}|_{XRQA-2}$ (mGy)	54.95	38.69	28.98
Uncertainty in $CTDI_{vol}|_{XRQA-2}$ (%)	0.2	0.95	1.25

Table 8.4. Philips Brilliance® Big Bore CT Simulator CTDI measurements.

In summary, $CTDI_{vol}$ values measured for CT simulator scanners were constantly lower than their nominal values, and the disagreement between measured and tabulated $CTDI_{vol}$ values is strongly dependent on the nature of the irradiation protocol used to produce the image. Accordingly, CTDI values for 1-slice axial scans were on average 3.6 % lower than expected, multi-axial scans were 10.3 % lower, and helical scans were 29.1 % lower. ***Figure 8.4*** illustrates the relation between $CTDI_{vol}|_{XR-QA2}$ and $CTDI_{vol}|_{Tabulated}$.

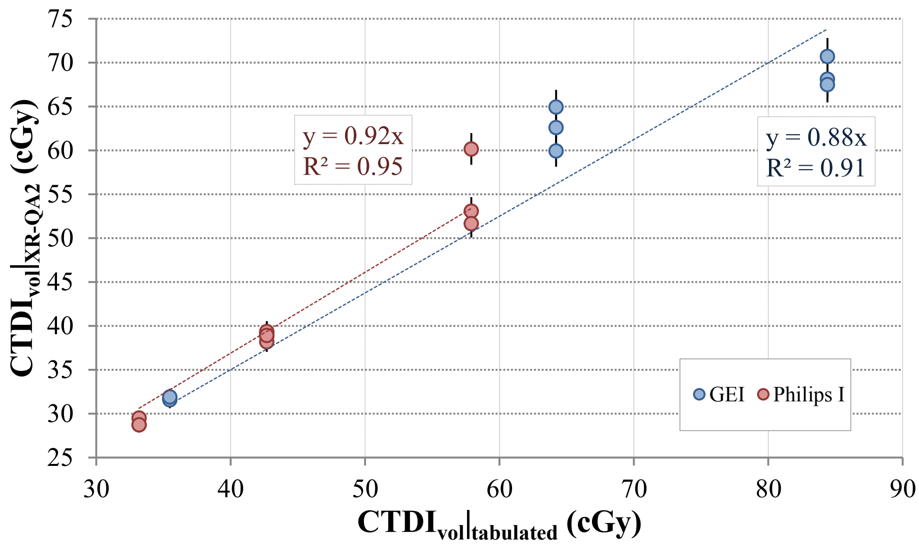

Figure 8.4. Linear correlation between measured and tabulated $CTDI_{vol}$ values on CT simulators: LightSpeed® in blue and Brilliance® in red.

A linear correlation between $CTDI_{vol}|_{XRQA-2}$ and $CTDI_{vol}|_{Tabulated}$ was determined for each CT Simulator, and the performance of the radiochromic protocol was assessed in terms of the slope m of the fitting function and its correlation coefficient R^2. A relatively high correlation was observed for both devices ($R_{GE}^2 = 0.95$, and $R_{Philips}^2 = 0.91$), and apparent underestimation in dose measurements using Gafchromic® XR-QA2 film was related to the slope of the fitting models, which were in both cases lower than unity ($m_{GE} = 0.92$, and $m_{Philips} = 0.88$).

8.3 $CTDI_{vol}$ measurements on kV Cone Beam CT devices on Linacs

Figures 8.5** – **8.7 summarize the $CTDI_{vol}|_{XR-QA2}$ values obtained for 15 imaging protocols delivered by three On Board Imager® devices. Three scanning protocols were followed on the Clinical iX Linear Accelerator, each repeated twice to test the reproducibility of the radiochromic CTDI measurements method over time. ***Table 8.5*** provides scanning parameters for each protocol.

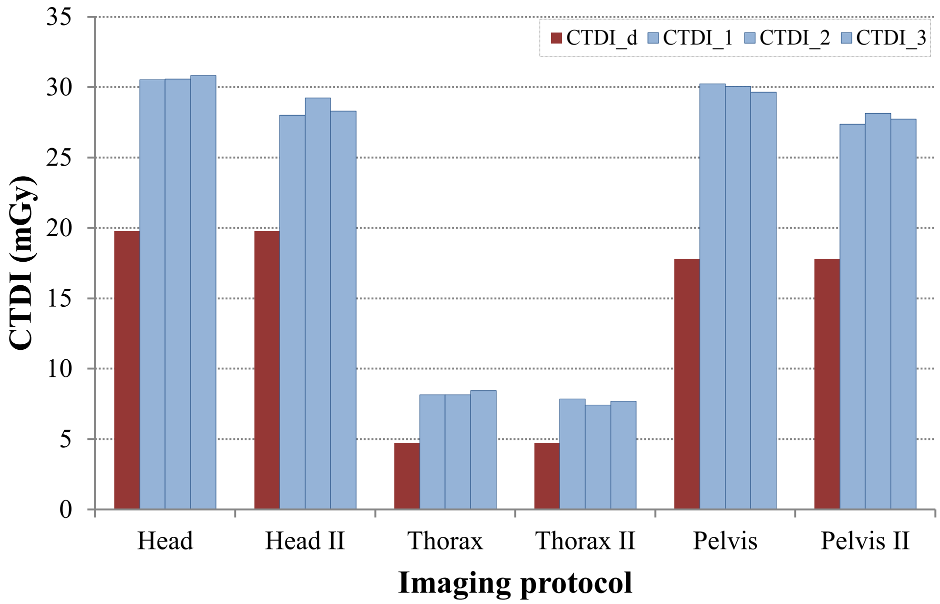

Figure 8.5. Comparison between $CTDI_{vol}|_{tabulated}$ and $CTDI_{vol}|_{XR-QA2}$ values acquired on the OBI system coupled to the Clinical iX Linear Accelerator. Measured data are shown in blue ($CTDI_{1,2,3}$) and tabulated data in red ($CTDI_d$).

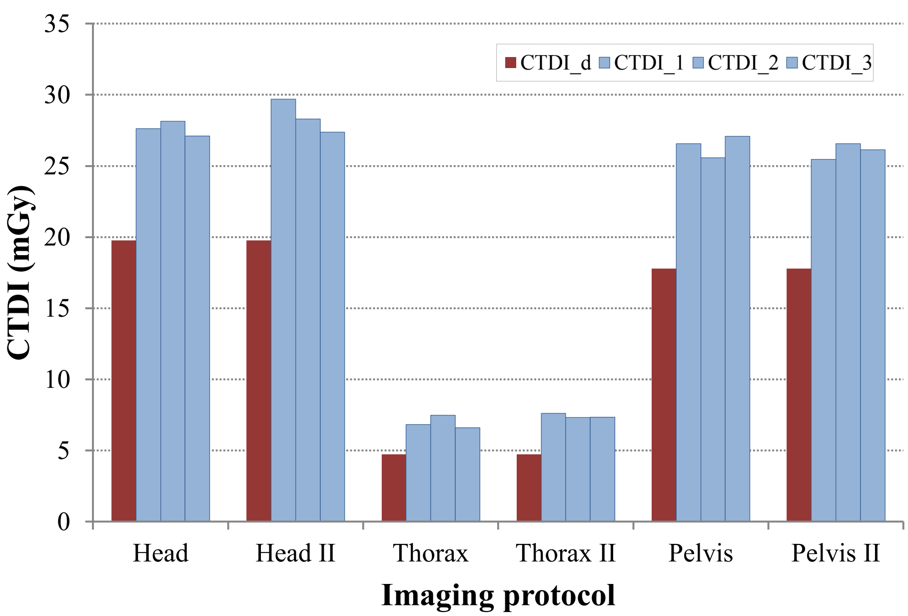

Figure 8.6. Comparison between $CTDI_{vol}|_{tabulated}$ and $CTDI_{vol}|_{XR-QA2}$ values acquired on the OBI system coupled to the Trilogy Linear Accelerator. Measured data are shown in blue ($CTDI_{1,2,3}$) and tabulated data in red ($CTDI_d$).

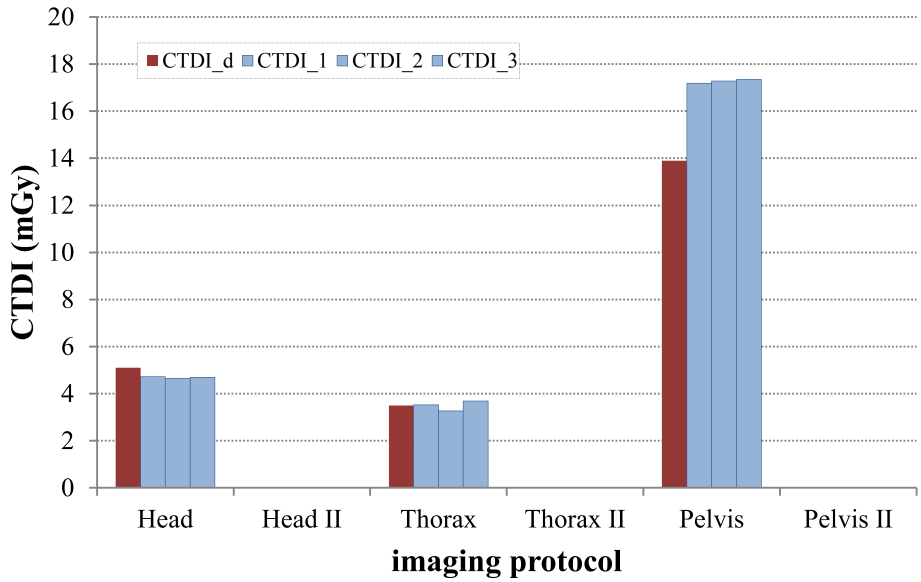

Figure 8.7. Comparison between $CTDI_{vol}|_{tabulated}$ and $CTDI_{vol}|_{XR-QA2}$ values acquired on the OBI system coupled to the TrueBeam System. Measured data are shown in blue ($CTDI_{1,2,3}$) and tabulated data in red ($CTDI_d$).

For the OBI CBCT on the Clinical iX Linear Accelerator, $CTDI_{vol}|_{XR-QA2}$ was constantly higher than $CTDI_{vol}|_{Tabulated}$ (Tabulated data is shown in ***Section 8.1***). On average, it was 49.7 % higher for head scans, 68.8 % for thorax scans, and 53.3 % for pelvis scans. Although measured results were much higher than tabulated data, the variation over time was low. Regardless of the imaging protocol, the uncertainty in the measurements was consistently lower than 2.3 %. Dose measurements carried out with the film for CTDI calculation showed a high reproducibility. The variation of measured doses accounted in average 1.1 % for head scans and 1.5 % for body scans.

	Imaging protocol					
	High-Quality Head I	High-Quality Head II	Low-Dose Thorax I	Low-Dose Thorax II	Pelvis (Prostate) I	Pelvis (Prostate) II
Clinical iX Linear Accelerator						
Peak energy (kVp)	100	100	110	110	125	125
Phantom/filter	Head	Head	Body	Body	Body	Body
mAs	200	200	440	440	860	860
$CTDI_{vol}\|_{Tabulated}$ (mGy)	19.76	19.76	4.73	4.73	17.79	17.79
$CTDI_{vol}\|_{XR-QA2}$ (mGy)	30.65	28.52	8.24	7.65	26.8	27.75
Uncertainty in $CTDI_{vol}\|_{XRQA-2}$ (%)	0.41	1.81	1.6	2.28	0.83	1.12
Trilogy Linear Accelerator						
Peak energy (kVp)	100	100	110	110	125	125
Phantom/filter	Head	Head	Body	Body	Body	Body
mAs	200	200	440	440	860	860
$CTDI_{vol}\|_{Tabulated}$ (mGy)	19.76	19.76	4.73	4.73	17.79	17.79
$CTDI_{vol}\|_{XR-QA2}$ (mGy)	27.62	28.46	6.97	7.43	24.41	26.06
Uncertainty in $CTDI_{vol}\|_{XRQA-2}$ (%)	1.55	3.32	5.37	1.69	2.35	1.76

Table 8.5. Clinical iX Linear Accelerator and Trilogy Linear Accelerator CTDI Measurement.

The same general scanning protocols presented in ***Table 8.5*** for the Clinical iX Linear Accelerator were tested on the Trilogy Linear Accelerator. Similarly, scans were repeated over time to assess the reproducibility of the dosimetry method. Similar results were obtained for the OBI CBCT coupled to the Trilogy Linear Accelerator and the Clinical iX Linear Accelerator. $CTDI_{vol}|_{XRQA-2}$ was constantly higher than $CTDI_{vol}|_{Tabulated}$. The difference between tabulated and measured $CTDI_{vol}$ values was similar for both imaging devices, as well as the variation of $CTDI_{vol}|_{XRQA-2}$ over time. The $CTDI_{vol}|_{XR-QA2}$ values were on average 41.9 %

higher for head scans, 52.2 % for thorax scans, and 41.8 % for pelvis scans, while the uncertainty in the measurement was on average 2.4 % for head scans and 2.8 % for body scans.

Finally, three imaging protocols were studied on the OBI CBCT coupled to the TrueBeam System, but they were not repeated over time. Selected protocols parameters were similar to the parameters chosen on other OBY® systems, and the results are presented in ***Table 8.6***.

Imaging protocol	High-Quality Head	Low-Dose Thorax	Pelvis (Prostate)
Peak energy (kVp)	100	125	125
Phantom/filter	Head	Body	Body
mAs	264	264	1055
$CTDI_{vol}\|_{Tabulated}$ (mGy)	5.1	3.5	13.9
$CTDI_{vol}\|_{XRQA-2}$ (mGy)	4.7	3.5	17.27
Uncertainty in $CTDI_{vol}\|_{XRQA-2}$ (%)	0.59	4	0.4

Table 8.6. TrueBeam® System CTDI Measurements.

When compared to $CTDI_{vol}|_{XR-QA2}$ measured on the Trilogy and iX Linear Accelerators, the TrueBeam® *OBI* exhibits higher accuracy. Additionally, the absolute and relative differences between measured $CTDI_{vol}|_{XR-QA2}$ and displayed $CTDI_{vol}|_{Tabulated}$ for the TrueBeam® System were the smallest among the three systems. The $CTDI_{vol}|_{XR-QA2}$ values for the head protocol were on average 0.49 mGy lower (−7.9 %) than $CTDI_{vol}|_{Tabulated}$, and measured values for the low-dose thorax protocol were in good agreement with the displayed data (− 0.004 mGy, or −0.12 %). However, a considerable discrepancy was noted for the pelvis scan protocol, where $CTDI_{vol}|_{XR-QA2}$ was 3.37 mGy higher than $CTDI_{vol}|_{Tabulated}$ (+ 24.3 %).

A linear correlation was found for $CTDI_{vol}|_{XR-QA2}$ and $CTDI_{vol}|_{Tabulated}$ data measured on OBI systems, as shown in ***Figure 8.8***. The performance of the Gafchromic® XR-QA2 film dosimetry protocol was assessed in terms of the slope m and correlation coefficient R^2 of the fitting model (intercept set to $y = 0$). Although both curves exhibit a positive slope greater than unity, the difference in their magnitude indicates a significant overestimation of the dose delivered by the first set of imaging devices ($m_{iX\&TR} = 1.50$, $m_{TB} = 1.19$). As a way to compare the performance of the film based dosimetry protocol for CTDI determination, data for CT simulators were grouped and plotted as a function of tabulated data, and the same applied for OBI devices. This can be seen in ***Figure 8.9***.

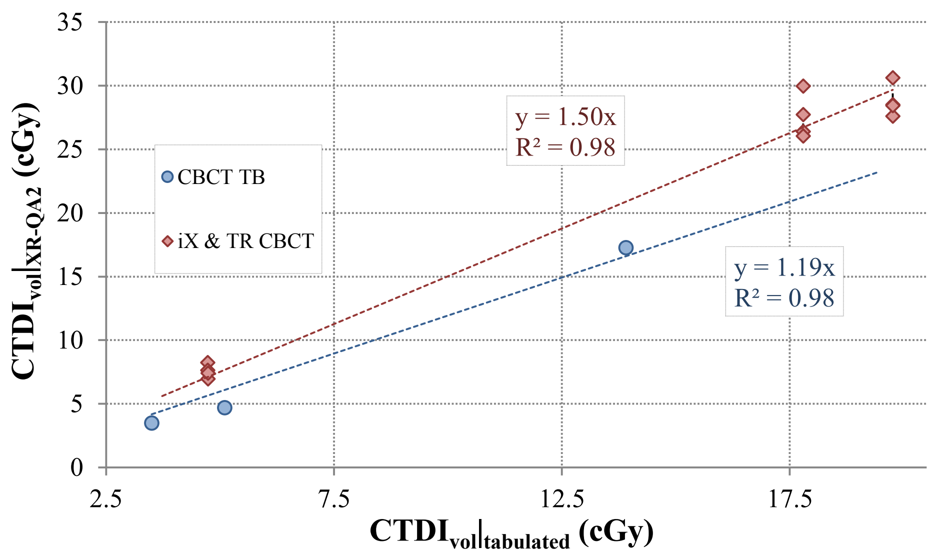

Figure 8.8. Linear correlation between measured and tabulated $CTDI_{vol}$ values on OBI CBCT Systems: TrueBeam® System is shown in blue, and Clinical iX Linear Accelerator & Clinical Trilogy Linear Accelerator in red due to the similarity of the results on the last two devices, these values were grouped into one set.

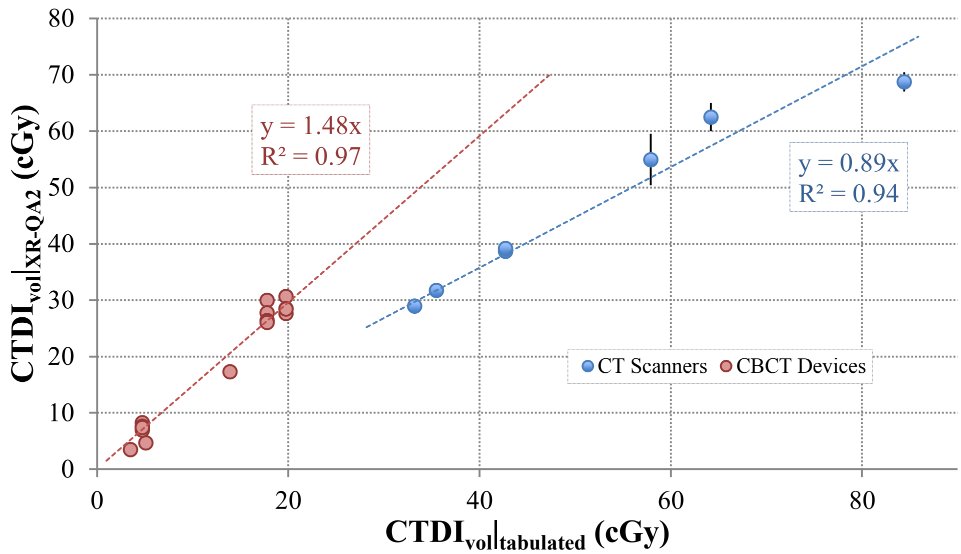

Figure 8.9. Linear correlation between measured and tabulated $CTDI_{vol}$ values on CT Simulators (blue) and OBI CBCT Systems (red).

8.4 Clinical CTDI Measurements Protocol reproducibility

The reproducibility of the Gafchromic® XR-QA2 film-based dosimetry system for CTDI measurements for a particular imaging device and a particular imaging protocol was defined as the relative *SD* on the measured CTDI values:

$$reproducibility(device, imaging\ protocol) = 100\ \% \cdot \frac{SD(CTDI_{vol}|_{XR-QA2})}{average(CTDI_{vol}|_{XR-QA2})}. \qquad [8.1]$$

This value takes into consideration exclusively changes in the film response due to the dosimetry system reproducibility, as the phantom imaging protocols remained constant. The reproducibility of the system was evaluated for the protocols and machines summarized in ***Table 8.5*** and ***Table 8.6.***

Regarding ***Equation 8.1***, the lower *SD* of a set of measurements implies greater reproducibility of the protocol for a particular device and imaging setup. ***Figure 8.9*** presents reproducibility values determined for every imaging protocol studied on CT simulators and CBCT devices. Data in ***Figure 8.9*** are grouped according to the imaging device used, either CT simulators or OBI devices. In general, the reproducibility of the dosimetry method follows a clear trend that decreases with $CTDI_{vol}|_{tabulated}$, except for 1-slice axial scans taken on CT simulators. The 1-slice axial scan is characterized by narrow beam collimation, $1.25 - 5.00$ mm, and it results in high $CTDI_{vol}|_{XR-QA2}$ values that are not fully reproducible. For small beam collimation, the amount of imparted energy to the film varies considerably from one measurement to the next one, and the reproducibility of the protocol varies between 2.4 % and 8.3 %. On the contrary, for multi-axial, helical, and cone beam geometries the protocol reproducibility fluctuates between 0.5 % and 6.1 %. ***Table 8.7*** summarizes the reproducibility results for $CTDI_{vol}|_{XRQA-2}$ measurements per imaging device and imaging protocol geometry.

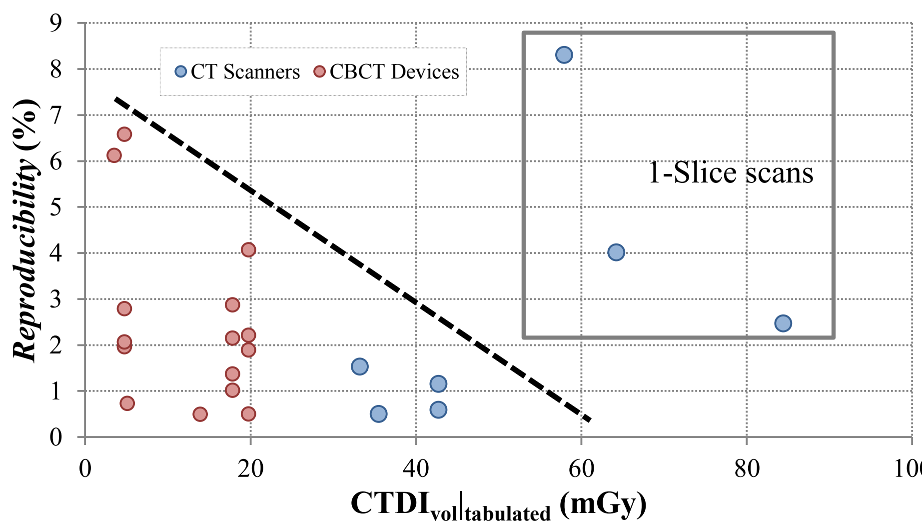

Figure 8.9. CTDI measurements reproducibility for CT Simulators are shown in blue and OBI Systems in red. $CTDI_{vol}|_{XR-QA2}$ values become more reproducible as $CTDI_{vol}|_{tabulated}$ increases, except for 1-slice scans shown in gray.

Imaging device	Imaging protocol geometry	Reproducibility of $CTDI_{vol}\vert_{XR-QA2}$ values (%)
OBI	Cone beam	2.46 ± 1.79
CT Simulators	Axial, 1-slice	4.93 ± 2.49
	Multi-axial	1.66 ± 0.81
	Helical	1.06 ± 0.37

Table 8.7. Gafchromic® XR-QA2 film dosimetry protocol reproducibility.

8.5 Clinical CTDI Measurements Protocol accuracy

The accuracy of the Gafchromic® XR-QA2 film-based dosimetry system for CTDI measurements for a particular imaging device and a particular imaging protocol was defined as

$$accuracy(device, imaging\ protocol) = \frac{average\left(CTDI_{vol}|_{XRQA-2}\right)}{CTDI_{vol}|_{tabulated}}. \qquad [8.2]$$

For a 100 % accurate measurement the ratio equals the unity. ***Figure 8.10*** presents the protocol accuracy report as a function of $CTDI_{vol}|_{tabulated}$. CT simulators, as shown in ***Figure 8.4***, exhibit $CTDI_{vol}|_{XR-QA2}$ close in value to $CTDI_{vol}|_{tabulated}$. On average, the accuracy of the dosimetry protocol for CT simulators was 0.90. The average accuracy of $CTDI_{vol}|_{XRQA-2}$ values on OBI devices was 1.44. The accuracy factors are presented in Table 8.8 for all imaging units studied.

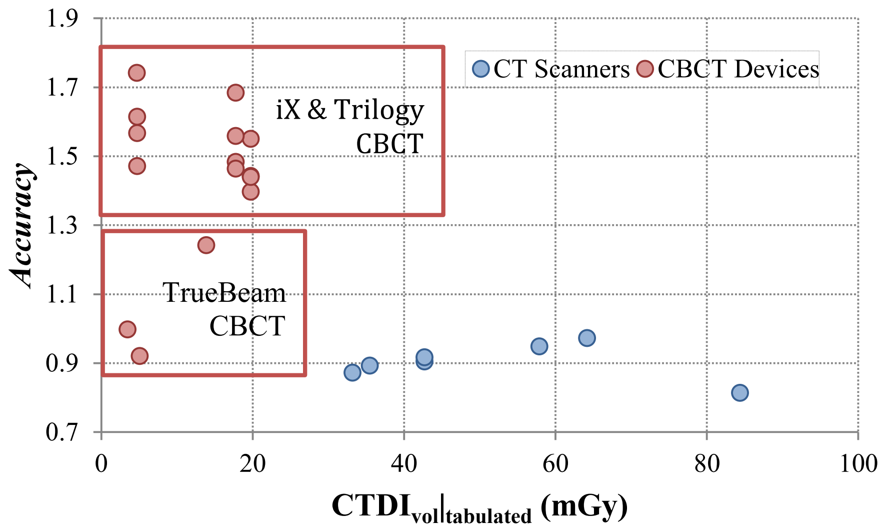

Figure 8.10. CTDI Measurements accuracy for CT Simulators are shown in blue and OBI Systems in red. The gray regions gather measurements for the OBI system coupled to the iX and Trilogy Linear Accelerators (Up), and the TrueBeam System (Down).

Imaging device	Reference	Accuracy of $CTDI_{vol}\|_{XRQA-2}$ values
OBI	iX	1.6 ± 0.1
	TR	1.47 ± 0.05
	TB	1.1 ± 0.1
CT Simulators	GE	0.89 ± 0.07
	Philips	0.91 ± 0.03

Table 8.8. Gafchromic® XR-QA2 film dosimetry protocol reproducibility on CT Simulators and OBI® Systems.

8.6 The influence of scanning parameters on CTDI measurements

Certain scanning parameters were evaluated to assess their effect on the accuracy of the CTDI dosimetry system. This list includes the axial, multi-axial, helical or cone beam geometry, the beam collimation $N \cdot T$ (on CT simulators exclusively), and the length m of the dose profile D_p (as described in ***Section 3.6***) used to calculate $CTDI_{XR-QA2}$ in ***Equation 3.11***. The accuracy and reproducibility of the dosimetry system was reported as a function of the beam geometry used to scan the phantom, ***Figure 8.11***.

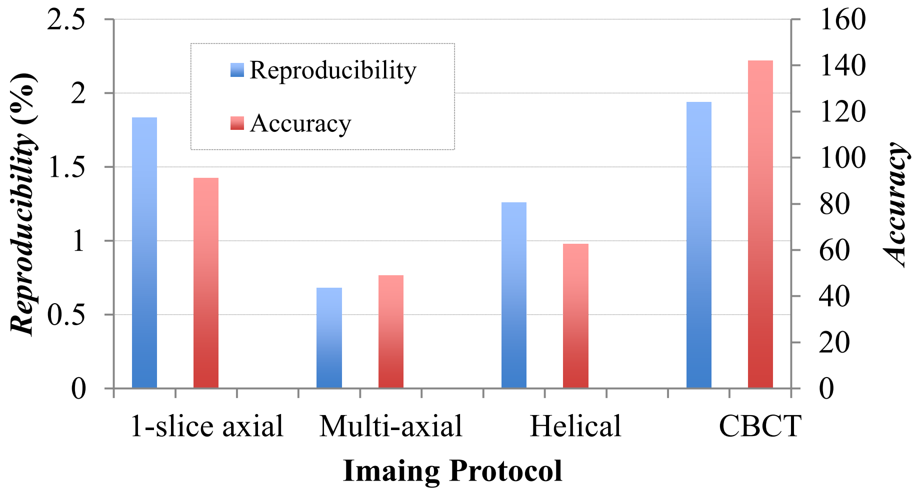

Figure 8.11. Performance of the CTDI measurement protocol. Reproducibility (as defined in Equation 8.1) is shown in blue and accuracy (as defined in Equation 8.2) in red. Bars correspond to average values of scanning protocols of the same acquisition mode, regardless of the imaging device.

8.6.1 Beam collimation

The accuracy and reproducibility of the dosimetry system as a function of the beam collimation $N \cdot T$ (***Equation 3.11***) was also investigated for the CTDI measurements carried out on CT simulators under axial scan protocols. The results are shown in ***Figure 8.12*** and ***Figure***

8.13. Data on $CTDI_{vol}$ for three 1-slice scans with beam collimation ranging from 1.25 to 5.00 mm on CT Simulators, as presented in ***Section 8.1***, was used in this study. ***Figure 8.12*** shows $CTDI_{vol}|_{XRQA-2}$ and $CTDI_{vol}|_{tabulated}$ values as a function of beam collimation. ***Figure 8.13*** presents the reproducibility and accuracy for the measurements, as defined in ***Equation 8.1*** and ***Equation 8.2***, as a function of beam collimation. At very small beam collimations, $N \cdot T =$ 1.25 mm, dose measurements based on radiochromic film are difficult to reproduce. Therefore, the accuracy of the measurement is also compromised. On one side, the geometrical occlusion of the beam due to the collimator increases the intensity of scattered radiation along the central beam. Further, it is known that for small beams, the lack of lateral charged-particle equilibrium (CPE) affects any dose measurement, as it underestimates the actual value of energy deposited in the material per unit of mass. While the beam gets broader the contribution of scattered radiation to the dose profile along the z-direction decreases, and dose measurements become more accurate. At 5 mm collimation, $CTDI_{vol}|_{XRQA-2}$ values show reproducibility of close to 3 % and underestimate $CTDI_{vol}|_{tabulated}$ by less than 3 %.

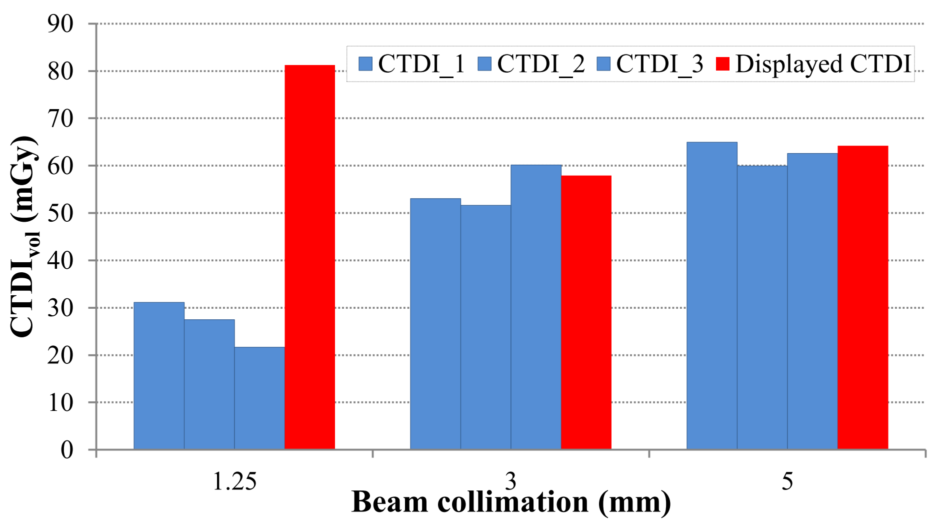

Figure 8.12. $CTDI_{vol}|$ for 1-slice axial scans on CT Simulators as a function of beam collimation. Measured data are shown in blue ($CTDI_{1,2,3}$) and tabulated data in red ($CTDI_d$).

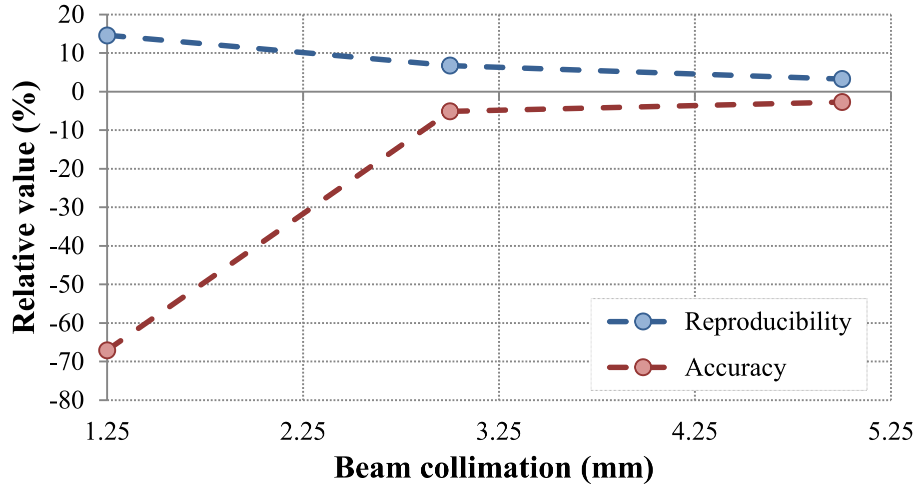

Figure 8.13. Beam collimation effect on the CTDI measurement protocol. *Reproducibility* is shown in blue and *accuracy* in red.

8.6.2 Integration length

The software for film analysis was modified so that the CTDI reported for the same set of films was calculated as a function of the integration length m (***Equation 3.11***). ***Appendix 6*** includes raw data of this test. The calculation of $CTDI_{vol}$ values is based on the $CTDI_{100}$ concept, which is the prevailing parameter used in CT dosimetry. According to its definition (***Equation 1.2***), dose profiles along the z-direction are integrated over a 100 mm-length and normalized with respect to the beam collimation. Ionization chambers used to measure charge within the CTDI phantom are conveniently chosen to be 100 mm long. Nevertheless, the use of radiochromic films allows the measurement of dose profiles extended over the typical 100 mm range; therefore $CTDI_{vol}$ can be evaluated over any integration length smaller than the dimensions of the CTDI phantom (16 cm). Dose profiles acquired for the head 1-slice axial imaging protocol summarized in ***Table 8.9*** were integrated over 14 lengths l, for 10 mm $\leq l \leq$ 140 mm, and associated $CTDI_l$ values are shown in ***Figure 8.14***. As the limits of integration in ***Equation 2.1*** are increased, absorbed dose also increases due to the energy contribution of scattered photons along the tails of the profile. However, this contribution decreases as the integration length separates from the beam collimation value, and the rate at which $CTDI_l$ varies with length $\left(\frac{dCTDI_l}{dl}\right)$ eventually reaches zero, as demonstrated in ***Figure 8.15.***

Machine	**CT GE**	**Date**	**2013-09-28**
	Protocol		Head 1Slice
Protocol parameters	Peak Energy (kVp)		120
	Tube Current (mA)		300
	Exposure time (ms)		1000
	Collimation (cm)		0.5
	Displayed CTDI_100 (mGy)		64.21
Fitting Parameters	Alpha		6.8206
	Beta		-1.7136
	$[\mu_{en}/\rho]_{air\ to\ water}$		1.035

Table 8.9. Imaging protocol settings used during the Integration Length (l) effect test.

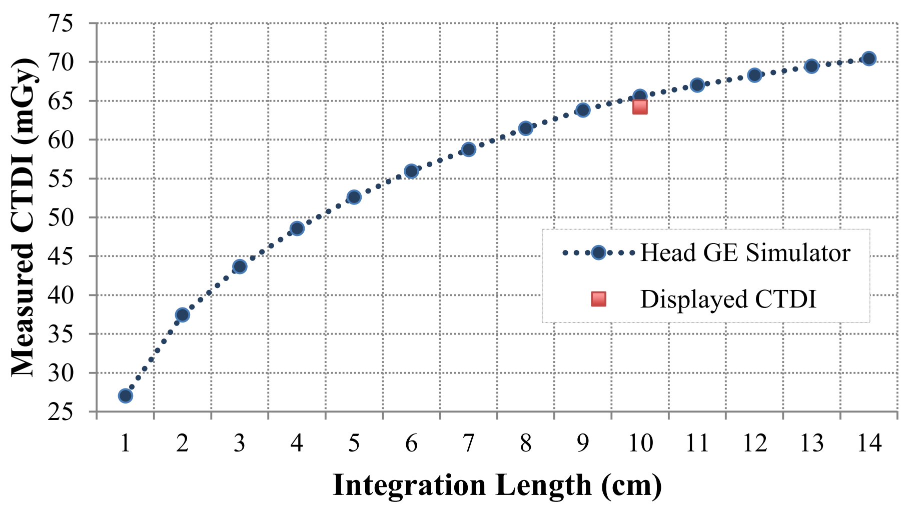

Figure 8.14. Measured $CTDI_l$ values as a function of integral length l are shown in blue. Nominal $CTDI_{100}$ is shown in red.

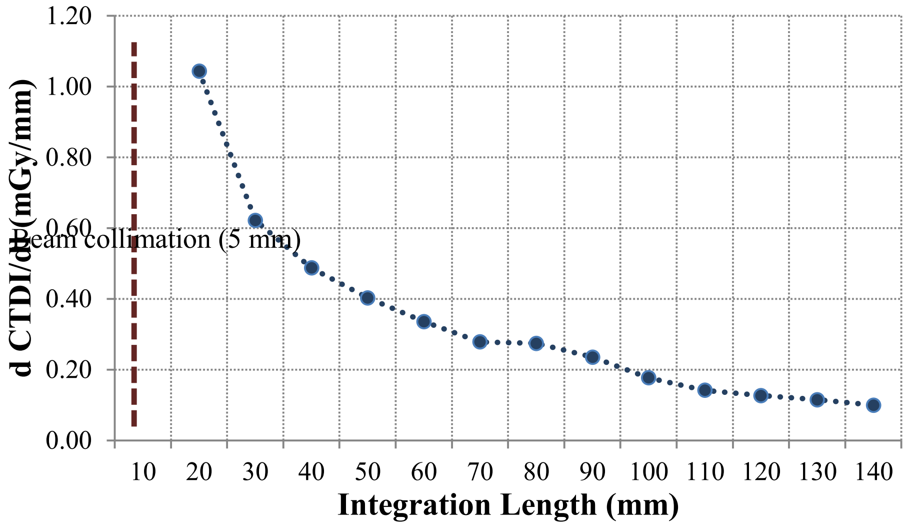

Figure 8.15. Change of CTDI(l) with l. The slope of the curve $CTDI_l$ as a function of l is shown in blue. The beaam collimation ($N \cdot T = 5$ mm) is shown by a dotted red line.

The theoretical $CTDI_l$ value at which $\frac{dCTDI_l}{dl} = 0$ mGy/mm is named *equilibrium dose*, and it is suggested by TG -111 [25] to become a new standard in CT dosimetry. Radiochromic films showed to be a useful 2D dosimeter and could, therefore, be used to measure *equilibrium dose* if used with an appropriate CTDI phantom (sufficiently long to reach the equilibrium length).

Additional dose profiles, acquired under diverse imaging protocols were also integrated over multiple lengths to assess the effect in a more general scope. ***Figure 8.16*** is a plot of $CTDI_l$ against integration length l for multi-axial and helical scans delivered by the SpeedLight® CT Simulator, and ***Figure 8.18*** is the equivalent for CBCT scans acquired by the OBI device coupled to the Clinical iX Linear Accelerator. For multi-axial and helical scans, $CTDI_l$ exhibited a weak dependence on the integration length, as their value remained almost constant over the studied range: the maximum relative variation $(6.1\ \%)$ was observed for the head multiaxial scan delivered by the LightSpeed® CT Simulator (Head Multiaxial - GE 2, In ***Figure 8.16***). The rest of protocols averaged a variation of 3.4 % (range 3.3 % to 3.2 %). Regarding the CBCT scans, a particular dependence was observed: $CTDI_l$ always diminishes, but as integration length l increases (from 10 mm up to 30 $mm \pm 10\ mm$ depending on the imaging protocol), the rate at which $CTDI_l$ also decreases slightly with l. After the length approximately of 30 mm, the $\frac{dCTDI_l}{dl}$ value decreases uniformly, as seen in ***Figure 8.18.***

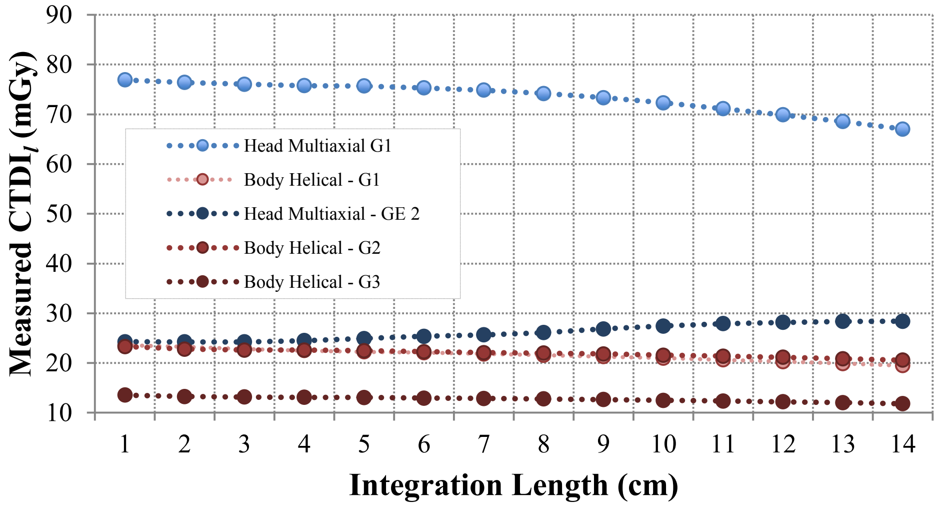

Figure 8.16. Measured $CTDI_l$ values as a function of integral length l are shown in blue for five imaging protocols delivered by the LightSpeed® CT Simulator.

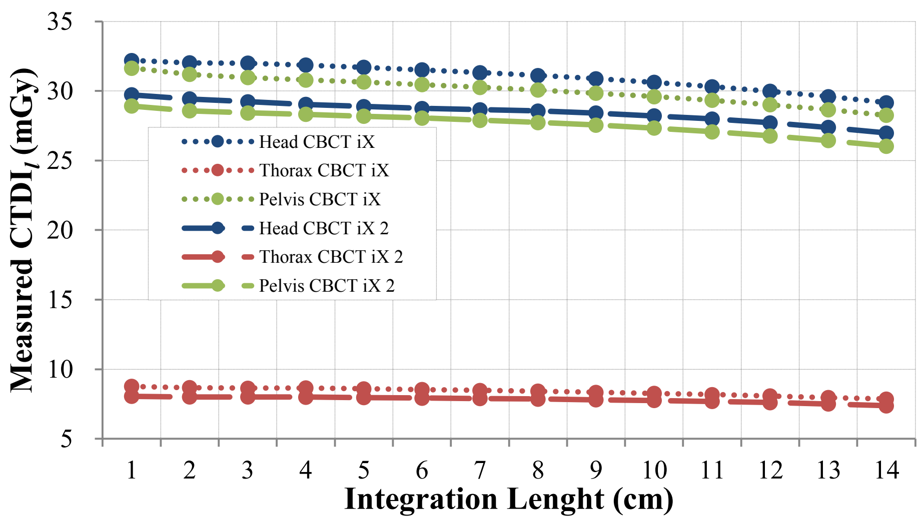

Figure 8.17 Measured $CTDI_l$ values as a function of integral length l are shown in blue for six imaging protocols delivered by the kV CBCT imaging system coupled to the Clinical iX Linear Accelerator.

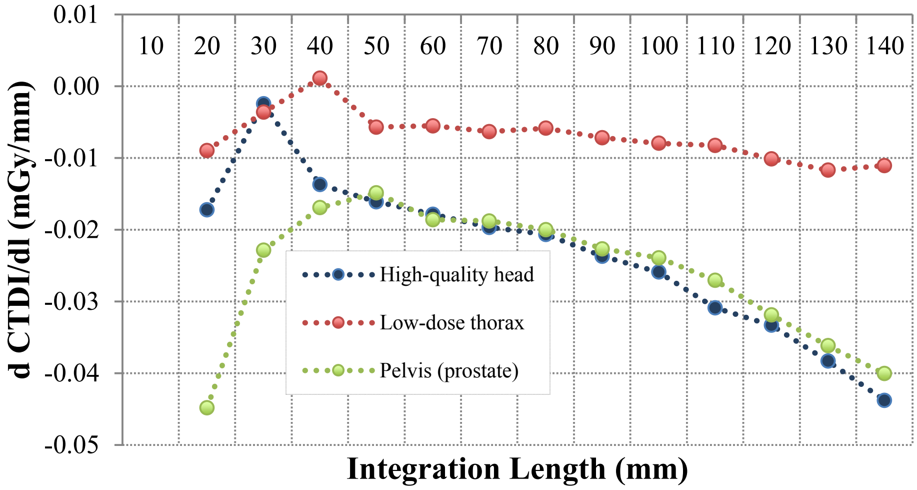

Figure 8.18. Change of CTDI(l) with l for measurements on the OBI system coupled to the Clinical iX Linear Accelerator. Three imaging protocols are shown for head and body phantom measurements.

8.7 The impact of phantom misalignment

The impact of phantom misalignment was assessed by scanning the CTDI phantom according to the CTDI irradiation protocol, first with its central axis parallel to the $z-$ axis of the General Electric LightSpeed® CT Simulator and crossing its isocenter. Another CTDI measurement was taken with the phantom central axis aligned to the $z-$ axis of the imaging system, but with a offset of the isocenter in the x direction. The accuracy of the measurements was compared to previous well-aligned phantom measurements to establish the effect of phantom misalignments on the performance of the dosimetry system. The film protocol for CTDI measurement was followed for the imaging setup summarized in ***Table 8.10***. Dose values obtained for each phantom measurment hole and measured $CTDI_{vol}$ were then comparated to assess the effect of slight phantom misaligments on the dosimetry protocol acccuracy (***Figure 8.19***). A 20 mm misalignment of the phantom conducted to an overestimation of $CTDI_{vol}|_{XRQA-2}$ of 0.48 mGy. This difference (0.27 %) is smaller than the reproducibility of the CTDI protocol for $CTDI_{vol}$ measurements on

CT Simulators reported in ***Section 8.4***, ***Figure 8.9*** (~1.0 %). As a result of the test, small phantom misalignments ($< 20\ mm$) do not have a significant impact on the accuracy of $CTDI_{vol}|_{XRQA-2}$.

	Machine	CT GE
	Date	2013-09-28
		Protocol Head 1Slice
Protocol parameters	Peak Energy (kVp)	120
	Tube Current (mA)	300
	Exposure time (ms)	1000
	Beam collimation (mm)	5
	Pitch	-
	Displayed CTDI (mGy)	64.21
Fitting Parameters	Alpha	6.8206
	Beta	-1.7136
$[\mu_{en}/\rho]_{air\ to\ water}$		1.035

Table 8.10. Scanning protocol used to assess the impact of the phantom misalignment on the CTDI measurement protocol.

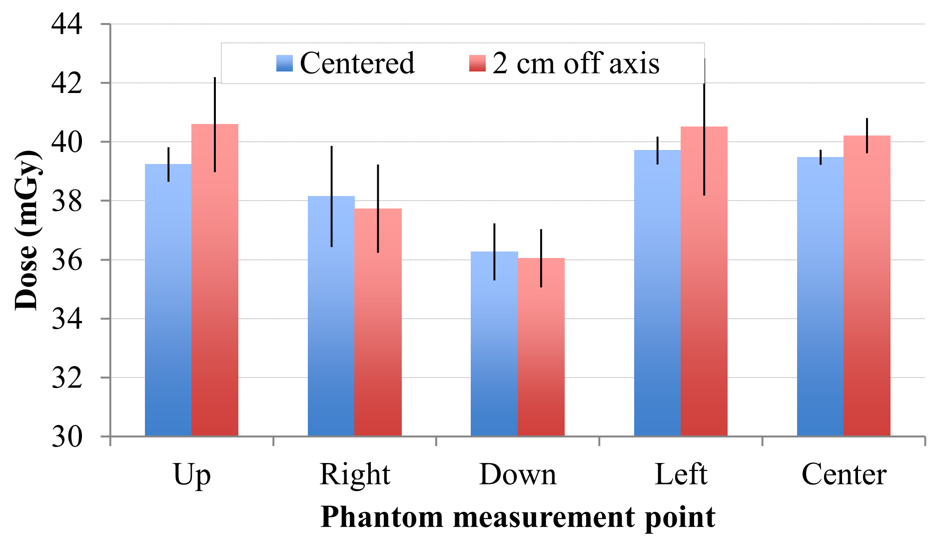

Figure 8.19. Measurements of dose to the CTDI phantom for phantom misalignment assessment. Dose is shown in function of the in phantom measurement point. Dose measured with the phantom well-centered respect to the $x - axis$ of the LightSpeed® CT Simulator is shown in blue, and dose with the phantom 2 cm off of the $x - axis$ is shown in red.

9. Conclusions

A series of tests were carried out to assess the reproducibility and accuracy of a Gafchromic® XR-QA2 radiochromic film-based dosimetry protocol for CTDI clinical measurements on CT simulators and kV CBCT devices coupled to linear accelerators. The protocol for CTDI clinical measurements consisted of 6 concatenated steps, starting from the irradiation of Gafchromic® XR-QA2 film strips placed in a PMMA phantom for CTDI measurements, until the report of dose to water values and CTDI values associated to the imaging protocol used to scan the films. An in-house written Matlab script was used to read out images of the irradiated films and create calibration curves, dose maps, dose profiles, and calculate dosimetric magnitudes out of them. Additionally, the response in the reflectance of the film to ionizing radiation was also tested as a function of the effective energy of the beam (E_{eff}) in the imaging energy range of 38.8 keV $\leq E_{eff} \leq 64.0$ keV, and the effect of the orientation of the film respect to the radiation source on the dose absorbed by the film's active layer was also evaluated.

The response of the film (*reflectance*, R) in a particular *ROI* was defined in terms of the change in the mean pixel value $\left(\frac{\overline{PV}}{2^{16}}\right)$ read-out within this region before and after the irradiation of the film. The effect of the *ROI* size on the *SD* of the *PV* during the calibration films read-out process, and consequently on the total uncertainty of the calibration curve was evaluated. Since the experimental and fitting uncertainties are added in quadrature to obtain the total uncertainty, its behavior is strongly dependent on each component, and similarly to the experimental uncertainty, its value increases with the *ROI* size. At very small *ROI* sizes (~ 64 pixel^2) inconsistences in the fitting uncertainty were observed, so in order to obtain the smallest total uncertainty possible (2.7 %) during the calibration process, the *ROI* was set at 100 pixel^2. At this size of *ROI*, the experimental error was small enough (1.4 %), and the fitting error was acceptable (2.3 %). The effect of the *ROI* geometry on the total uncertainty was neglected due to the small difference observed in the mean *PV* and its standard deviation (0.13%) when the shape of the *ROI* was modified. According to the tests, there are no considerable differences in the total uncertainty of the calibration curves created with different *ROI* geometries. Total uncertainties became nearly identical over the tested $[K_{air}]_{air}$ range with a negligible average difference of 0.13 %. For simplicity, a squared-shaped *ROI* was adopted in this study.

The red channel of *TIFF* images produced from the irradiated films was used to describe the response of the film to ionizing radiation, as it demonstrated to provide the highest signal to noise ratio (*SNR*) across the whole E_{eff} range in comparison with the green and blue channels ($\overline{SNR}_{red} = 2.5$, $\overline{SNR}_{green} = 1.6$, $\overline{SNR}_{blue} = 0.25$). Additionally, at the low $[K_{air}]_{air}$ values used in this study (< 100 mGy), the active layer of the film doesn't show signals of saturation in the red channel.

The AAPM Report TG-61 on kilo-voltage dosimetry [28] was followed to measure air-kerma free in air $[k_{air}]_{air}$ based on the N_k concept. The attenuation of beams delivered by the LightSpeed® CT Simulator and Xstrahl 300 unit was evaluated to calculate *HVL* values in the range $4.0 - 7.3$ mmAl and linear attenuation coefficients μ in the range $0.172 - 1.27\ \text{cm}^{-1}$. This information was used to interpolate N_k values from data provided by the National Research Council of Canada [43].

A series of calibration curves were elaborated to model the Gafchromic® XR-QA2 film response to radiation in the $[k_{air}]_{air}$ range covering nominal CTDI values delivered by CT scanners and CBCT devices during common imaging protocols, *i.e.* $5\ \text{mGy} \leq [k_{air}]_{air} \leq 100\ \text{mGy}$. Calibration curves were created for multiple E_{eff} within the range covering the operational beam qualities generally used by imaging systems in radiology and radiotherapy procedures, *i.e.* $38.8\ \text{keV} \leq E_{eff} \leq 64.0\ \text{keV}$. The response of the film was modeled by a bi-parametric (α, β) fitting function that correlates the change in the reflectance of the film (ΔR_{net}) to $[K_{air}]_{air}$ values used to expose the film $(\Delta R_{net} = \alpha[K_{air}]_{air}/(1 + \beta[K_{air}]_{air}))$. This model showed to provide the lowest fitting uncertainties among a set of predetermined fitting models $f_i(\alpha, \beta)$, and was used consistently to produce calibration curves in the E_{eff} range of beams between 12.7 and 64 keV. In this broad range, uncertainties in the fitting parameters varied from 1 to 1.6%, while in the clinical imaging energy range of 38.8 – 56.4 keV, uncertainties from 0.7 to 1.6 % were observed.

The response of the film was tested for two orientations ("UP" corresponding to the film active layer facing the static x-ray tube of the LightSpeed® CT Simulator, and "DOWN" the opaque layer facing the x-ray tube). The maximum difference in the film orientation was registered in air at medium energies (~2.2 %), while differences for measurements on the surface and inside the phantom where minimal regardless of the energy (< 1.3 %). This difference was lower than the total uncertainty in ΔR_{net} reported for every studied E_{eff}, which supposes that the film orientation dependence for static radiation sources can be neglected for in-phantom measurements. No significant differences were observed between the film responses when the film's active layer was placed in three different orientations inside a head and body PMMA phantom and irradiated by a rotating x-ray tube. A slightly larger change in the reflectance of the film (~2 %) was seen when the active layer faced the x-ray tube with the head phantom. On the other hand, when the body phantom was used, a higher change in the reflectance of the film (~1 %) was observed if its opaque layer is facing the x-ray tube. In general, for both the head and body phantom, the uncertainty associated with the orientation of the film was smaller than the uncertainty in the measurement of the reflectance change individually for each orientation.

The Xstrahl 300 unit was used to broaden the photon beam energy available on the LightSpeed® CT Simulator. The absorbed-dose – energy dependence of the Gafchromic® XR-QA2 film was tested over the beam quality range 0.16 mmAl – 3.00 mmCu, which extends the beam qualities used generally in radiography and radiotherapy imaging procedures (clinical range). The response of the film ΔR_{net} can be described for the clinical imaging rage, and for $[K_{air}]_{air}$ values below 100 mGy by a simplified 1-parametric fitting function $\left(\Delta R_{net} = \frac{\alpha[K_{air}]_{air}}{1-1.744[K_{air}]_{air}}\right)$. Moreover, the clinical use of a radiochromic film-based CTDI protocol may result in 15 % systematic error in dose measurements if a single calibration curve is used ($\bar{\alpha} = 6.464 \pm 0.774$). Outside of the imaging effective range, the response of the film is strongly dependent on the beam quality. In general, due to the shown dependence of fitting parameters on effective energy (E_{eff}), the response of the film can be described by a parameterized model $\left(\Delta R_{net} = \frac{(0.1382\, E_{eff}-0.0215)K_{air}}{1+(0.0054\, E_{eff}-1.9973)K_{air}}\right)$.

Average relative variation of 5.2 % in the mean reflectance change of the Gafchromic® XR-QA2 film was observed over the beam quality range used in diagnostic radiology ($38.8 - 64\ keV$).

The relative variation of the film was determined to be inversely proportional to the absorbed dose. The film response variation declines from a maximum of 11.1 % at 5 mGy to 2.8 % at 100 mGy. By extending the beam quality range down to 12.7 keV, the observed mean variation of the film response was 14.5 %, declining from 22.7 % to 11.1 % within the same dose limits. The maximum absolute variation of the film response was observed at 30 mGy over the studied E_{eff} range. The observed variation diminishes up to 50 % as dose decreases to 5 mGy, and up to 75 % as dose increases to 100 mGy.

The *SD* in multiple $CTDI_{vol}$ measurements for the same imaging protocol ($CTDI_{vol}|_{XR-QA2}$) was used to assess the reproducibility of the dosimetry system, while measured to tabulated $CTDI_{\mathrm{vol}}$ values ratios $\left(\frac{CTDI_{vol}|_{XR-QA2}}{CTDI_{vol}|_{tabulated}}\right)$ were used to evaluate the accuracy of the protocol. $CTDI_{vol}|_{tabulated}$ values were recorded for 12 scanning protocols on two CT simulators and three *OBI* systems coupled to linear accelerators. These values ranged from 3 mGy up to 87 mGy. $CTDI_{vol}|_{XR-QA2}$ values for CT simulator were constantly lower than $CTDI_{vol}|_{tabulated}$. $CTDI_{vol}|_{XR-QA2}$ for 1-slice axial scans were on average 3.6 % lower than $CTDI_{vol}|_{tabulated}$, multi-axial scans were 10.3 % lower, and helical scans were 29.1 % lower. On the other hand, $CTDI_{vol}|_{XR-QA2}$ values for kV CBCT devices were considerable higher than $CTDI_{vol}|_{tabulated}$. Similar differences between these values were found for the *OBI* system coupled to the Trilogy Linear Accelerator and the Clinical iX Linear Accelerator (41.9 % higher for head scans, 52.2 % for thorax scans, and 41.8 % for pelvis scans). The difference between measured and tabulated data on the TrueBeam® System was the smallest among the three systems (7.9 % lower for head scans, 0.12 % lower than thorax scans, and 24.3 % higher than pelvis scans). In general, the uncertainty in the measurement was independent of the device used to irradiate the films, and it was on average 2.4 % for head scans and 2.8 % for body scans.

In terms of reproducibility of the dosimetry protocol, $CTDI_{vol}|_{XR-QA2}$ values presented a mean variation for a given scanning protocol of 2.7 % for CT simulators and 2.5 % for CBCT devices. It was observed that $CTDI_{vol}|_{XR-QA2}$ values become more reproducible as the corresponding $CTDI_{vol}|_{tabulated}$ increases (7 % at 5 mGy up to 1% at 40 mGy). 1-slice axial scans did not show this trend, and the reproducibility of the protocol for this kind of scans was the higher among the universe of scans (8 % at 60 mGy). A linear correlation was found for CT-simulators and CBCT devices with acceptable correlation factors ($R^2_{CT-Simulator} = 0.94$ and $R^2_{CBCT} = 0.97$). Measured $CTDI_{\mathrm{vol}}$ values were on average 10 % lower than tabulated $CTDI_{\mathrm{vol}}$ values for CT-simulators, and 44% higher for CBCT devices.

Film dosimetry using Gafchromic® XR-QA2 film proved to be reproducible regardless of the protocol or device used to irradiate the set of films, but its clinical use may result in 15% systematic error in dose measurements if a single calibration curve is used. It was also found relatively large discrepancies between measured and tabulated $CTDI_{\mathrm{vol}}$ values for various protocols and imaging systems used within the radiotherapy department. The findings strongly support the trend towards replacing the CTDI value with measurement of *equilibrium dose* in the center of a cylindrical phantom as suggested by TG-111. Radiochromic films showed to be a useful and low-cost 2D dosimeter and could, therefore, be used to measure *equilibrium dose* if used with an appropriate CTDI phantom.

References

1. Goldman, L.W. (2007). Principles of CT and CT Technology. *Journal of Nuclear Medicine Technology*, 35, 115 – 128. doi: 10.2967/jnmt.107.042978
2. Bushberg, J., Seibert, J., Leidholt, E., & Boone, Jr.J. (2012). *The Essential Physics of Medical Imaging*, third edition. Wolters Kluwer, Lippincott Williams & Wilkins
3. Bocage, A. (1921). Procédé et dispositifs de radiographie sur plaque en movement. French patent 536-464.
4. Hounsfield, G.N. (1976). Historical notes on computerized axial tomography. *Journal of the Canadian Association of Radiologists*, 27(3), 135 – 142. PMID: 789383
5. Bull, J. (1981). History of Computed Tomography. Introduction: Newton, T. & Potts, D. editors *Technical Aspects of Computed Tomography*. St Louis, MO: CV Mosby Co. 3835 – 3849.
6. McCollough, C, Cody, D., Edyvean, S., Geise, R., Gould, B., Keat, N., Huda, W., Judy, P., Kalender, W., McNitt-Gray, M., Morin, R., Payne, T., Stern, S., & Rothenberg, L. (2008). *Report of AAPM task Group No. 23: CT Dosimetry. The Measurement, Reporting, and Management of Radiation Dose in CT*. AAPM
7. Keneth, R.K. (2009) *NCRP Report No. 160: Ionizing radiation exposure of the population of the United States*. Bethesda: National Council on Radiation Protection and Measurements.
8. Brenner, D. (2008) *Minimizing Medically Unwarranted CT scans*. Columbia University Medical Center
9. Siedband, M., Baiter, S., Brateman, L., Britt, W., Deutsch, G., Dobrin R., Duerkes, R., Fields, T., Laurence, D., Lin, P., Morgan T., Properzio, W., Rossi, R., Rothenberg, L., Scheid, C., Starchman, D., Vucich, J., Waggener, R., & Winkler, N. (1978) *AAPM Report No 4: Basic Quality Control in Diagnostic Radiology*. New York: AAPM
10. Shepard, S., Lin, P., Boone, J., Cody, D., Fisher, J., Frey, G., Glasser, H., Gray, J., Haus, A., Hefner, L., Holmes, R., Nobistek, R., Ranallo, F., Rauch, P., Rossi, R., Seibert, J., Strauss, K., Suleiman, O., Schnek, J., & Thompson, S. (2002) *AAPM Report No. 74: Quality Control in Diagnostic Radiology*, New York: AAPM

11. Mutic, S., Palta, J., Butker, E., Das, I., Saiful, M., Dick, L., Salter, B., McCollough, C., & Van Dik, J. (2003) *AAPM Report No 66: Quality assurance for computed-tomography simulators and computed-tomography simulation process*. New York: AAPM
12. Murphy, M., Balter, J., Balter, S., BenComo, J., Das, I., Jiang, S., Ma, C., Olivera, G., Fodebaugh, R., Ruchala, K., Shirato, H., & Yin, F. (2007) The management of imaging dose during image-guided radiotherapy: Report of the AAPM Task Group No. 75. *Med. Phys*. 34(10), 4041 – 4063. Doi: 10.1118/1.2775667
13. Bongartz, G., Golding, S.J., Jurik, A.G., Leonardi, M., & Van Meerten, E.v.P. (1999) *European Guidelines On Quality Criteria for Computed Tomography*. European Commission's Radiation Protections Actions, 16252.
14. World Health Organization (1982) *Quality Assurance in Diagnostic Radiology*. Geneva: WHO.
15. International Atomic Energy Agency (2012). *Quality Assurance Programme for Computed Tomography: Diagnostic and therapy Applications.* Vienna: IAEA.
16. Wagner, L., Eifel, P., & Geise, R. (1994) Potential biological effects following high x-ray dose interventional procedures. *J. Vasc. Interv. Radiol*. 5(1), 71 – 81 PMID: 8136601
17. Lee, C.I., Haims, A.H., Monico, E.P., Brink, J.A., & Forman, H.P. (2004) Diagnostic CT scans: Assessment of patient, physician, and radiologist awareness of radiation dose and possible risks. *Radiology* 231(2), 393 – 398. PMID: 15031431
18. Hall, E.J., & Brenner, D.J. (2008) Cancer risks from diagnostic radiology. *Br. J. Radiol*. 81(965), 362 – 378. PMID: 18440940
19. International Atomic Energy Agency (2007). *Technical Reports Series No 457: Dosimetry in Diagnostic Radiology: An International Code of Practice*. Vienna: IAEA
20. Goldman, L. (2007). Principles of CT: Radiation Dose and Image Quality. *J Nucl Med Technol*, 35(4), 115 – 128. PMID: 18006597
21. International Commission on Radiation Units and Measurements (1971). *Report Committee No. 19 on Radiation Dose and Image Quality Assessment in Computed Tomography*. Bethesda: ICRU
22. Judy, P., Balter, S., Bassano, D., McCullough, E., Payne, J., & Rothenberg, L. (1977). *AAPM Report No 1: Phantoms for Performance Evaluation and Quality Assurance of CT scanners*. New York: AAPM

23. Shope, T.B., Gagne, R.M., & Johnson, G.C. (1981). A method for describing the dose delivered by transmission x-ray computed tomography. *Med. Phys*. 8(4), 488 – 495. PMID: 7322067
24. Boone J.M. (2007). The Trouble with CTDI 100. *Med. Phys.* 34(4), 1364 – 1371. Doi: 10.1118/1.2713240
25. Dixon, R., Anderson, J., Bakalyar, D., Boedeker, K., Boone, J., Cody, D., Fahrig, R., Jaffray, D., Kyprianou, I., McCollough, C., McNitt-Gray, M., Morgan, H., Morin, R., Nakonechny, K., Payne, & T., Pizzutiello. R. (2010) Report of the AAPM Task Group No 111: Comprehensive Methodology for the Evaluation of Radiation Dose in X-Ray Computed Tomography. New York: AAPM.
26. Dixon, R.L., & Ekstrand, K.E. (1978). A film dosimetry system for use in computed tomography. *Radiology* 127(1), 255–258. PMID: 635194
27. Tomic, N., Devic, S., DeBlois, J., & Seuntjens,, J. (2010). Reference radiochromic film dosimetry in kilo-voltage photon beams during CTBT image acquisition. *Med. Phys.* 37(3): 1083 – 1092. Doi: 10.1118/1.3302140
28. Ma, C., Coffey, C., DeWerd, L., Liu, C., Nath, R., Seltzer, S., & Seuntjens. J. (2001). TG-61: AAPM protocol for 40 – 300 kV x-ray beam dosimetry in radiotherapy and radiobiology. *Med. Phys*. 28, 868 – 893. Doi: 10.1118/1.1374247
29. Boivin, J., Tomic, N., Fadlallah, B., DeBlois, F., & Devic, S. (2011). Reference dosimetry during diagnostic CT examinations using XRQA radiochromic film model. *Med. Phys.* 38(9), 5119 – 5129. Doi: 10.1118/1.3622607
30. Coursey, C. &Frush, D. (2008). CT and Radiation: What Radiologists Should Know. *Applied Radiology*, 37(3), 22-29. Retrieved from http://www.appliedradiology.com
31. Rampado, O., Garelli, E., & Ropolo. R. (2010). Computed tomography dose measurements with radiochromic films and a flatbed scan. *Med. Phys.* 37(1), 189 – 196. Doi: 10.1118/1.3271584
32. Lewis, D.F. (2010). *Radiochromic Film*. Retrieved from Ashland.com
33. Shani, G. (2000). *Radiation Dosimetry Instrumentation and Methods*. Florida: CRC Press
34. Keyleth Instruments, Inc. (1996). *Model 6517a Electrometer User's Manual*. Cleveland: Keyleth.
35. Xstrahl Limited (2009). Xstrahl 200 & 300. Camberley: Xstrahl

36. Purchasing and Supply Agency (2005). *Report 05070: GE LightSpeed RT CT scanner. Technical evaluation*. London: NHS PASA
37. Philips Healthcare (2011). *Philips Brilliance CT Big Bore oncology specifications*. Netherlands: Koninklijke Philips Electronics
38. Varian Medical Systems (2012). *The TrueBeam System*. Palo Alto: Varian
39. Desroches, J., Bouchard, H., & Lacroix, F. (2010). Technical note: Potential errors in optical density measurements due to scanning side in EBT and EBT2 Gafchromic film dosimetry, *Med. Phys*. 37, 1565. Doi: 10.1118/1.3355895
40. Micke, A., Lewis, D.F. & Yu, X. (2011). Multichannel film dosimetry with nonuniformity correction. *Med. Phys.* 38(5), 2523 – 2534. Doi: 10.1118/1.3576105
41. Hubbell, J.H. & Seltzer, S.M. (1996). NISTR 5632: Tables of X-Ray Mass Attenuation Coefficients and Mass Energy-Absorption Coefficients from 1 keV to 20 MeV for Elements Z=1 to 92 and 48 Additional Substances of Dosimetric Interest. Radiation Physics Division. Retrieved from http://www.nist.gov
42. Miller, D., Bloch, P., Cunningham, J., Curran, B., Ibbott, G., Jones, D., Jucius, S., Leavitt, D., Mohan, R., & Van de Geijn, J. (1995). *AAPM report No. 55: Radiation Treatment Planning Dosimetry Verification.* New York: American Institute of Physics.
43. National Research Council. "NRC Report Number: IRS-2010-1350Medium-Energy X-ray (Nk, Nx) Calibration Report".
44. Niroomand-Rad, A., Blackwell, C., Coursey, B., Gall, K., Galvin, J., McLaughlin, W., Meigooni, A., Nath, R., Rodgers, J., & Soares, C. (1998). Radiochromic Film Dosimetry: Recommendations of AAPM Radiation Therapy Committee Task Group No. 55. *Med. Phys.*15, 2093. Doi: 10.1118/1.598407
45. Boone, J., Strauss, K., Cody, D., McCollough, C., McNitt-Gray, M., & Loth, J. (2013). *Report of AAPM Task group 204: Size-Specific Dose Estimates (SSDE) in Pediatric and Adultn Body CT Examinations*. College Park: AAPM.
46. Bissonette, J., Balter, P., Dong, L., Langen, K., Loveloch, D., Miften, M., Moseley, D., Pouliot, J., Sonke, J., & Yoo, S. (2012). Quality Assurance for image-guided radiation therapy utilizing CT-based technologies: A report of the AAPM TG-179, *Med. Phys.* 39, 1946 – 1963. Doi: 10.1118/1.3690466

47. United Nations Scientific Committee on the Effects of Atomic Radiation (2000). *Sources and Effects of Ionizing Radiation*. New York: United Nations.
48. International Electrotechnical Commission (2009). *Particular Requirements for the Safety of X-Ray Equipment for Computed Tomography*. Geneva: IEC
49. Leitz, W., Axelsson, B., & Szendro, G. (1995). Computed Tomography Dose Assessment: A Apractical Approach. *Radiation Protection Dosimetry* 57(1-4), 377 – 380. Retrieved from http://rpd.oxfordjournals.org
50. Dixon, R.L. (2003). A new look at CT dose measurements: Beyond CTDI. *Med. Phys.* 30, 1272. Doi: 10.1118/1.1576952
51. Butson, M., Cheung, T., & Yu, P. (2006). Measurement of energy dependence for XRCT radiochromic film, *Med. Phys.* 33, 2923. Doi: 10.1118/1.2219330
52. Dawson, L., & Sharpe, M. (2006). Image-guided radiotherapy: rationale, benefits, and limitation. *The Lancet Oncology* 7(10), 848-858. Doi: 10.1016/S1470-2045(06)70904-4
53. Verellen, D., De Ridder, M., Tournel, K., Duchateau, M., Reynders, T., Gevaert, T., Linthout, N., & Storme, G. (2008). An overview of volumetric imaging technologies and their quality assurance for IGRT. *Acta Oncologica* 47(7), 1271-1278. Doi: 10.1080/02841860802244182
54. Subhalaxmi, M., & Selvam, T.P. (2014). Monte Carlo-based investigation of absorbed-dose energy dependence of radiochromic films in high-energy brachytherapy dosimetry. *J. Appl. Clin. Med. Phys*. 15(1), 4448. Doi: 10.1120/jacmp.v15i1.4448.
55. Das, I.J., Ding, G.X., & Ahnesjo, A. (2008). Small fields: nonequilibrium radiation dosimetry. *Med. Phys.* 35, 206 – 215. Doi: 10.1118/1.2815356
56. Lewis, D.F. (2010). *Radiochromic Film.* Ashland.
57. Hill, R., Healy, B., Holloway, L., Kuncic, Z., Thwaites, D., & Baldock, C (2014). Advances in kilovoltage x-ray dosimetry. *Physics in Medicine and Biology,* 59(6), R183 – R231. doi: 10.1088/0031-9155/59/6/R183.

Appendices

Appendix 1: Raw and processed data from HVL measurement

Date:	2013-09-07	Scanner:	GE CT Simulator
Peak Energy (kVp)	80	Filter	Air

Thickness (mm Al)	Electrometer reading (nC)				Relative intensity
	1	2	3	Average	
0	0.253	0.254	0.254	0.254	1.000
0.5	0.229	0.230	0.229	0.229	0.904
1	0.207	0.208	0.209	0.208	0.820
1.5	0.19	0.191	0.191	0.191	0.752
2	0.175	0.176	0.176	0.176	0.693
2.5	0.161	0.162	0.162	0.162	0.637
3	0.149	0.150	0.15	0.150	0.590
3.5	0.139	0.139	0.139	0.139	0.547
4	0.131	0.130	0.130	0.130	0.514
4.5	0.121	0.122	0.121	0.121	0.477

Exponential fitting model for the beam attenuation

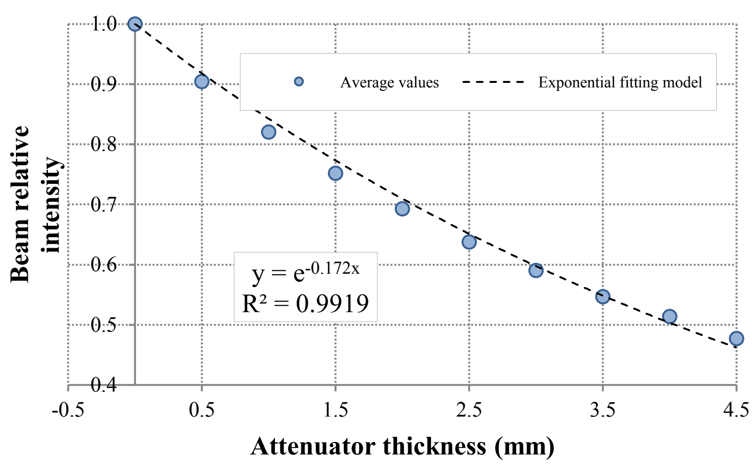

Attenuation coefficient (mm-1)	R^2	*HVL* (mm Al)
0.172	0.99	4.03

Table i. The table is an example of the format used to register raw and processed data during *HVL* measurement in the General Electric LightSpeed® CT Simulator.

Appendix 2: Processed data from effective energy (E_{eff}) measurement

Date:		2013-09-07		Scanner:	GE CT Simulator
Peak Energy (kVp)		80		Filter	Air
Attenuator	Density (g/cm^3)	HVL (mm)	Attenuation coefficient (cm^{-1})	Mass attenuation coefficient (cm^2/g)	Effective energy (kVp)
Aluminum (Al)	2.699	4.03	1.72	0.637	38.8

Table ii The table is an example of the format used to register processed data during E_{eff} measurement in the General Electric LightSpeed® CT Simulator.

Appendix 3: Processed data from radiation sources output measurements

Date:	2013-09-07			Scanner:	GE
Nominal Energy (kVp)	80			Filter	Air
PRESSURE-TEMPERATURE				Nominal HVL (mm Al)	4.03
P (Torr)	747.0			Nominal Energy (kVp)	80
T (^{o}C)	22.0			Filter no.	Air
P_{TP}	1.017			Reading #1	0.5649
C_{SSD}	1.0000			Reading #2	0.5645
EQUIPMENT				Reading #3	0.5656
Chamber	2577c			Reading #4	0.5650
s/n	282			P_{ion}	1.0008
Electrometer	6517a			P_{pol}	0.9973
s/n	914864			Average reading	0.5650
CORRECTION FACTORS				Cssd	1.0000
Voltage (V)	+ 300	+ 150	- 300	Corrected (P, T) reading	0.5737
Measurements	Collected charge (nC)			mAs	600
1	0.5649	0.5636	0.5680	Dose ratio-app BSF	1.000
2	0.5645	0.5638	0.5679	Nk (cGy/nC) - From step 2	12.535
3	0.5656	0.5636	0.5684	BSF	1.000
4	0.5650	0.5637	0.5681	MU/RO w/air (TG-61)	1.02512
Average	0.5650	0.5637	0.5681	Output Air-kerma in air (cGy/mAs)	0.0120
P_{ion}		1.001		Output Water-Kerma in air (cGy/mAs)	0.0123
P_{pol}		0.997		Output-Exposure (mR/mAs)	**13.683**
Interpolation values for mu/ro w/air					
HVL (mm Al)		mu/ro w/air			
1	2	1	2		
4.00	5.00	1.025	1.029		

Table iii The table is an example of the format used to register raw and processed data during *output* measurement in the General Electric LightSpeed® CT Simulator.

Appendix 4: Percentage Depth Dose (PDD) curve for kilovoltage photon beams

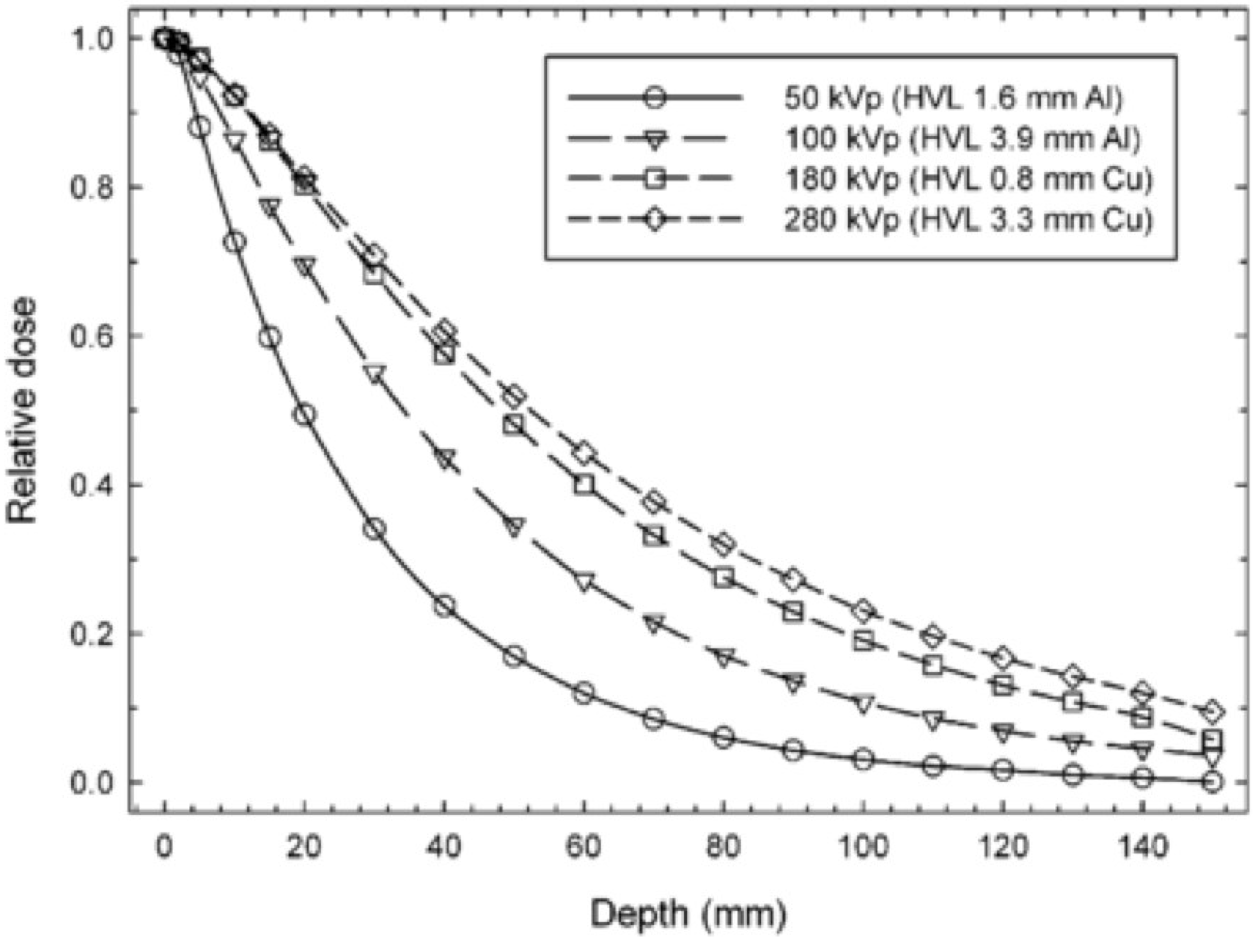

Figure i. PDD curve for kilovoltage photon beams [57]

Appendix 5: Raw and processed data from CTDI Measurements

Machine		**CT GE**			Date			2013-09-28		
					Protocol					
		Head 1Slice			Axial Head			Helical Body		
Protocol parameters	Peak Energy (kVp)	120			120			120		
	Tube Current (mA)	300			300			440		
	Exposure time (ms)	1000			2000			1000		
	Beam collimation (mm)	5			5			5		
	Pitch	-			-			0.986		
	Displayed CTDI (mGy)	64.21			84.39			35.48		
Fitting Parameters	Alpha	6.8206			6.8206			6.8500		
	Beta	-1.7136			-1.7136			-1.7193		
$[\mu_{en}/\rho]_{air\ to\ water}$		1.035			1.035			1.035		
					Measurement					
		1	**2**	**3**	**1**	**2**	**3**	**1**	**2**	**3**
ΔR_{net}	Up	0.046	0.039	0.042	0.377	0.367	0.368	0.286	0.284	0.286
	Right	0.039	0.040	0.038	0.368	0.363	0.363	0.278	0.276	0.277
	Down	0.042	0.032	0.036	0.349	0.345	0.340	0.252	0.257	0.253
	Left	0.043	0.041	0.042	0.371	0.371	0.363	0.282	0.280	0.282
	Center	0.043	0.042	0.044	0.372	0.367	0.369	0.197	0.196	0.200
	Weighted	0.043	0.040	0.041	0.368	0.363	0.362	0.249	0.248	0.250
$K_{air}\ (cGy)$	Up	0.341	0.289	0.308	7.284	6.769	6.785	3.847	3.793	3.865
	Right	0.284	0.289	0.279	6.807	6.551	6.551	3.654	3.605	3.622
	Down	0.310	0.235	0.263	5.935	5.768	5.560	3.046	3.160	3.073
	Left	0.314	0.301	0.309	6.947	6.938	6.533	3.738	3.689	3.738
	Center	0.316	0.312	0.328	7.003	6.729	6.847	2.044	2.026	2.092
	Weighted	0.314	0.289	0.302	6.830	6.581	6.520	3.062	3.050	3.080
$D\ (cGy)$	Up	0.353	0.299	0.319	7.539	7.006	7.023	3.982	3.925	4.000
	Right	0.294	0.299	0.288	7.045	6.780	6.780	3.781	3.731	3.748
	Down	0.321	0.243	0.273	6.142	5.970	5.754	3.153	3.270	3.181
	Left	0.325	0.312	0.320	7.190	7.181	6.761	3.869	3.818	3.869
	Center	0.327	0.323	0.339	7.248	6.964	7.087	2.116	2.097	2.165
	Weighted	0.325	0.300	0.313	7.069	6.811	6.749	3.169	3.156	3.188
$CTDI_w$(mGy)		62.49			68.76			31.71		
CTDI abs. uncertainty (mGy)		2.05			1.39			0.13		
CTDI rel. uncertainty (%)		3.28			2.02			0.41		
$\frac{CTDI_m - CTDI_d}{CTDI_d} \times 100\ \%$		-2.68			-18.52			-10.62		

Table iv The table is an example of the format used to register raw and processed data during *CTDI* measurement in the General Electric LightSpeed® CT Simulator.

Appendix 7: Processed data form Integration Length effect analysis

		Integration length (mm)													
	Measurement point	**10**	**20**	**30**	**40**	**50**	**60**	**70**	**80**	**90**	**CTDI_100**	**110**	**120**	**130**	**140**
CTDI (*mGy*)	Up	36.85	47.08	52.66	57.20	60.53	63.04	65.41	68.08	69.99	71.39	72.59	73.67	74.30	75.08
	Right	31.81	39.52	45.04	49.08	52.00	54.21	56.14	57.72	58.79	59.71	60.55	60.78	61.29	61.85
	Down	27.18	36.28	42.08	46.34	50.58	54.00	56.78	59.54	62.30	64.62	66.12	67.39	68.97	70.34
	Left	29.30	42.76	48.29	52.58	55.92	58.68	60.93	63.02	64.68	65.77	66.67	67.84	68.62	69.14
	Center	18.46	29.53	36.98	43.04	48.21	52.83	56.52	60.21	63.57	66.02	68.06	69.98	71.68	73.05
	Weighted	27.01	37.45	43.67	48.55	52.58	55.93	58.72	61.46	63.82	65.59	67.01	68.27	69.42	70.42

Table v. The table is an example of the format used to register raw and processed data during *CTDI* measurement in the General Electric LightSpeed® CT Simulator for integration length tests.